Advanced Fluorescence Microscopy to Study Plasma Membrane Protein Dynamics

THÈSE N^O 4869 (2010)

PRÉSENTÉE LE 5 NOVEMBRE 2010

À LA FACULTÉ SCIENCES DE BASE

LABORATOIRE DE CHIMIE PHYSIQUE DES POLYMÈRES ET MEMBRANES

PROGRAMME DOCTORAL EN CHIMIE ET GÉNIE CHIMIQUE

ÉCOLE POLYTECHNIQUE FÉDÉRALE DE LAUSANNE

POUR L'OBTENTION DU GRADE DE DOCTEUR ÈS SCIENCES

PAR

Joachim PIGUET

acceptée sur proposition du jury:

Prof. L. Helm, président du jury
Prof. H. Vogel, Dr R. Hovius, directeurs de thèse
Prof. K. Johnsson, rapporteur
Prof. A. Triller, rapporteur
Prof. J. Widengren, rapporteur

ÉCOLE POLYTECHNIQUE
FÉDÉRALE DE LAUSANNE

Suisse
2010

ii

Abstract

Membrane protein dynamics is of great importance for living organisms. The precise localization of proteins composing a synapse on the membrane facing a nerve terminus is essential for proper functioning of the nervous system. In muscle fibers, the nicotinic acetylcholine is densely packed under the motor nerve termini. A receptor associated protein, rapsyn, acts as a linker between the receptor and the other components of the synaptic suramolecular assembly.

Advances in fluorescence microscopy have allowed to measure the behavior of a single receptor in the cell membrane. In this work single-molecule microscopy was used to track the motion of ionotropic acetylcholine (nAChR) and serotonin ($5HT_3R$) receptors in the plasma membrane of cells. We present methods for measuring single-molecule diffusion and their analysis.

Single molecule tracking has shown a high dependence of acetylcholine receptors diffusion on its associated protein rapsyn. Comparing muscle cells that either express rapsyn or are devoid of it, we found that rapsyn plays an important role on receptor immobilization. A three-fold increase of receptor mobility was observed in muscle cells devoid of rapsyn. However, in these cells, a certain fraction of immobilized receptors was also found immobile. Furthermore, nAChR were strongly confined in membrane domains of few tens of nanometers. This showed that membrane composition and membrane associated proteins influence on receptor localization. During muscle cell differentiation, the fraction of immobile nAChR diminished along with the decreasing nAChR and stable rapsyn expression levels. The importance of rapsyn in nAChR immobilization has been further confirmed by measurements in HEK 293 cells, where co-expression of rapsyn increased immobilization of the receptor.

nAChR is a ligand-gated ion-channel of the Cys-loop family. In mammals, members of this receptor family share general structural and functional features. They are homo- or hetero-pentamers and form a membrane-spanning ion channel. Subunits have three major regions, an extracellular ligand binding domain, a transmembrane channel and a large intracellular loop. $5HT_3R$ was used as a model to study the effect of this loop on receptor mobility. Single-molecule tracking experiments on receptors with progressively

larger deletions in the intracellular loop did not show a dependence of the size of the loop on the diffusion coefficient of mobile receptors. However, two regions were identified to play a role in receptor mobility by changing the fractions of immobile and directed receptors. Interestingly, a prokaryotic homologue of cys-loop receptors, ELIC, devoid of a large cytoplasmic loop was found to be immobile or to show directed diffusion similar as the wild-type $5HT_3R$.

The scaffolding protein rapsyn stabilizes nAChR clusters in a concentration dependent manner. We have measured the density and self-interactions of rapsyn using FRET microscopy. Point-mutations of rapsyn, known to provoke myopathies, destabilized rapsyn self-interactions. Rapsyn-N88K, and R91L were found at high concentration in the cytoplasm suggesting that this modification disturbs membrane association of rapsyn. A25V was found to accumulate in the endoplasmic reticulum.

Fluorescent tools to measure intracellular concentration of calcium ions are of great value to study the function of neurons. Rapsyn is highly abundant at the neuromuscular junction and thus is a genuine synaptic marker. A fusion protein of rapsyn with a genetically encoded ratiometric calcium sensor has been made to probe synapse activity.

This thesis has shown that the combined use of biologically relevant system and modern fluorescence microscopy techniques deliver important information on pLGIC behaviour in the cell membrane.

Keywords: Fluorescence, microscopy, plasma membrane, membrane proteins, membrane proteins diffusion, single-molecule imaging, single-molecule tracking, pentameric ligand-gated ion channels, nicotinic acetylcholine receptor, serotonin receptor, synapse, neuromuscular junction, post-synaptic scaffold, rapsyn, myopathies, fluorescent proteins, Förster resonance energy transfer, FRET imaging, protein-protein interactions, protein trafficking, photo-activatable proteins.

Résumé

La dynamique des protéines dans les membranes lipidiques est d'une grande importance pour le bon fonctionnement des organismes vivants. La localisation précise des protéines synaptiques face à la terminaison nerveuse est essentielle au système nerveux. Dans les fibres musculaires, le récepteur nicotinique de l'acétylcholine est arrangé densément sous les terminaisons du nerf moteur.

Des méthodes avancées de microscopie de fluorescence ont permis la mesure du comportement individuel de récepteurs dans la membrane plasmique de cellules vivantes. Lors de ce travail, la microscopie de molécules individuelles a été utilisée pour suivre le mouvement des récepteurs ionotropes de l'acétylcholine (nAChR) et de la sérotonine (5HT$_3$R) dans la membrane plasmique.

Le suivi de molécules individuelles montre une forte dépendance de la rapsyn, une protéine associée au récepteur dans la jonction neuromusculaire, sur le récepteur de l'acétylcholine. La comparaison de la mobilité du récepteur dans des cellules musculaires qui expriment ou non la rapsyn montre le rôle important de la rapsyn dans l'immobilisation du récepteur. Trois fois plus de récepteurs mobiles ont été mesurés dans les cellules qui n'expriment pas la rapsyn. Néanmoins, dans ce type de cellule, une fraction importante du récepteur est immobile. Une fraction substantielle de récepteur de l'acétylcholine diffuse dans des domaines de quelques nanomètres. Ce confinement suggère un rôle important des propriétés de la membrane plasmique dans la localisation des récepteurs. Lors de la différentiation des cellules en fibres musculaires, la fraction de récepteurs immobiles diminue en fonction de l'augmentation de l'expression du récepteur de l'acétylcholine par rapport à celle de la rapsyn. L'importance de la rapsyn dans l'immobilisation des récepteurs a été confirmée par des mesures de mobilité dans des cellules HEK 293 où la co-expression de la rapsyn a augmenté l'immobilisation du nAChR.

Le nAChR est un canal ionique de la famille des Cys-loop, déclenché par un ligand. Chez les mammifères, les membres de cette famille de protéines partagent des caractéristiques structurales et fonctionnelles. Ils se présentent sous la forme d'un homo ou hétéro pentamère et forment un canal à travers la membrane. Les sous-unités se composent de

trois parties principales, un domaine extracellulaire de liaison pour le ligand, un canal à travers la membrane et une longue boucle intracellulaire. Le $5HT_3R$ a été utilisé comme modèle pour l'étude de l'effet de cette boucle sur la mobilité des récepteurs. Des expériences de suivi de molécules individuelles sur différents mutants du récepteur avec des délétions de plus en plus longues dans la boucle intracellulaire n'ont pas montré de dépendance de la taille de cette boucle sur le coefficient de diffusion des récepteurs mobiles. Néanmoins, deux régions importantes pour la mobilité du récepteur ont été identifiées, l'une modifie la fraction de récepteur diffusant de manière dirigée et l'autre la quantité de récepteurs immobiles.

La rapsyn, une protéine structurale de la jonction neuromusculaire, stabilise les agrégats de nAChR par rapport à sa concentration. Nous avons mesuré la densité et le niveau d'auto-interaction de la rapsyn par microscopie de FRET. Des mutations ponctuelles, connues pour provoquer des myopathies chez l'homme, déstabilisent l'auto interaction de la rapsyn. Les mutations N88K et R91L augmentent la quantité de rapsyn dans le cytoplasme, ce qui suggère une diminution de l'interaction de la rapsyn avec la membrane. La mutation A25V provoque, elle, une accumulation de la protéine dans le réticulum endoplasmique.

Les senseurs qui permettent de mesurer la concentration intracellulaire des ions calcium sont très utiles pour l'étude des fonctions des neurones. La rapsyne est naturellement abondante dans la jonction neuromusculaire. Cette protéine peut donc être utilisée comme marqueur de cette synapse. Une protéine de fusion entre la rapsyn et un senseur de calcium génétiquement encodé a été construite par génie génétique pour mesurer l'activité de la jonction neuromusculaire.

Avec cette thèse, nous avons montré que la combinaison de systèmes biologiques pertinents et de techniques modernes de microscopie de fluorescence permet d'obtenir des informations importantes sur le comportement des pLGIC dans la membrane cellulaire.

Mots-clés : Fluorescence, microscopie, membrane plasmique, protéines membranaires, diffusion de protéines membranaires, imagerie de molécules individuelles, suivi de molécules individuelles, canaux pentamèriques déclanchés par un ligand, récepteur nicotinique de l'acétylcholine, récepteur de la sérotonine, synapse, jonction neuromusculaire, structures post-synaptiques, rapsyn, myopathies, protéines fluorescentes, transfert d'énergie par résonance de Förster, imagerie de FRET, interactions protéine-protéine, acheminement de protéines, protéines photo activables.

Table of Contents

Introduction

1.1 General introduction

The existence of life results from the compartmentalization of essential processes into confined volumes. The first unicellular organism developed and grew thanks to the protection given by a lipid bilayer. Membrane receptors have added a dramatically important feature to primitive organisms, the ability to sense and communicate with its surrounding, while retaining the protection given by plasma membrane.

In more complex organisms, the role of membrane receptors has evolved from single sensors of the environment to part of fast and reliable signaling platforms. These particular regions of the cell plasma membrane are essential for the survival of evolved organisms. Synapses belong to these highly ordered structures. They are responsible of the propagation of information in the brain and throughout the entire organism.

Synapses are composed of hundreds of proteins, which all have defined roles in synaptic formation and function. Proteins found in synapses have shorter lifetimes than synapses themselves. This means that stability of this complex is not a consequence of the stability of its components but depends on the ability of the assembly to regenerate.

Ionotropic neurotransmitter receptors are major components of synapses. They are directly responsible for the conversion of the chemical signal secreted by the presynaptic nerve to an electrical signal. They are found at very high density in synapses. Understanding how the receptors are maintained at high concentrations in these very localized regions and how receptors associate to proteins in these specialized structures is of first importance, and will be the major subjects of this thesis.

1.2   Plasma membranes

The cellular plasma membrane is not just a permeability barrier between the cytoplasm and the surrounding media, but it also mediates the transmission of matter and information between the intra- and extracellular media. The plasma membrane is a 5 nm-thin lipid bilayer containing proteins. Lipids are amphiphilic; they are made up of a polar head group and a hydrophobic tail. In water, these amphiphilic molecules form bilayers by an entropy driven process. Membrane-associated proteins usually have regions with a high hydrophobic side-chain content, which form transmembrane domains.

The model proposed by Danielli and Davson in 1935 postulated a lipids bilayer containing only lipids covered on both sides by globular proteins [1]. This model remained valid until 1972, when Singer and Nicolson proposed the fluid mosaic model. This model was the first model where proteins were inserted in the membrane. Furthermore, this accurate model described the plasma membrane as a 2D fluid continuum with freely diffusing transmembrane proteins randomly distributed in the membrane [2]. This model did not exclude the existence of multiple phases or discontinuity in the plasma membrane. It was being refined but is still correct as general description.

The lipid membrane is a very efficient electrical insulator. In absence of proteins, lipid bilayers are virtually impermeable to ions and generally to water-soluble molecules. This property is independent of the size or the charge of ions. The presence of charged molecules in the hydrophobic region of the bilayer is energetically unfavorable and the large hydration sphere encircling ions increases this effect. Organelles are also isolated from the cytoplasm by membranes. The impermeability of membranes is required for fundamental cellular process such as maintenance of ion gradients for co-transport of solutes or action potential propagation.

The lipid organization in plasma membrane is complex. The cell plasma membranes are composed of more than 1000 different lipids [3], which have multiple functions. Lipids can stabilize or destabilize protein complexes, serve as messenger, or modulate bilayer fluidity. The lipid composition is different for organelles and cellular membrane. Furthermore, the lipid composition of the inner and outer leaflets is different, yielding an asymmetric distribution (e.g. exposure of phosphatidylserine on the outer leaflet of apoptotic cells [4]).

The majority of lipids is synthesized in the endoplasmic reticulum (ER). They are then actively translocated specifically to their final destination after sorting in the trans-Golgi network (TGN) [3].

Like lipids, most of the membrane-spanning proteins are synthesized in the ER. They are then exported through the trans-Golgi network. Some proteins interacting at the plasma membrane are exported together from the ER to the plasma membrane, like rapsyn and nAChR [5].

Cell shape is maintained by a dense protein structure, the cytoskeleton. Some components of the cytoskeleton are membrane associated and interact directly with the membrane [6, 7]. Their organization is essential for cell polarization, cell junctions or synapses formation. The cytoskeleton shapes the plasma membrane and enables the existence of complex structure like caveolin or clathrin-coated pits [8]. All these cytoskeleton-membranes interactions have dramatic effects on membrane protein diffusion [9].

Lipids and protein form domains in membranes, also called rafts [10, 6]. These nanometer-sized regions compartmentalize the membrane. Raft formation is driven by local immiscibility and phase separation of membrane components. Regions enriched in cholesterol and sphingolipids [11] coalesce to form transient rafts of a few nanometers [12]. The raft hypothesis postulates a role for lipid heterogenousity in membrane organization and function [13]

Membrane proteins correspond to a large fraction of the total cellular protein content. A considerable part of membrane proteins serves as signal transducer across the membrane. Indeed, they receive an extracellular signal and trigger a reaction of the cell. There are many types of receptor in mammal plasma membrane. Some, like ligand-gated ion channels, just open ion-selective channels leading to change in cell polarization. When others trigger major modification in cell function and phenotype like differentiation or apoptosis.

In central and peripheral nervous system, the fast signal transduction between neuron or between neurons and muscles fibres is mediated by ligand-gated ion channels. The receptors are localized at the post-synaptic side of the synapses. Receptors bind the neurotransmitters released by the presynaptic cell, and open a channel. The postsynaptic density (PSD) is a very specialized region of the cell membrane. All the proteins necessary for correct signal transmission, i.e. are localized at the contact region between pre- and postsynaptic cell. PSD is a highly dynamic structure [14].

1.3   Pentameric ligand-gated ion channels

Pentameric ligand-gated ion channel (pLGIC), previously known as cys-loop receptors, are involved in the fast signal transduction in synapses. They are composed of five subunits (homo- or heteropentamers) surrounding a pore.

The strong development of bioinformatics tool and the huge amount of sequenced prokaryotic genome have allowed the discovery of potential homologues of pLGIC in bacteria [15]. Glvi (GLIC) was the first prokaryotic homologue of pLGIC, that was cloned from the cyanobacterium *Gloeobacter violaceus* in 1997. It was identified as a proton gated ion channel after heterologous expression in HEK 293 cells and *Xenopus* oocytes. The first electron micrographs clearly showed a pentameric arrangement of the

subunits [16].

The first crystal structure of a pLGIC was obtained for a homologue from *Erwinia chrysanthemi*, ELIC, with a 3.3 Å resolution. This high-resolution structure corresponded well to the general features determined previously on nAChR with cryo-electron microscopy confirming the assumed similarity from structure homology [17]. As previously predicted, the protein is composed of five different subunits surrounding a water-filled pore [18].

1.3.1   Nicotinic acetylcholine receptor

The muscle nAChR belongs to the superfamily of pLGIC (see paragraph 1.3). nAChR are highly expressed in the electric organ of the ray *Torpedo*. From this natural source, nAChR was purified for the first time [22].

nAChR structure — As a member of the cys-loop subfamily, the nAChR is a pentamer. This receptor is found in the CNS and at the NMJ. Five different types of subunits have been isolated ($\alpha, \beta, \delta, \gamma$ and ϵ), which have a homologous amino-acid sequence and a similar tertiary structure. Nine different subtypes of α subunit (α1-9) and four of β (β1-4) have been isolated in vertebrates [23]. According to Corringer et al., acetylcholine receptor subunits can be classified in four different subgroups; epithelial (α9), neuronal I (α7-8), neuronal II (α2-6 and β2-4) and muscle (α1, β1, δ, γ and ϵ) type receptors. Members of the epithelial and neuronal I subgroups form homopentamers, whereas members of the neuronal II subgroup form a heteropentamer composed of α and β subunits. The muscle subgroup nAChR is also a heteropentamer but composed of four different subunits in the anticlockwise arrangement when looking from the extracellular side $\alpha, \gamma, \alpha, \delta, \beta$ in its fetal form; in the adult form γ is replaced by ϵ [24].

A first structural model structure at 9 Å of the receptor was proposed by N. Unwin in 1993 [25] showing the arrangement of the subunits around a pore. A recently refined structure (shown in fig. 1.1) at 4 Å has been published by the same author [17] giving new insights on the extracellular, transmembrane parts, and intracellular helix (MA). The two ligand-binding pockets have been localized at the interface of α-subunits and δ or γ subunits. These structures have been determined by cryo-electron microscopy on tubular 2-dimensional crystals obtained from *Torpedo* membranes.

The pore inside the membrane region was also studied by substituted-cysteine accessibility method (SCAM) by A. Karlin [26]. Within this approach, amino acids of the second transmembrane helix (TM2) are replaced sequentially by cysteine in order to determine which residues are accessible to a sulphydryl-specific reagent (e.g. methanethiosulfonate containing probes), identifying amino acids lining the pore in the resting and open states.
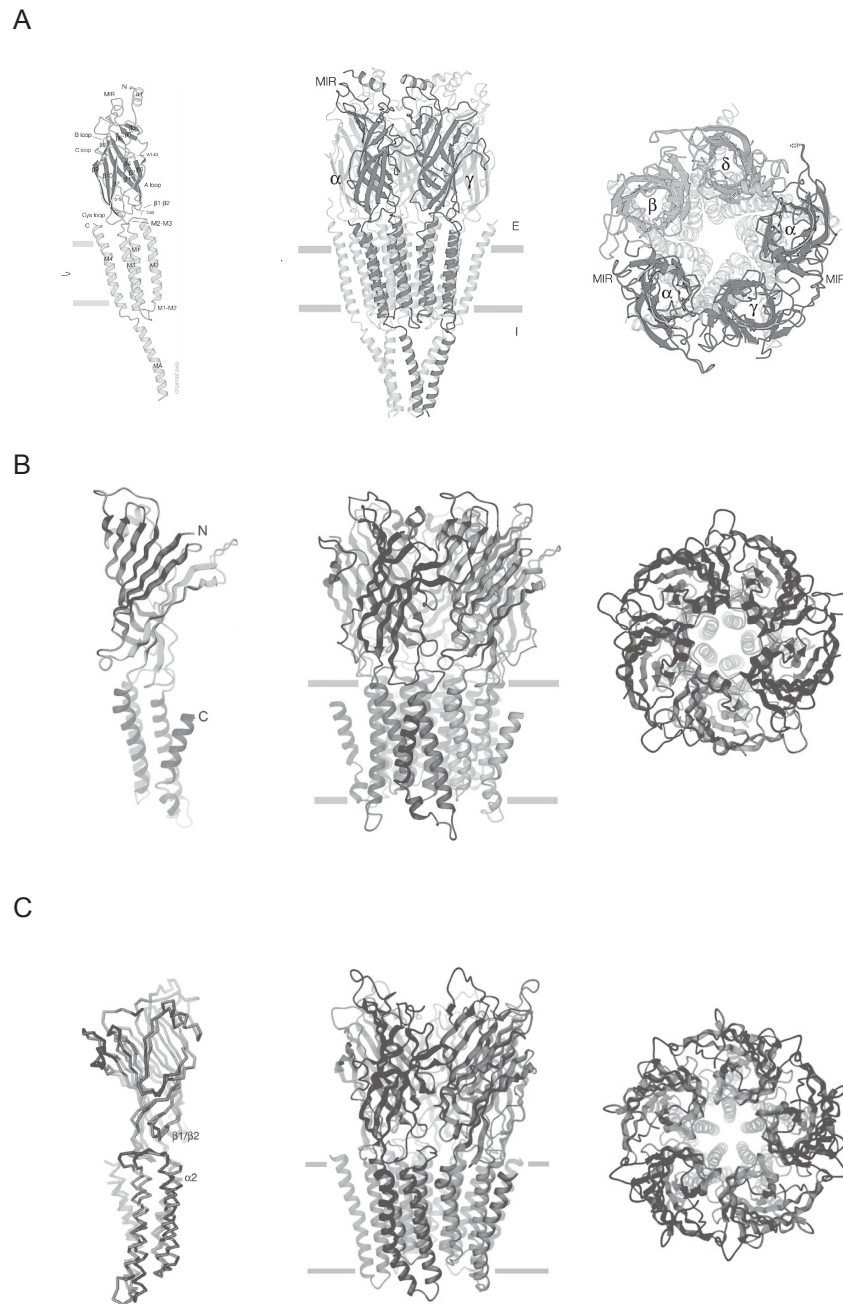
Figure 1.1: Currently known structures of pLGIC. All structures are shown at the single subunit level, from side, and from top. **A.** 4 Å resolution electron microscopy structure of nAChR from *Torpedo marmorata* (pdb 2BG9 [17]). The α subunit is shown. **B.** X-ray structure at 3.3 Å resolution of ELIC, a homopentameric LGIC from *Erwinia chrysanthemi* (pdb 2VL0) [19]. **C.** X-ray structure at 3.1 Å resolution of GLIC, a homopentameric LGIC from *Gloebacter violaceus* (pdb 3EHZ) [20, 21]. ELIC and GLIC are thought to be in a close and open conformation, respectively.

Another significant step was the discovery of a soluble analogue of the N-terminal extracellular domain of nAChR from the snail *Lymnea stagnalis*, named acetylcholine-binding protein (AChBP)[27]. This protein has been crystallized and a high-resolution X-ray diffraction structure has been determined. Further studies on another AChBP from *Aplysia californica* [28] have yielded structures of nAChBP with different ligands.

Ligand-binding and channel-gating — The natural ligand of the nAChR is acetyl-choline. Binding of two neurotransmitter molecules to the two binding-sites of the muscle receptor causes channel opening; the opening of the channel is gated by the binding of the ligand. The original kinetic model of nAChR as proposed by del Castillo and Katz in 1957 [29] was refined to account for allosteric interactions [30]. The receptor has three distinct states; basal, opened and desensitized. The most stable state in the absence of agonist is the basal, closed state. Binding of agonists displaces the equilibrium toward the open channel. When the receptor binds agonists for a prolonged time, it becomes desensitize. This third state is the most stable one in presence of agonist.

One of the best ways to catch a prey or to protect oneself against a predator is to immobilize the target, by blocking its skeletal muscle function. Therefore muscle acetylcholine receptor (as well as CNS acetylcholine receptors) is a preferential target for many natural toxins [31].

1.3.2   Serotonin type 3 receptor

The 5-hydroxyptamine type 3 receptor ($5HT_3R$) is the only ion channel among all the serotonin receptors and shares a high homology with nAChR. The receptor is also a pLGIC. Its is located presynaptically and is involved in the modulation of the neuro-transmitter release. $5HT_3R$ plays a very important role in emesis. It is therefore a pref-erential target for chemotherapy side effects. Five different subtypes have been isolated (A, B, C, D, and E). Only the $5HT_{3A}$ subtype can form a functional homo-pentamer, with a very low conductance (0.5 pS) [32]. $5HT_{3B}$ subtype can form a hetero-pentamer with the A subunit, whereas it is retained in the ER when expressed alone [33]. The other subtypes have not been found to form functional receptors, but seem to modulated receptor trafficking [32].

The $5HT_3R$ subtypes are widely expressed in human. The mRNA level of the receptor A subtype is very high in the gastro-intestinal tract and in the central nervous system (CNS). The different subtypes are more specifically expressed throughout the different organs [34].

A more complete description of the $5HT_3R$ structure is presented in chapter 7.

1.4   Neuromuscular junction

The vertebrate neuromuscular junction (NMJ) mediates the signal transmission from motor neuron to skeletal muscle. NMJ is a highly specialized structure involving assembly of numerous proteins. It is composed of three different cell types (fig. 1.2), a nerve, some Schwann cells and a muscle fibre. Its role as a chemical synapse is to transmit a signal from a presynaptic cell to a postsynaptic one. In this case, the action potential transmitted along the presynaptic motor neuron is converted to a chemical signal, i.e. acetylcholine release, and restored to an action impulse by its associated receptor on the postsynaptic membrane. The extracellular matrix and specific protein-protein interactions help to maintain the link between the nerve terminus and the muscle fibre. The whole synapse is isolated from its surrounding by several Schwann cells.

1.4.1   Action potential

In the motor system, the action potential propagates along the nerve axon by opening cation (Na^+ and K^+) permeable channels. The depolarization of the membrane at the pre-synaptic endplate causes the opening of presynaptic calcium channels. The Ca^{2+} influx in the nerve terminus induces the fusion of the acetylcholine-containing vesicles to the presynaptic membrane. Acetylcholine is rapidly released at millimolar concentration into the synaptic cleft and diffuse rapidly over the 50-100 nm wide cleft. The neurotransmitter binds to the acetylcholine receptor inducing channel opening. Due to the electro-chemical potential difference of Na^+ and K^+ between the cytosol and the cell's surroundings, a flux of cations is established between the cytosol of muscle fibre and the surrounding medium. This leads to the depolarization of the membrane, and subsequently the opening of the muscle cell voltage-gated ion channels, which enhances the depolarization. In turn, this causes the calcium channels of the sarcoplasmic reticulum to open. The increase of calcium concentration in the cytosol then leads to the contraction of the myofibrils. Acetylcholine that remains in the synaptic cleft is either degraded by the acetylcholinesterase present within the NMJ or diffuses away. Other chemical synapses in the central nervous system (CNS) have a similar functioning. The precise localization of all the synaptic proteins is crucial for the fast and reliable transmission of nervous action potential.

At the post-synaptic endplate of mature muscle fibres the density of the nAChR is around 10'000 receptors /μm^2, 1000 times higher the in the bulk membrane [37]. This dense packing of receptors is maintained during the entire lifetime of the synapse, which is far longer than the turnover of the receptor of 14 days [38]. The receptors at the NMJ are thus continuously removed and renewed. This process is maintained by a complex set of scaffolding proteins located in the post-synaptic density of the NJM, which
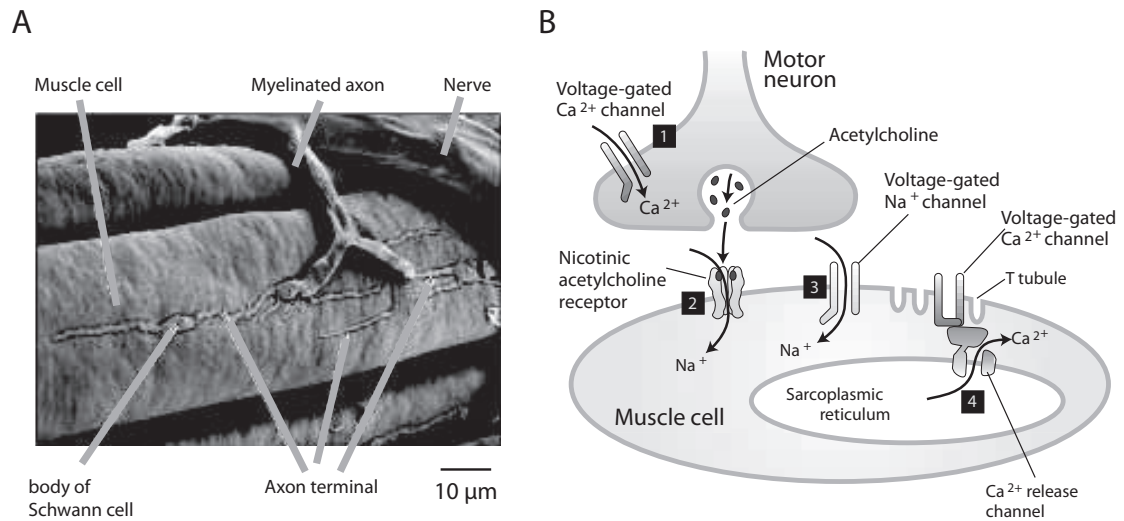
Figure 1.2: Neuromuscular junction (NMJ). A. Low-magnification scanning electron micrograph of a frog neuromuscular junction (image takee from [35]). **B.** Schematic representation of the NMJ. The action potential is pointed out by number 1 to 4. (reproduced from [36]).

interact reversibly with the nAChR, maintaining the high local receptor concentration (see paragraph 1.4.2).

1.4.2 Post-synaptic scaffold

The post-synaptic scaffold is a complex structure (fig. 1.3). Despite the fact that nAChR forms patches on non-innervated myotubes [39, 40], these spots are not precursors of the post-synaptic structure. The high density and localization of receptors at the nerve-muscle interaction locus is induced by the release of agrin, a chemical signal from the axon terminus, that activates the muscle specific kinase (MuSK) [41], mediated by the LRP4 receptor, which binds specifically neuronal agrin [42, 43].

The activation of MuSK induces its immediate tyrosine phosphorylation. This event followed by a cascade of protein activation events ending with the formation of the post-synaptic density. Like rapsyn, the 43 kDa nAChR associated protein (fig. 1.4), MuSK has the ability to bind the cytoskeleton through the spectrin network. Rapsyn and MuSK colocalize in the absence of activation by agrin [44]. The stability of this apparatus is enhanced by the activity of Src-Family Kinase (SFK). For instance, these kinases control the phosphorylation level of the nAChR and stabilize the AChR-rapsyn interaction [45].

nAChR has been shown to cluster independantly of MuSK after Tid1 mediated tyrosine phosphorylation [46]. Tid1 has also been shown to take part in the PSD sta-

bilization. Other kinases are required for proper NMJ formation like Abl1 [47], which enhances MuSK induced phosphorylation *in vitro* .

These multiple interactions, occurring during synaptogenesis, enhance formation and persistance of synapse. Recently, the WNT/β-catenin signaling pathway has been shown to modulate rapsyn mediated nAChR clustering. WNT promotes clustering of synaptic nAChR, while destabilizing extrasynaptic clusters [48, 49].

During synaptogenesis, neuregulins secreted by the nerve changes the expression mode of the nAChR [50, 51]. In the nucleus closest to the NMJ, the transcription on nAChR genes is strongly enhanced, whereas in the other nuclei the transcription of nAChR is strongly reduced. The same holds for rapsyn in mature NMJ [52].
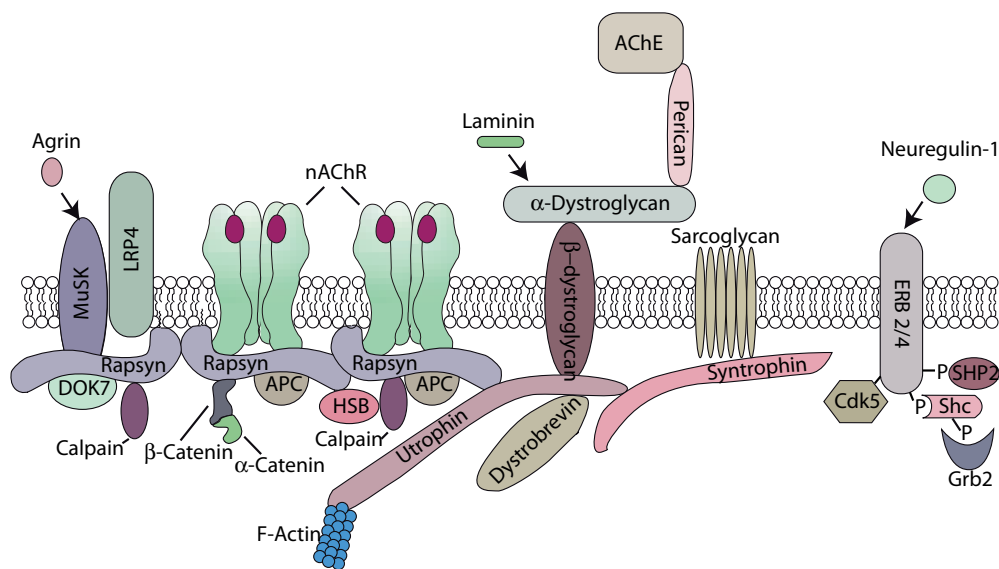
Figure 1.3: Simplified model of the post-synaptic scaffold of the neuromuscular junction. This scheme shows the three most important receptors involved in synapse formation and maintenance (nAChR, LRP4 and erbB 2/4). Some components of the post-synaptic scaffold are also depicted. This figure is not exhaustive as the actual scaffold is composed of several hundred proteins. This scheme is based on references [42, 43, 52, 53, 54, 55, 56].

Lipids micro-domains or rafts have a significant importance in neurotransmitter signaling (for a review see [57]). Concerning NMJ, some recent publications point out the importance of lipids rafts and rafts-associated structures on post-synaptic signaling. nAChR is surrounded by a well-defined annulus of lipids. These lipids have the properties of the liquid-ordered phase (for a review see nAChR see [58]). Furthermore, rapsyn is located constitutively in the lipid raft fraction as determined by detergent extraction [5]. Agrin signaling induces nAChR translocation into cholesterol and sphingolipid-rich lipid domains [59]. Other experiments show that cholesterol and lipid micro-domains stabilize

the post-synaptic side of the NMJ [60]. Cholesterol and sphingomyelin depletion changes the surface expression of nAChR in CHO and Cos7 cells [5, 61, 62]. The processes involved in NMJ post-synaptic endplate formation and maintenance are associated with the detergent resistant membrane fraction [63]. Recent fluorescence recovery ofter photobleaching (FRAP) and fluorescence correlation spectroscopy (FCS) measurements of nAChR have shown a cholesterol dependence on mobility [64].

1.5   Rapsyn and associated proteins

Rapsyn is a scaffolding protein involved in the maintenance of the post-synaptic apparatus both in muscle and in the electric organ of the *Torpedo californica* [65]. It was first named 43K protein as it appeared as a band of apparent molecular weight of 43 kDa on polyacrylamide gel during nAChR purification. Rapsyn is already expressed in muscle stem cells (myoblasts) [66] before the synapse-specific stimulated expression of the nAChR.
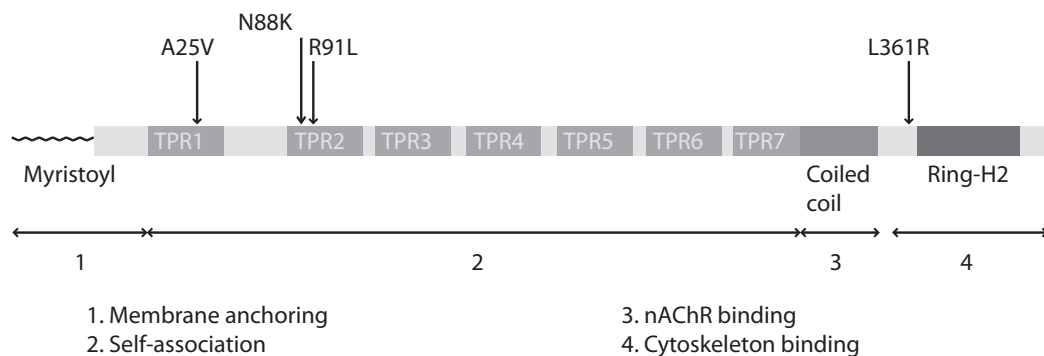
Figure 1.4: Schematic drawing of rapsyn. N-terminal myristoylation induces rapsyn anchoring to the plasma membrane. The seven tetratrichopeptide repeats (TPR) are involved in self-association. The coiled-coil region is implied in interaction with nAChR and the C-terminal region interacts with other components of the PSD. The indicated mutations provoke myasthenia in human. They have been studied in chapter 8.

Rapsyn is composed of 4 distinct parts, a N-terminal myristoylation, eight tetratricopeptides repeats (TPR), a coiled-coil domain and a zinc finger (RING-H2) motif (fig. 1.4). It has not been crystallized yet. A co-translational modification of the N-terminus adds a myristoyl tail, which targets the protein to plasma membrane. Two consensus sites for phosphorylation have been located at the end of the sequence [53]. In mature muscle fibre, rapsyn and nAChR are co-targeted to the plasma membrane [67].

The scaffolding protein acts as a linker between the major components of the NMJ (see fig. 1.3). It is able to self-associate and exhibits clusters when expressed alone [68].

The TPRs are responsible of this self-association. Rapsyn interacts directly with the intracellular loop of each nAChR subunits through a coiled-coil site located between the amino acids 298-331 on rapsyn [69, 70, 71]. Until recently it was not clear which of the receptor subunit was interacting with rapsyn. It has been shown that phosphorylation of the β subunits mediates rapsyn association with nAChR [72]. Furthermore, the same group has shown that constitutive interaction of rapsyn with nAChR subunits implied the intracellular α-helix of α, β and ϵ subunits. Thus, nAChR and rapsyn are bound both in regulated and constitutive way [73]. A clear interaction of the TPR with the cytoplasmic domain of MuSK has been pointed out [44]. Rapsyn also interacts with the dystroglycan complex [74] through its Ring-H2 domain and with the cytoskeleton via a protein of the spectrin superfamily named ACF7, that has a binding site for the TPR [75] and through α-actinin [76].

Rapsyn is bound to calpain in the functional NMJ [77]. This Ca^{2+} dependent interaction [78] plays an important role in the extrasynaptic nAChR dispersal and could, together with the WNT/β-catenin signaling (see section 1.4.2), partially explain the notable difference between the synaptic and extrasynaptic nAChR densities.

Rapsyn's main function is to link nAChR to the other proteins composing the NMJ. Except for rapsyn, nAChR has been shown to bind directly only to APC [79]. Despite a very high turnover rate (with a τ of a few hours), rapsyn is the main stabilizing protein of nAChR clusters [80]. At the NMJ, rapsyn and nAChR dynamics are independent [54].

1.6 Congenital myasthenic syndromes

Congenital myasthenic syndrome (CMS) is an ensemble of diseases provoking muscle weakness [81]. Different types of myasthenic syndromes have been identified so far, which can be divided in two major classes, auto-immune and genetic syndromes. The latter are provoked by point mutations, which disrupt the function of the synapse. Eleven proteins exhibiting mutations have been identified so far in patients suffering from myasthenia. Among all these mutations, those leading to acetylcholine receptor localization deficiency are directly related to the interaction between rapsyn and nAChR [82].

The most widespread rapsyn mutation in the population is N88K. Not all patients have the same phenotype, but the general feature at cellular level is a loss in receptor density at the NMJ postsynaptic endplate [82]. Other less frequent mutations of rapsyn have been identified such as A25V and R91L [83].

Mutations in the cytoplasmic loop of the receptor are less frequent [82]. However, recently the non-lethal mutation E381K has been identified on the δ subunit, which induces less stable receptor clusters on HEK 293 cells [84].

All these mutations have been studied on labeled and chemically-fixed cells for co-

localization of rapsyn with nAChR using confocal microscopy or by measurements of patch density [83]. Little is known on the protein-protein interactions disrupted and on receptor mobility (replacement, recycling, turn-over) in presence of these mutations in muscle cells.

1.7   Protein diffusion in the cell membrane

The lipid mosaic membrane model describes proteins as membrane-spanning objects freely diffusing in a bidimensional plane. Based on this model, Saffman and Delbrück derived a theoretical model for the diffusion coefficient for membrane proteins [85], considering the membrane as an infinite sheet with water on both sides. Experimental results have rapidly shown the limits of this model in model membranes [86] and in cells [12] (reviewed in [87, 88]). These results were later confirmed. Diffusion in membrane is a very complex phenomenon, implying several interactions with other components of the plasma membrane [9]. There is no general way to calculate an accurate theoretical diffusion coefficient.

1.8   Single molecule microscopy

Visualization of single-molecule behavior in living cell has always been a challenging question; How would be the motion, shape or localization of a single protein or lipid molecule when it is not hidden in a measurement that reveals averaged behavior of an ensemble? A living cell can be considered as a highly complex system, where proteins cannot be considered in terms of concentration in solution or average chemical state. Some proteins are expressed at very low level. Others are densely packed in quasi crystalline structure as nAChR in the electric organ of *Torpedo*.

Single-molecule techniques were designed to study individual behavior rather than the average population properties, without the need of synchronization and with the possibility to measure changes in behavior with time.

Single-molecule localization and tracking is based on the ability to distinguish photons coming from a single fluorescent molecule from the noise and the other sources of photons. This feature is obtained using well prepared samples combined with a very high-quality measurement setup.

1.8.1   First experiments

Nanovid microscopy was a breakthrough in membrane protein studies [89]. Using video enhanced microscopy, it was possible to distinguish 40 nm diameter gold beads. Therefore, for the first time, it was possible to track the motion of a single protein directly

on cells. This technique allowed one to discover confinement of proteins diffusing in the plasma membrane [90, 91]. The major drawback of these gold beads was their multivalency, which might induce protein crosslinking. The use of fluorescent monovalent labels was introduced first in measurement on cells at low temperature [92].

Single-molecule techniques were then quickly developed with measurements at room and body temperature on artificial systems [93] and living cells [94, 95]. Single-molecule methods are now widely accepted techniques to image biological processes and protein dynamics [96, 97].

1.9 Labeling

In any fluorescence microscopy experiment the molecule of interest must be labeled with a fluorescent probe. This probe can be of many types as long as it is fluorescent and specific. Labeling proteins in living cell is straightforward for standard microscopy experiments, whereas single-molecule tracking requires very specific (i.e. without unspecific interactions) and bright probes, that do not crosslink two or more proteins of interest. There are numerous methods to label protein or other biologically relevant molecules with fluorescent label probes like antibody, agonist, antagonist, substrate, affinity tags, binding proteins and fluorescent proteins. All these methods have their own drawbacks, but can be used for single-molecule experiments when carefully performed. In this thesis, two different labeling techniques have been used, specific ligands and affinity tags.

1.9.1 Ligands and affinity labels

Fluorescent ligands are very specific probes for membrane receptor proteins. A ligand can be agonist or antagonist for its associated receptor. Generally, the average lifetime of receptor-ligand complexes using natural agonist is very short, whereas antagonists or non-natural agonists have longer lasting binding.

Due to their importance in function of living organisms, membrane receptors are preferential targets for venom-associated toxins. These toxins bind very tightly and specifically their targets. The first widely used toxin, targeting nAChR, was extracted from the venom of the snake *Bungarus multicinctus*, α-bungarotoxin (α-BgTx) (fig. 1.5B). Its quasi irreversible binding to nAChR has been characterized since the seventies. Fluorescently labeled α-BgTx was quickly used as label for experiment on nAChR in mammalian skeletal muscle [101]. Many nAChR specific toxins have been subsequently discovered and are potently useful ligands for receptor labeling [102].

Among these toxins α-conotoxin-GI, extracted from the marine snail *Conus geographicus*, is of great interest for single-molecule labeling due to its specific binding to a single-site of muscle type nAChR without interacting with neuronal receptors [103, 104, 105]
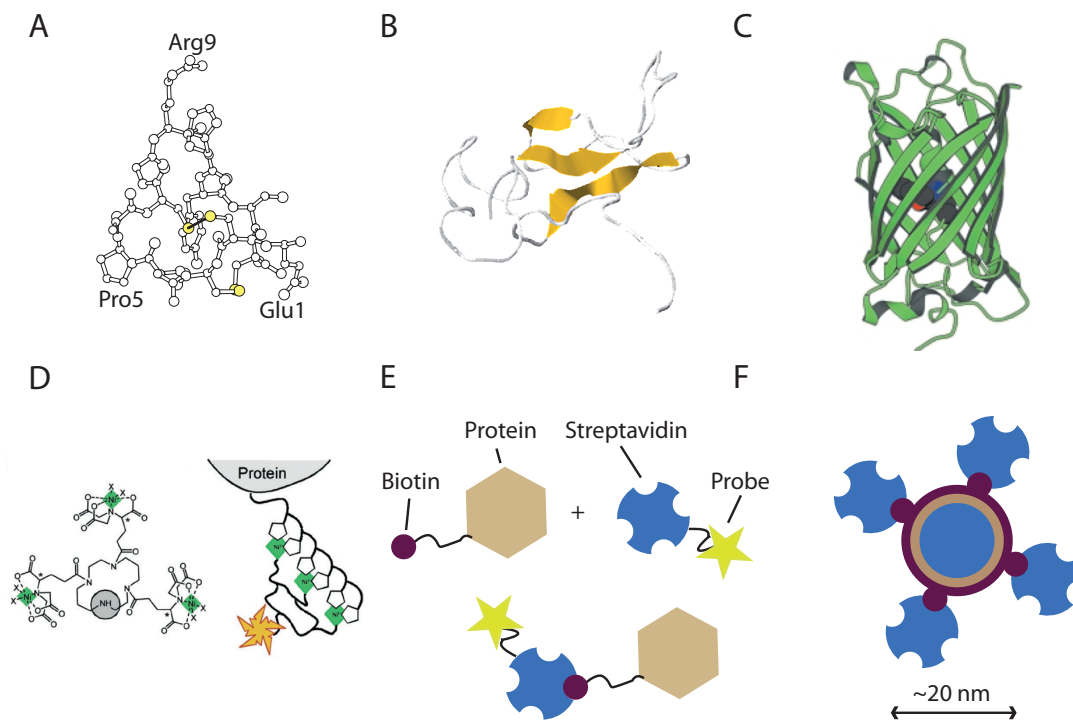
Figure 1.5: Ligands and probes used for specific protein labeling. **A.** α-conotoxin-GI (α-CnTx-GI) (PDB:1NOT) (taken from [98]), and **B.** α-bungarotoxin (α-BgTx) (PDB:1IDI) are toxins specific to nAChR. α-BgTx binds quasi-irreversibly to the receptor, whereas α-CnTx-GI binding is readily reversible. Fluorescent derivatives of these toxins were used for single-molecule experiments. **C.** Structure of the monomeric green fluorescent protein mGFP (reproduced from [99]). **D.** *tris*-NTA affinity-tag principle. The *tris*-NTA moiety (left) is binding the oligohistidine-tagged protein of interest (right) (reproduced from [100]). **E.** Biotin-streptavidin binding principle. The protein of interest is functionalized with a biotin, to which a fluorescent streptavidin can bind. **F.** Streptavidin-coated fluorescent nanoparticle or quantum dot (QD). QD are composed of a core (blue) and a shell (brown), and coated with a (bio)polymer (black) and functionalized to bind protein of interest.

(fig. 1.5A). However, its affinity is moderate ($\tau_{1/2}$ 2-500 s [105]).

A fluorescent derivative of an agonist toxin, epibatidine, has been used for single-molecule tracking of nAChR in living cell [106].

Several methods have been used for affinity labeling of proteins in cells [107]. Affinity tags are binding to specific amino-acid sequences introduced by genetic engineering into the target protein.

Among these techniques, nitrilotriacetic acid (NTA) based affinity probes are very convenient for membrane proteins labeling. They are binding to a short tag (6-10 histidines) and are available with many fluorophores [108]. The high unbinding rate of mono-NTA labels limits their use. This drawback was almost completely circumvented by the development of multivalent chelators with strongly enhanced affinity [109].

1.9.2 Fluorescent probes

The choice of the appropriated fluorescent probes is not straightforward for single-molecule studies. A large variety of dyes is available each with different properties. Measurements in cell membranes require dyes with specific spectral properties to avoid cell autofluorescence and they should not be too much hydrophobic to avoid unspecific membrane binding.

Organic dyes are widely used in single molecule studies [110]. Modern organic dyes have very interesting optical properties: High molar extinction coefficient, long wavelength of excitation, high quantum efficiency, narrow emission peaks, large Stokes shift, or high photostability. The major drawback of organic dyes is their high photobleaching yield (10^{-6}) which strongly limits the measurement time to a few seconds. Some organic dyes are more photostable and, using particular conditions, measurements with laser of more than one hour have been reported [111].

Quantum dots (QD) are nanometer-sized colloidal semiconductor crystals. Their small size induces a quantum confinement that provokes a discretization of the energy levels, giving them properties comparable to organic dyes. They can have a broad range of color depending on their composition and size [112, 113]. QD do not bleach when they are excited even with high-energy light sources. However, due to photoionization they are blinking. Single-molecule QD experiments can be performed with very long times at high signal-to-noise ratio (SNR).

Quantum dots are composed of a core and a shell of semi-conductor material (e.g. a core of CdSe and a shell of ZnS). They can be functionalized to bind molecule of interest (e.g. ref. [114, 115]). QD can also be directly coated with an affinity probe like streptavidin (fig. 1.5D and 1.5F) [116]. Commercial QD are multivalent, which might induce crosslinking of the proteins of interest. Small monovalent QD have recently been developed, reducing this drawbacks [117]

Despite a generally less define valency and a by far larger size than organic dyes, quantum dots are very convenient probes for microscopy and single-molecule imaging. They are widely used to study synaptic protein diffusion and other cellular processes (for reviews see [118, 119])

Chapter 2

Aim and scope of the thesis

The general aim of this work was to study the behavior of pentameric ligand-gated ion-channels (pLGIC) and structurally related proteins in living cells.

Chapter 3 presents the general methods used during this thesis.

Chapter 4 presents the procedures used for single-molecule localization and tracking. It focuses on the software developed for single-molecule microscopy (SMM) and in particular on modules implemented for single traces analysis. Some of the methods' advantages and drawbacks are discussed.

Chapter 5 presents the methods development and improvements for FRET measurements in living cells. The development of a versatile software is presented. This flexible software was made to analyze data of multiple types of FRET experiments.

Measurements of diffusion of single nAChR in the plasma membrane of living cells are presented in chapter 6. The aim of this chapter was to understand the role of rapsyn in nAChR immobilization and concentration in the neuromuscular junction.

Chapter 7 deals with the impact of the intracellular loop on pLGIC mobility, which is thought to be strongly dependent on this intracellular region through specific and non specific interactions with the cytoskeleton. Progressive deletions in the M3-M4 loop of the $5HT_3R$ have been made by molecular biology. The goal of this chapter was to measure the effect of the deletions on the diffusion properties of the receptor.

Rapsyn self-association and oligomerization is very important for synapse stability. Cellular localization and protein packing was studied in chapter 8. Fluorescent versions of rapsyn were imaged by microscopy to study the effect of disease-related mutations on protein aggregation and cellular localization.

General materials and methods

This chapter describes the general techniques and measurements systems used during this thesis. A more complete description of the particular methods is available in each chapter.

3.1 Molecular biology

3.1.1 Cloning and subcloning

Polymerase chain reactions were performed using Phusion DNA polymerase (Finnzymes) according to the manucfacturer's instructions. Primers were purchased from Eurofins MWG Operon and Sigma. All DNA preparations and purifications were made using Qiagen products. Restriction nucleases and ligases were from New England Biolabs. DNA plasmids were amplified in XL-10 Gold *E. coli* strains (Stratagene).

Point mutations were generally made using abutted primers with Phusion polymerase, up to 3% DMSO was added to the standard reaction mix. In some cases, mutagenesis was done with Quikchange II (Stratagene) according to the manufacturers instructions. For long primers, up to 5% DMSO was added to the reaction mix.

3.2 Cell culture and transfection

During this thesis different cell types have been used depending on their phenotype and the experiments to be performed.

3.2.1 Human embryonic kidney cells (HEK 293 T)

Adherent HEK 293 T cells (ATCC: CRL-11268) were grown in DMEM/F12 (1:1) supplemented with 10% fetal bovine serum (FBS) in a humidified 5% CO_2 atmosphere at

37°C. Cells were sub-cultived when reaching 80 % confluency. Cells were diluted 10-15 times.

HEK cells were used as background-free expression system for diffusion experiments on nAChR and $5HT_3R$, and for the characterization of fluorescent rapsyn derivatives. HEK cells express neither rapsyn nor Ric-3 [120].

3.2.2   Myoblasts and myotubes

Three mice myogenic cell lines were used for this study. C2C12 cells were a gift of U. Ruegg from Geneva University. R12 and R11 cells were a kind gift of C. Fuhrer of Zürich University.

C2C12 were grown in DMEM/F12 supplemented with 10% FBS, 100 u/ml of penicillin, and 100 μg/ml streptomycin at 34°C in a 5% CO_2 humidified atmosphere. Cells were split at maximum confluency of 80% to avoid spontaneous cell differentiation into myotubes. Controlled differentiation to myotubes was induced two days after splitting by changing the culture medium to DMEM/F12 with 10% horse serum (Gibco). Medium was changed every second day during differentiation.

Myoblasts (C2C12, R11 and R12) were transfected using Fugene 6 (Roche) according to the manufacturer with 3 μl reagent and 1 μg plasmid DNA per ml of adherent cell culture.

3.2.3   T-REx/Flp-In 293 cells

T-REx/Flp-In 293 cells (Invitrogen) were grown in DMEM/F12 supplemented with 10% FBS at 37°C in a 5% CO_2 humidified atmosphere. Cell were maintained under selection with 100 μg/ml zeocin (Invitrogen) and 10 μg/ml blasticidin. After generation of expression cell lines using pcDNA5-FRT-TO vector (Invitrogen), cells were grown under the same conditions excepted the replacement of zeocin by 100 μg/ml hygromycin.

3.2.4   Cell transfection

Cells were transfected using Effectene transfection reagent (Qiagen), Fugene 6 (Roche) or Lipofectamine 2000 (Invitrogen). All transfections were made according to manufacturer with circular plasmid DNA.

3.3   Microscopy

The majority of the experiments described in this thesis involved microscopy. Confocal microscopy was used for general purpose imaging of living cells. Single-molecule experiments were performed on a laser illuminated wide-field microscope. During this thesis,

the latter microscope was upgraded with new lasers and a multi-detector system for advanced fluorescence microscopy.

3.3.1   Confocal microscopy

Confocal imaging is a scanning microscopy method [121]. A focused laser beam is scanned along the sample to excite fluorescent probes. Photons emitted at each position are detected using the same objective. The resulting fluorescence is filtered and focused through a pinhole to remove light coming from out-of-focal plane regions and recollimated. Light is measured using a detector, generally a photomultiplier tube (PMT) or a more sensitive avalanche photodiode (APD) (fig 3.1A).

3.3.2   Wide-field microscopy

In wide-field microscopy, a laser beam is focalized on the back aperture of the objective. Light coming out from the objective is defocussed and illuminates a wide region of the sample. The image of this region is detected through the objective and directed to a CCD (or EMCCD) detector (fig 3.1B).

3.4   FRET

Cells were transfected according to the standard manufacturers protocols. For each experiment, donor (D) and acceptor (A) alone were transfected to determine the correction factors for bleedthrough (see chapter 5). Plasmid DNA D/A ratio was varied according to the mass of DNA.

3.5   Single-molecule microscopy

An existing single-molecule was upgraded to a multiple laser and detector setup. This setup is shown in figure 3.2. This microscopy system has been designed to measure simultaneously fluorescent single-molecules and FRET signals on living cells. It has also been set to perform FPALM (fluorescent photocativation localization microscopy). This setup is composed of three distinct parts, an excitation system, a microscope, and a detection system. All filters and dichroic mirrors were purchased from Chroma Corp.

3.5.1   Illumination system

The excitation system is composed of four lasers. (i) a 30 mW 405 nm diode laser (WSTech), (ii) a 25 mW 488 nm solid state laser, (iii) a 30 mW 514 nm diode laser
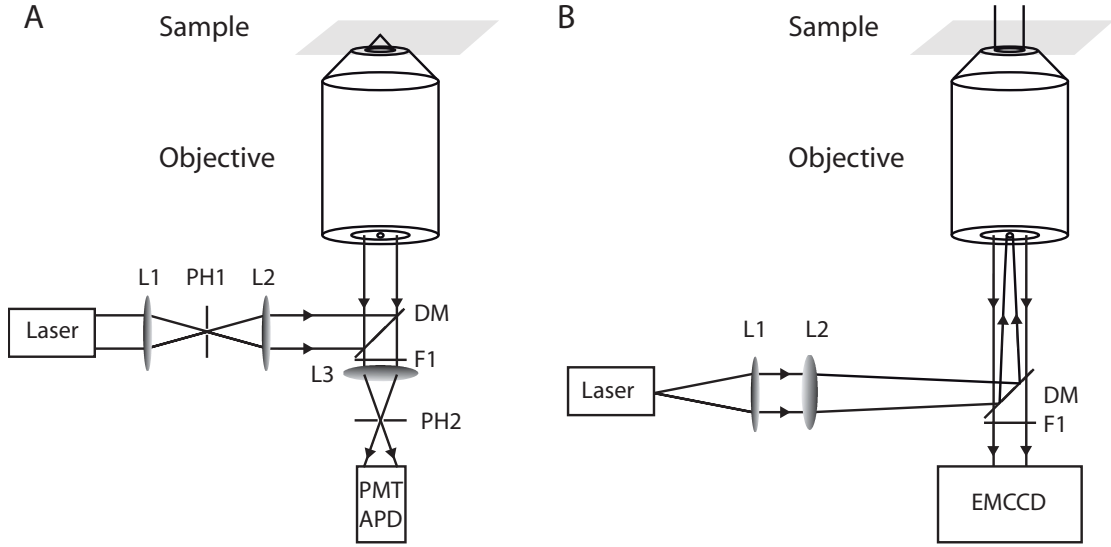
Figure 3.1: Fluorescent microscopes used in this thesis. A. Confocal microscopy principle. A parallel beam from a laser is used to fill the back aperture of the objective using a beam expander (L1 and L2). The pinhole PH1 is used to enhance the quality of the beam. The beam, focalized by the objective is scanned along the sample. Light is filtered by a band pass filter (F1) to remove unwanted fluorescence and detected by a PMT or an APD detector. Pinholes are placed in the excitation and detection pathway in a place where light is focused to remove out of plane emission. **B.** Wide-field microscopy principle. Light from a laser is collimated (L1) and then focalized (L2) on the back aperture of the objective via a dichroic mirror (DM). The beam is collimated by the objective and illuminates a wide region (wide-field) of the sample. Captured light is filtered (F1 and DM) and imaged by a camera, generally a CCD detector.

(WSTech), and (iv) a 30 mW 632.8 nm He-Ne laser (Coherent). The 405 laser is collimated with an external lens. The beam diameter of the four lasers is 1 mm. Lasers are co-linearized using four dichroic mirrors, DM1, DM2, DM3, DM4 (see table 3.1 and two broadband dielectric mirrors (Thorlabs).

The combined laser beams are filtered using an acousto-optic tunable filter (AOTF, AA Opto-Electronic). Two shutters can be placed in the position S1, S2, S3 and S4 according to the needs of the experiments. This excitation system is controlled by a home written Labview (National Instrument) program.

The laser beam diameter is increased by a beam expander (L1 and L2). The beam is then focalized on the back aperture of the objective by a wide-filed lens (L3). For some experiments requiring a good homogeneity of illumination, a diaphragm is added in the beam path to cut the low intensity periphery of the laser beam profile.
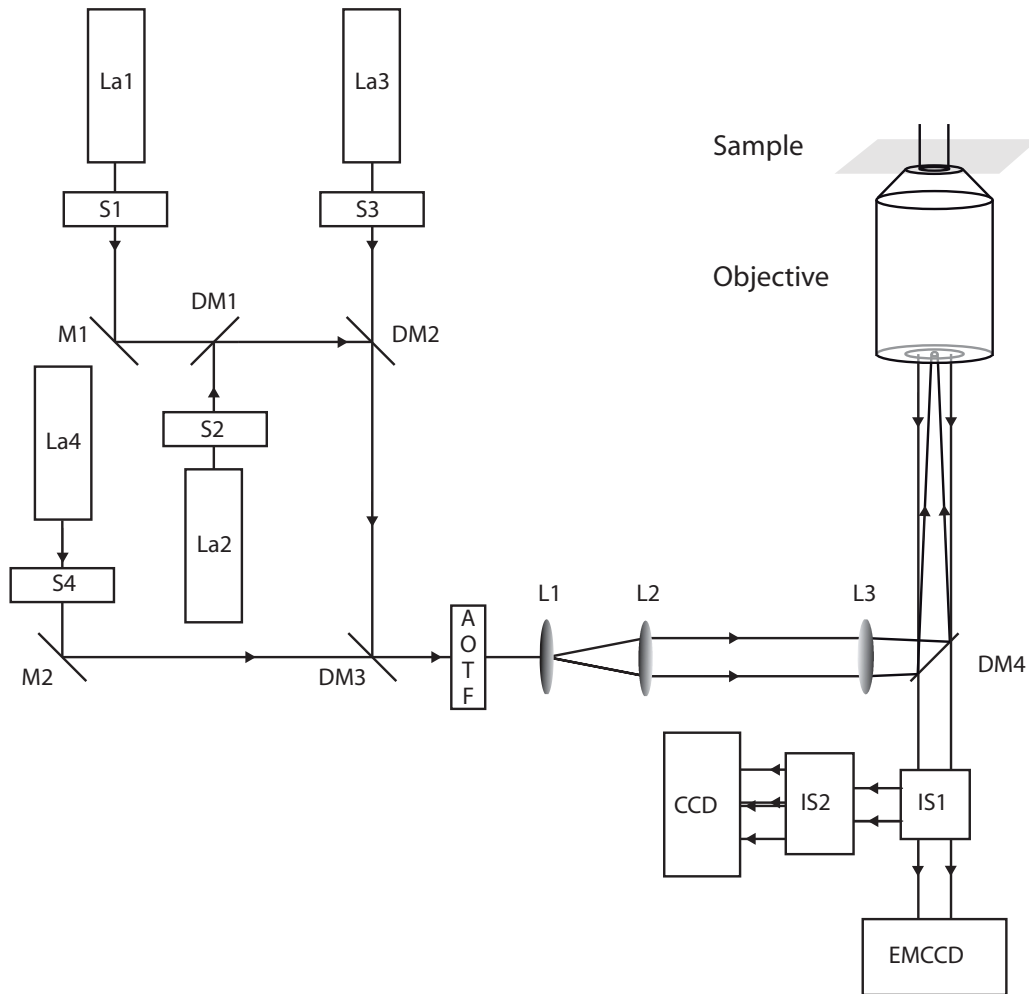
Figure 3.2: Single-molecule microscopy setup. The setup is composed of three main parts, a laser excitation system, a microscope and a CCD based detection system. A complete description of the components is made in section 3.5. La stands for laser. Laser wavelength are La1=488 nm, La2=405 nm, La3=532 nm and La4=632.8 nm. DM are dichroic mirrors with appropriate wavelength. M are broadband dielectric mirrors. S are mechanical shutters. The AOTF is an acousto-optic tunable filter. L stands for lens. IS are image color splitters. The two cameras are a CCD and an EMCCD.

Table 3.1: *Dichroic mirrors used in the illumination path of the setup described on fig 3.2*

Element	Filter name
DM1	Z405RDC
DM2	500DCXR
DM3	Z532RDC
DM4	Microscope cube turret

3.5.2 Microscope

The laser beam is directed to the sample with a dichroic mirror and an Apochromat 63x, NA=1.2, water immersion objective (Zeiss) mounted on a Zeiss Axiovert 200 microscope. Fluorescence emitted by the sample is collected through the same pathway and directed to the detection system. Filters and dichroics of the filter wheel are shown in table 3.2

3.5.3 Detection system

Image coming from the microscope are separated according to their wavelength by two image splitters. The image is first separated with a Zeiss image splitter containing a 565dcrx dichroic mirror and a 730/100HQ. Long wavelength are directed an iXon 887BV EMCCD (Andor). Short wavelengths are directed through an image splitter (Optosplit) to a Luca CCD (Andor). Both cameras are controlled by a computer, either with the manufacturer's control software or by a Labview routine.

Table 3.2: *Filter cubes used in the microscope cube turret shown in fig 3.2.*

Cube	Dichroic	Emission Filter
1	Z405RDC	None
2	Q495LP	HQ525/50
3	Z514RDC	HQ585/40M
4	Q645LP	HQ710/120

All filters used in the different beam paths can be exchanged to adapt the setup to other fluorescent probes.

3.5.4 Synchronisation

The system is controlled by a Labview (National Instruments Inc.) procedure. Cameras, shutters and AOTF are synchronized through logic pulses. The microfluidics solution changer can also be controlled by Labview. Measurements can be automated with sequential lasers pulses combined with change in the medium composition.

3.6 Cell labeling

Cells were labeled for fluorescent microscopy using three techniques. Besides genetically encoded markers, we used two ways of labeling

3.6.1 Standard batch labeling

Cells, grown on 25 mm coverslips, were labeled at 37°C in their original culture medium. They are then washed with PBS (Sigma) and mounted on a coverslip holder for subsequent measurements on a microscope. Incubation time and concentration are specified in the corresponding chapters.

3.6.2 Dynamic labeling using microfluidics

Cells were grown on 25 mm coverslips. Coverslips were mounted in coverslip holders on the measurement setup. During measurements, cells were continuously perfused with a VC-77SP solution changer (Warner).

3.7 Fluorescent ligands

α-Conotoxin-GI-Cy5 and α-conotoxin-GI-Atto647N were synthesized using N-hydroxy-succinimide (NHS) esters of Cy5 (GE Healthcare) and Atto647N (Atto-tec) and purified by chromatography. α-CnTx-GI was from American Peptide Company.

Nitrilotriacetic acid (NTA) fluorescent derivatives were synthesized according to Guignet et al. [108].

tris-NTA-Atto647N, *tris*-NTA-8pro-Atto647N and *tris*-NTA-Biotin were kind gifts of R. Tampé.

Fluorescent nanoparticles coated with streptavidin were a kind gift from M. Bäumle (Fluka). Three different batches were used with emission peaks at 570, 610 and 614 nm.

Chapter 4

Single-molecule tracking

4.1 Introduction

Biophysical measurements at single protein level in living cells have always been challenging. Many single-molecule techniques have been developed to obtain reliable information on distance, force, movement or molecular interactions in living cells (for a review see [122]). From all the techniques used to measure single molecule properties in living cells, we choose single molecule tracking to measure the position and motion of proteins.

During many years treatment of the complex data sets have been limited by the lack of computational capacity. Since the beginning of the nineties, the huge increase of personal computer power has permitted the development of easy to use powerful analysis software. Presently, software are generally based on open source freely available programs like ImageJ or written in proprietary codes (MatLab, Mathematica).

During this thesis, several experiments required complex data analysis steps. We developed two different softwares based on Igor Pro (Wavemetrics). The common aim of these softwares was to reduce the data analysis duration. Furthermore, they were designed to standardize the analysis of large data sets while keeping the versatility and flexibility of home made softwares.

A single molecule software was developed to analyze efficiently single-molecule movies acquired with a CCD detector. This analysis software has been used extensively to extract relevant biological results from single-molecule images series in chapters 6 and 7. Several analysis module have been implemented to simplify localization and tracking of molecules and subsequently to analyze the corresponding trajectories.

In this chapter, we will focus on the data analysis of single-molecule and on the limitation of single-molecule tracking methods.

4.2 Single-molecule microscopy

One of the largest challenges in cell biology is to measure events at a relevant scale. Many biological processes take place on the nanometer and millisecond scale. This spatial and temporal range is not easily accessible in living system (cells, organism). Optical single-molecule microscopy, generally performed on fluorescent molecules, allows one to measure these events. Furthermore, all single proteins behave differently. Measurements of average parameters of the population are not always relevant for membrane proteins, which have very dynamic properties, and individual molecules can behave very differently.

The major difficulty of single-molecule imaging is to find experimental conditions where biologically important molecules (proteins, ligands, ions) can be studied individually under relevant conditions. Single-molecule must be studied at very low concentrations to be enough spatially separated, i.e. generally a few molecules per cell. Several optical technique have been developed to study single-molecules (for reviews see [96, 119, 123, 124, 125])

4.2.1 Single-molecule properties

Detection of single-molecules with a standard optical microscopy system is a complex issue. Indeed, a single fluorophore has only one or two emitting dipole and can only emit a limited number of photons.

Single molecules have defined intrinsic properties, which are often useful in single molecule measurements. (i) The rate of emission of molecules of the same fluorophore under identical conditions is comparable. Therefore, the detected counts rate from a single-molecule is almost constant. (ii) When a fluorophore is irradiated with light for a long time it undergoes photo-destruction. A single-molecule always exhibits single step disappearance of the fluorescence signal, i.e. single-step photobleaching. (iii) The existence of dark electronic states, like triplet for organic dyes or photo-ionization of quantum dots, provokes intermittent emission of the molecule. This blinking effect is typical of single-molecule emission and is observed with organic fluorophore and quantum dots. (iv) In measurements performed with a very high temporal resolution a bunching effect is observed for single-molecules. When a single molecule is in a excited state, it can not absorb a new photon before relaxation. Therefore, the emission of a single-fluorophore is not continuous, there is a minimum delay between emission of subsequent photons of a few nanoseconds. (v) The fluorescence of a single-molecule is emitted from a defined dipole. The emission is polarized. (vi) The size of the detected emission peak is limited by diffraction.

Fluorescent dyes [93], quantum dots [119], gold particles [89], or latex beads used as label in single molecule experiments are generally smaller than the optical resolution

limit coming from diffraction.

Single-molecule microscopy is a subdiffraction imaging technique. Even if the measurement is performed on a standard optical microcopy system, single-molecules can be localized with a precision better than the diffraction limit as defined by Abbe (eq. 4.4).

4.2.2 Localization precision and spatial resolution

A single fluorophore can be considered as a point-source emitting photons upon excitation at appropriated wavelength. When an image is acquired through an objective (or a lens), the original object is convolved by a point spread function (PSF) to give the image. This effect is due to diffraction of light in the measurement system parts. This PSF is dependent on the measurement setup. Each setup has an associated PSF. In the focal plane, a theoretical PSF can be estimated by a function based on a Bessel function of the first kind ($J_1(r.a)$) (eq. 4.1 and 4.2) [126], which depends only on the wavelength of emitted light (λ), and the numerical aperture of the objective (NA). The image obtained from a single fluorescent molecule with an objective is the PSF of the objective.

$$PSF(r) = \left(\frac{2J_1(r \cdot a)}{r} \right)^2 \tag{4.1}$$

$$a = \frac{2\pi \cdot NA}{\lambda} \tag{4.2}$$

The lateral resolution limit (Δr) describes the different distance necessary to discriminate two fluorescent emitters. This limit has three definitions according to Sparrows, Abbe, and Rayleigh (eqs. 4.3 to 4.5). These limits are minimal distance needed between two adjacent molecules to distinguish them. This distance depends on the light wavelength (λ) and the numerical aperture of the objective (NA). It was first approximated by E. K. Abbe (eq. 4.4). Later, Rayleigh defined it as the distance between the maximum and the first minimum of the PSF. Sparrow defined it as the maximal distance where the PSF peaks of two adjacent emitters are unresolved. A summary of these limits is shown on figure 4.2 [127].

$$\Delta r = 0.48 \cdot \frac{\lambda}{NA} \tag{4.3}$$

$$\Delta r = 0.5 \frac{\lambda}{NA} \tag{4.4}$$

$$\Delta r = 0.61 \cdot \frac{\lambda}{NA} \tag{4.5}$$
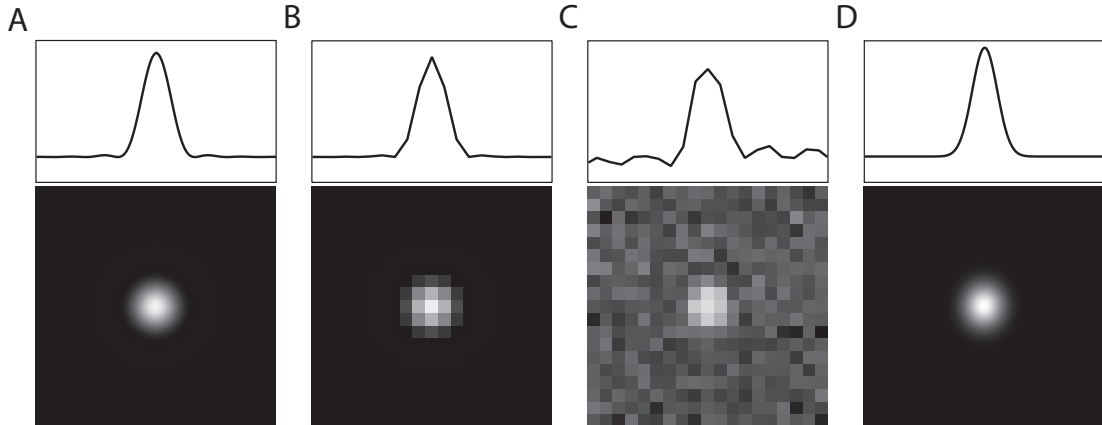
Figure 4.1: Profile and image of the estimated point spread function of a single fluorescent molecule All profiles are taken horizontally through the center of the image. **A.** PSF for a dye emitting at 647 nm detected with an objective with a NA=1.2 estimated with a order 1 Bessel J function. **B.** Calculated function on a CCD detector with 6.5 μm pixel and a 63x objective. **C.** The same as B with a Gaussian noise added to obtain a signal-to-noise ratio of 10. **D.** 2D-Gaussian function obtained after fitting the PSF showed on C.
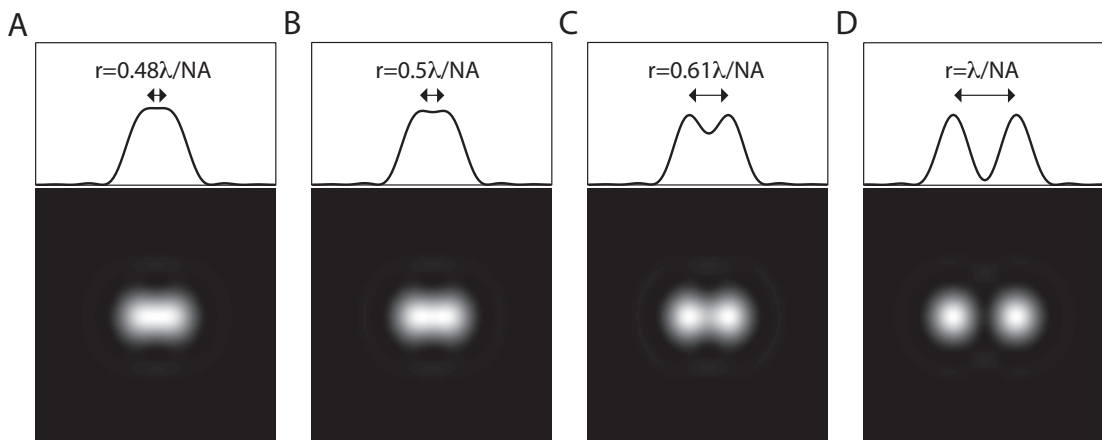
Figure 4.2: Different definitions of the diffraction limit. The distance r between two PSF is set to the different definitions of the diffraction limit **A.** Sparrow limit (eq. 4.3). The two PSF make a single peak. It is the largest intermolecular distance were only one broadened peak is visible on x-profile with these objective and wavelength. **B.** Abbe limit. This distance has been determined empirically by Abbe as the resolution limit of a lense (eq. 4.4). **C.** Rayleigh limit. The maximum of one PSF is exactly at the first minimum of the other (eq. 4.5). **D.** The two peaks are totally resolved when r=λ/NA. The top row show the profile along x-axis and the bottom row the x-y intensity plot.

The resolution limit is not a particularly limiting drawback in single-molecule imaging. It only implies that the observed molecule must be separated enough to avoid intermolecular distance smaller than the resolution. This can be achieved by proper dilution of the molecules as described in chapters 6 and 7.

Usually, a PSF is approximated by a 2D-Gaussian (eq. 4.6). z_0 is the minimum of the function corresponding to the background; A_0 the peak intensity; x_0 and y_0 the coordinates of the maximum; σ_x and σ_y the width in the corresponding directions and *cor* is a correlation parameter related to the orientation of the function.

$$
\begin{aligned}
z(x,y) &= z_0 + A_0 \cdot exp\bigg(\Big(\tfrac{-1}{2 \cdot (1-cor^2)} \Big) \cdot \Big(\big(\tfrac{x-x_0}{\sigma_x} \big)^2 + \big(\tfrac{y-y_0}{\sigma_y} \big)^2 \Big) \cdot \\
&\quad \cdot \Big(\tfrac{2 \cdot cor \cdot (x-x_0) \cdot (y-y_0)}{\sigma_x \cdot \sigma_y} \Big) \bigg)
\end{aligned}
\tag{4.6}
$$

Despite the large width due to light diffraction of the function, the position of the maximum of this Gaussian curve can be determined with a high accuracy. This maximum is the most probable position of the single fluorophore. As the PSF describes the probability distribution of the photon emitted by the fluorophore, the localization accuracy increase with the number of photons detected.

The theoretical maximal localization accuracy (δ_r) is given by equation 4.7 [128], where η the efficiency of the detection pathway, A the photons emission rate and t_{aq} the acquisition time. However, in practice this limit is never reached due to experimental noise.

$$
\delta_r = \frac{\lambda}{2 \cdot \pi \cdot NA \sqrt{\eta \cdot A \cdot t_{aq}}}
\tag{4.7}
$$

4.2.3 Noise sources

There are numerous noise sources present during single-molecule experiments, like shot-noise, noise coming from sample or optics, and noise provoked by the detector.

The shot noise is inherent to the nature of the light. A given light intensity corresponds to an average number of photon during a given time. The real number of photons during fraction of this time is distributed according to a Poisson distribution. This noise source will be particularly important with small number of photons. This noise cannot be reduced by technical improvements.

For measurements on living cells, the most important problem stems from cellular autofluorescence. This fluorescence arises from the existence of highly fluorescent molecules in cells (e.g. degradation intermediate, flavins). This problem can be reduced by the choice of appropriated fluorescent probes emitting at long wavelengths (> 650 nm), by measuring only healthy cells and by the use of non-fluorescent buffers and media.

Undesired fluorescence, residual excitation light, or stray light can also arise from the measurement system (objective, filter, lenses, dust). These noise sources can be reduced by using better optical parts and other technical improvements.

Generally used detectors in single-molecule tracking experiment are CCD cameras. Three major noise sources stem from this type of detector. (i) Dark noise stems from impurities in the semi-conductor material used, and happens when thermal energy promotes an electron to the conduction band without absorption of a photon. This noise can be reduced by cooling the detector. (ii) Electronic noise arises during the conversion of the promoted electron to a measurable current in the readout and amplification steps. (iii) Readout noise is due to the accumulation of charges in the CCD. Electron multiplying CCD (EMCCD) cameras have been developed to reduce the electronic noise by amplifying the electrons before the readout, thus increasing both the signal (N) and the SNR.

All these different noise sources add up. The position accuracy of a single molecule is strongly dependent on the signal-to-noise ratio (SNR). The effect of noise is shown in figure 4.3, where simulated images of PSF with different SNR have been fitted by a 2D Gaussian curve at different SNR.

Generally, in a system limited by the shot noise, which arises from the quantum nature of light, the error on the position decreases with $\sqrt{N}$), in a background limited measurement, it decreases with the number of photon N.

4.3   Single-molecule tracking in living cells

Single-molecule measurements give as a result the position of a particle in the cell membrane. In the plasma membrane, molecules are moving in two dimension. When a sequence of images is taken, it is possible to track the motion of this particle in time. Several parameters can be extracted from this trajectory like the diffusion coefficient (D), length of confinement (L_c), velocity (v), or abnormality (several parameters) [129].

Membrane spanning proteins undergo complex trajectories, with time or localization dependent parameters. Trajectories extracted from these molecules require elaborated analysis methods.

4.3.1   Diffusion

The diffusion coefficient is the most accessible parameter. Its measurement does not require necessarily single-molecule resolution. Many diffusion coefficient of proteins have been measured by fluorescent recovery after photobleaching (FRAP) [87] or FCS [130].

However, diffusion of a single-molecule gives information of the distribution of the
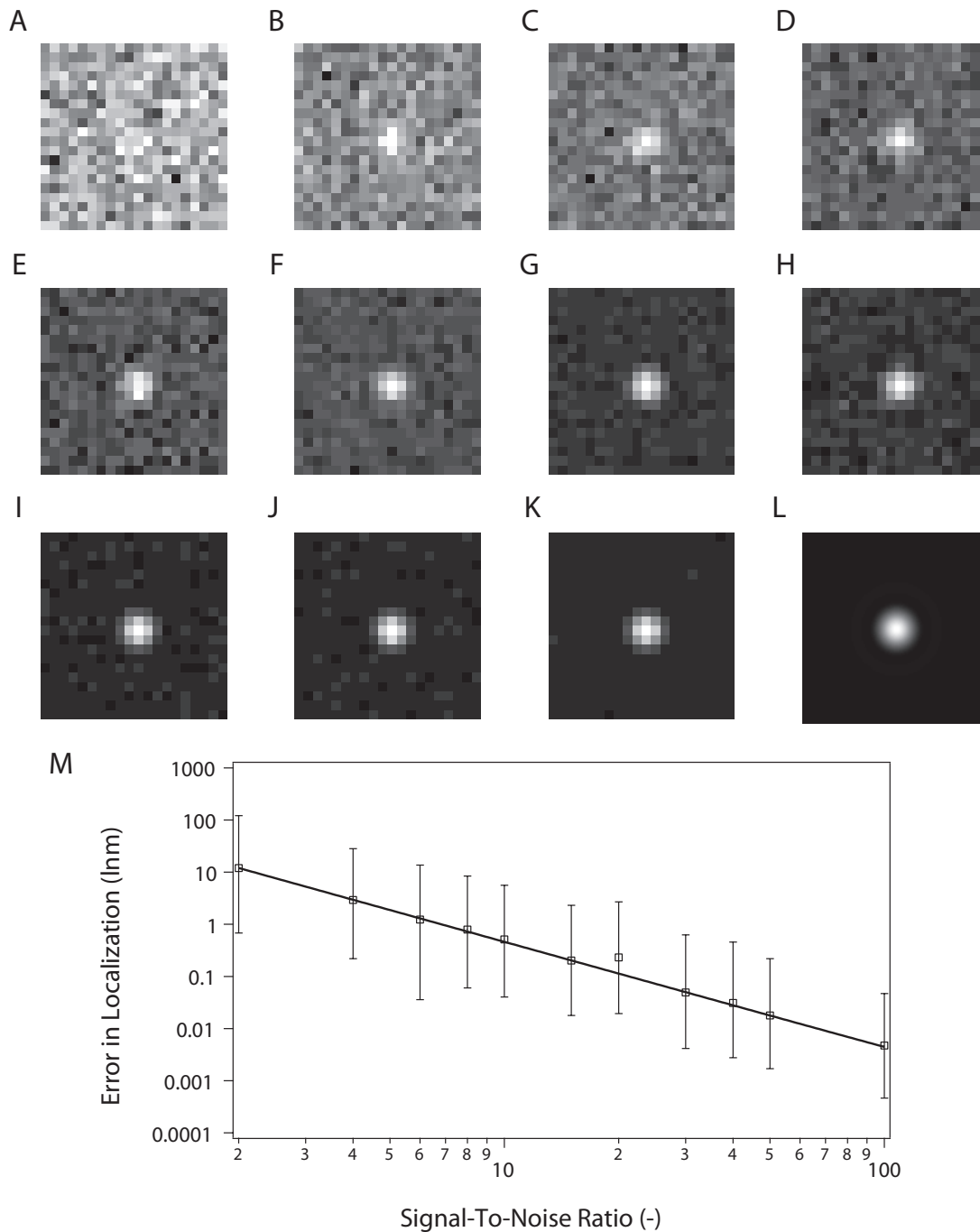
Figure 4.3: Effect of signal-to-noise ratio effect on position accuracy. An artificial PSF has been simulated (**L**), then the corresponding CCD image was calculated considering the pixel size correspond to the features of our microscopy setup. Noise has been added on the simulated CCD image. **A.** SNR=2. **B.** SNR=4. **C.** SNR=6. **D.** SNR=8. **E.** SNR=10. **F.** SNR=15. **G.** SNR=20. **H.** SNR=30. **I.** SNR=40. **J.** SNR=50. **K.** SNR=100. **L.** Original PSF. **M.** Log-log representation of the error in localization vs the SNR. For each SNR, 1000 PSF with randomly added noise were fitted with a 2D gauss. The value represented is the average of σ_r. The error bars are the 95% confidence intervals.

coefficient of diffusion and how it might change in time. In two-dimensional systems, the position in time of a particle performing Brownian is described by the probability distribution of the position, r, with time, t (eq. 4.8).

$$p(r,t)dr = \frac{1}{4\pi Dt} \ \exp\left(-\frac{r2}{4Dt}\right) 2\pi rdr \tag{4.8}$$

The probability distribution for a molecule experiencing an additional drift of velocity, v, in the x direction is shown on eq. 4.9

$$p(x,y,t,V)dxdy = \frac{1}{4\pi Dt}exp\left(\frac{(-(x-Vt)^2+y^2)}{4Dt}\right)dxdy \tag{4.9}$$

The probability distribution for a particle diffusing in a domain with reflecting boundaries is more complex. The mathematical development leading to eq. 4.11 has been established by Kusumi et al. [91].

Four general types of diffusion are possible for an object diffusing in a two-dimensional space [129]. This classification describes only homogenous diffusion, whereas motion in living cells plasma membrane is generally evolving with time or a mixture of diffusion types. Diffusion parameters are generally calculated using MSD vs t_{lag} graphs (fig. 4.5), fitted with equations 4.10 to 4.13. However, long traces can be analyzed according to properties of their statistical moments [131] (see section 4.5.4).

4.3.2   Brownian diffusion

Single-molecules undergoing Brownian motion are characterized by a linear relation of their mean square displacement with time lag with a slope proportional to the diffusion coefficient D_0 (eq. 4.10)

$$\text{MSD}\,(t_{lag}) = 4 \cdot D_0 \cdot t_{lag} + noise \tag{4.10}$$

4.3.3   Confined diffusion

In living cells, plasma membrane proteins are often confined in domains. This behavior has been described as a picket and fence associated diffusion, where motion of proteins is hindered by the presence of others membrane components [9].

MSD vs t_{lag} graphs of single molecules diffusing in domains tend towards a horizontal asymptote. This curve depends on the shape of the confinement region. Eq 4.11 is simplified function for a square region of size L_c [132].

$$\text{MSD}\left(t_{lag}\right) = \frac{L_c^2}{3} \cdot \left(1 - exp\left(\frac{-12 \cdot D_0 \cdot t_{lag}}{L_c^2}\right)\right) + noise \tag{4.11}$$

4.3.4 Directed diffusion

Directed motion is observed when particles undergo either active transport or diffuse in a flow. For active transport, D is negligible compared to the velocity of the transport, v. When molecules diffuse in flow, D can be important with respect to D. The MSD vs t_{lag} graph is described by equation 4.12

$$\text{MSD}\left(t_{lag}\right) = 4Dt_{lag} + (vt_{lag})^2 + noise \tag{4.12}$$

4.3.5 Anomalous diffusion

Particles undergo anomalous diffusion when by transiently interact with their surroundings. These interactions lead to deviation from the linearity of the mean square displacement with time. A negative curvature arises from hindered diffusion by obstacle or by transient interactions and a positive curvature stems usually from transient transport events. Anomalous diffusion is characterized by a power law of exponent α in equation 4.13.

$$\text{MSD}\left(t_{lag}\right) = 4Dt_{lag}^{\alpha} + noise \tag{4.13}$$

In isotropic media anomalous diffusion is not dependent of the scale. In cells, interactions of the diffusing molecule with surrounding objects depend of the time scale. Thus, in cells α is related to the measurement length scale [133].

D, the coefficient of diffusion, obtained using Brownian, confined and directed fit is the initial diffusion coefficient. Due to the power law dependence, the value obtained using anomalous fitting is not an exact initial coefficient of diffusion, but rather a general indication on diffusion.

4.4 Data acquisition

4.4.1 Principles

Several methods have been used for single molecule imaging and tracking in living cells. Basically, all these techniques involve the same steps. The first step is to label the molecule of interest with a probe that can be detected and imaged on a microscopy setup (i.e. endogenous fluorophore, fluorescent dye, semi-conductor nanoparticle, gold bead, latex bead). The labeled objects (proteins, nucleotides, metabolites, lipids) have

to be diluted enough to be distinct in the measured image (discussed in chapter 6). In a second step, single molecules have to be detected and imaged with a microscopy setup (wide-field, TIRF, confocal) at a sufficient lateral resolution. Finally, single-molecules have to be identified, and their trajectories have to be calculated and analyzed.

4.4.2   Movie acquisition

Single-molecule measurements require high power illumination and a very efficient detection system. This has been achieved using a home-built microscopy setup (see section 3.5 and figure 3.2). This setup is composed of very efficient optical components (i.e. filters, mirrors, lenses or objectives), a laser excitation that can reach intensities of kW/cm^2 power at the sample plane and a low-noise and high quantum efficiency EMCCD camera.

Illumination power at 632.8 nm was kept at 0.5 kW/cm^2 during all the experiments on organic dyes (Cy5 and Atto647N). In measurements involving QD, the illumination power at 488 or 514 nm was set at 100 W/cm^2. Movies were acquired at an imaging rate of 20 Hz in frame transfer mode. The illumination time corresponding to this frequency was 49.86 ms. These parameters were kept constant for all experiments. The amplification of the EMCCD was set to 211 and the dynamic range of images was 12 bits.

Generally, only 300 frames were acquired per experiments to limit cell damage and avoid huge data files and subsequent long computing time. Depending on the probe used, experiments were repeated up to ten times on the same cell. In test experiments, QD have been tracked for up to 6000 frames, corresponding to 5 minutes of continuous tracking.

4.5   Analysis software

4.5.1   Data import

The detectors used in single molecule microscopy all generate data using their own file type. To avoid fastidious and time consuming file conversion steps, four file importers were written to import directly in Igor Pro the files generated by the detectors. So far, Roper .spe, Andor .sif, raw data and .tiff files are supported. The information contained in the header of Andor and Roper files are read and added in the Igor Pro data analysis file. After import, data are converted to a 32-bit signed format to simplify the subsequent calculations.
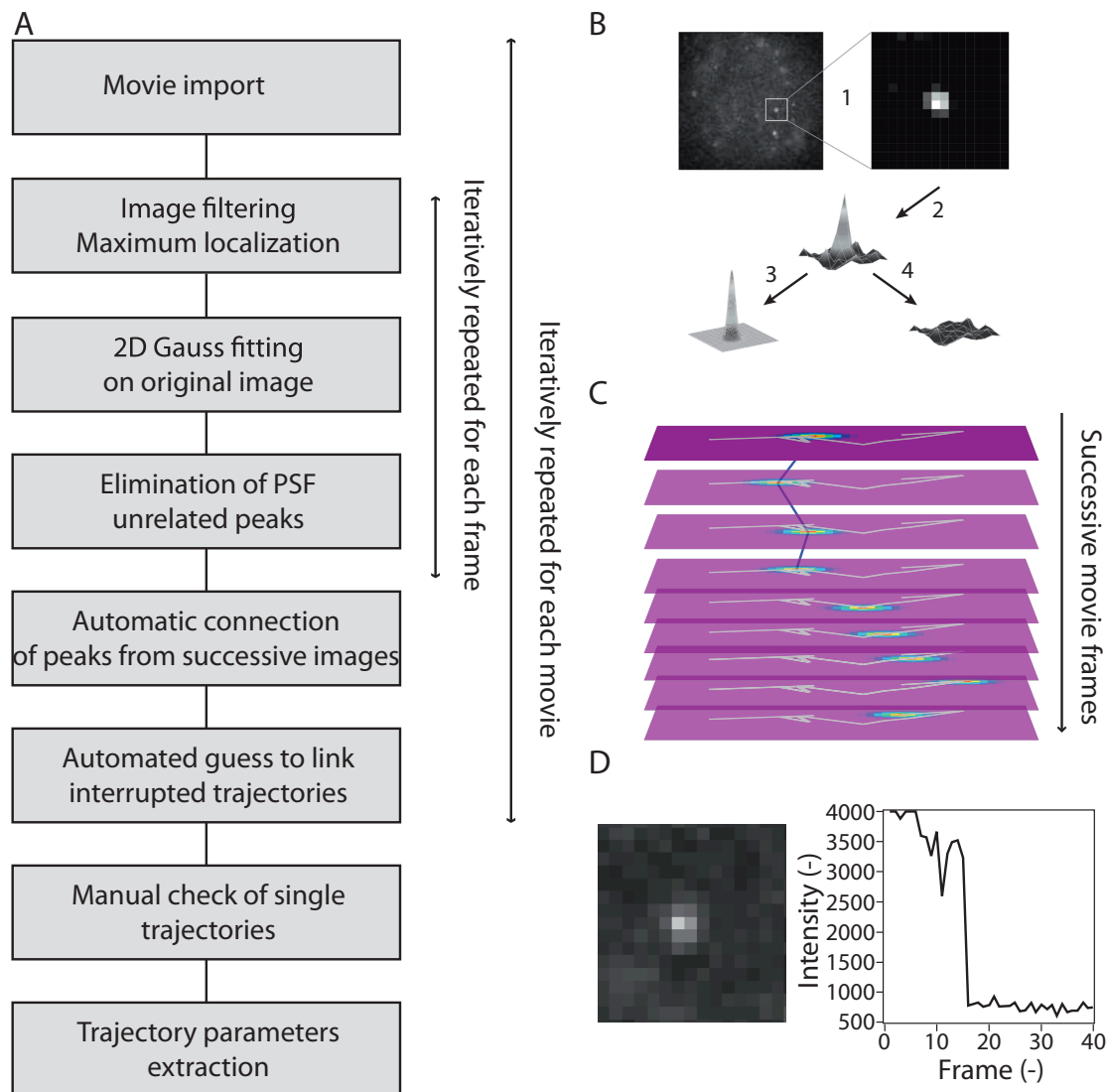
Figure 4.4: Single-molecule tracking software features. **A.** Flowchart of the single molecule software. All the steps involved in trajectory extraction are shown. **B.** Localization and fitting of fluorescent peaks. Fluorescent peaks (1) are first localized (2), then fitted with a 2D-Gaussian, yielding a distribution (3), and remaining noise (4) **C.** Trajectory extraction. Peaks of frame 1 are used as base coordinate to search the closest peak in the frame 2. If the distance in inferior to a determined threshold, the analysis goes on between frames 2 and 3. This is repeated until trace interruption. **D.** Single photobleaching step of α-CnTx-GI-Cy5 bound to nACR in HEK cell. Single photobleaching is the most used verification of the single molecule nature of the tracked peaks.

4.5.2   Single molecule localization

The first step of single molecule localization is the extraction of the local fluorescence intensity maxima (fig. 4.4). Each frame is filtered to remove the long-range structure of the image as the laser intensity profile or autofluorescence region. The filtering can be done using two equivalent methods.

The whole image is filtered with a Gaussian filter of 12x12 kernel. The resulting image is subtracted from the original image yielding a filtered image. These two steps can be replaced by a single step Fourier filter to obtain a comparable filtered image.

The filtered image does not contain long range structure but the small size fluorescence peaks are still present. The coordinates of the maximum of the filtered image are stored as potential single molecule loci. The intensity of the image region around the maximum coordinate is set the the minimum value of the image. This maxima localization procedure is repeated with an iterative loop until a given number of iterations or when the image maximum value fall above a determined threshold (calculated from the average peak size). This process is repeated for each frame of the movie.

Each of the stored maximum coordinate is then used as initial position value to fit the original image with a 2D Gaussian (eq. 4.6). During this step, peaks which shape does not correspond to a PSF are eliminated. These peaks are generally too broad (cellular autofluorescence and peaks with too low SNR) or too narrow (CCD or cosmic spikes). All the resulting maximum coordinates are stored and kept for further analysis.

4.5.3   Trajectories extraction

Trajectories are reconstituted by linking fluorescent peaks in successive frames (fig. 4.4C) [92]. This procedure is named tracking [134]. A molecule's position in the first frame is compared to the positions of maxima on the second frame. If the closest distance between position in the successive frame is smaller than a predefined threshold, they are considered to belong to the same molecule. When more than one molecule lie within the threshold, the linking procedure is interrupted. The same procedure is applied between the second and the third frame and over the whole movie. Uninterrupted trajectories of single molecules are stored as track.

The tracking algorithm only constructs uninterrupted trajectories. However, it might be that trajectories are interrupted for one or several frames yielding subtrajectories. These interruptions have multiple sources like blinking, detector noise, error of fitting procedures, or variations in cell autofluorescence lowering the SNR.

Many automated procedures that link subtrajectories have been developed (e.g. [135, 136, 137]). All proteins studied in this thesis exhibited complex trajectories. In order to simplify subtrajectories linking, two procedures were implemented. Immobile molecule were linked using a procedure linking the positions of the beginning of subtrajectories

over the whole movie. Subtrajectories of mobile molecules were linked by looking for the nearest subtrajectory beginning after the end of the current subtrajectory. The correlation factor of the square displacement vs the first time intervals of the MSD curve was used as a first test for subtrajectories linking likelihood. In case of doubt, subtrajectories linking were controlled by the users.

Several parameters can be used to determine whether one or more fluorophores are present like single-step-photobleaching, polarization properties, bunching, or anti-bunching [138]. Among all these parameters single-step photobleaching is the easiest to implement (fig. 4.4). All the traces acquired in experiments with organic dyes were tested for single step photobleaching. Quantum dots were tested with their blinking properties.

4.5.4 Trajectories analysis

The most simple mean to analyze a single-molecule trajectory is to plot the mean square displacement (MSD) for all time intervals. The mean square displacements are calculated for each time interval (t_{lag}) using eq. 4.14, where r is the position of the particle.

$$\text{MSD}(t_{lag}) = \frac{\sum_{t_i - t_j = t_{lag}} \left(r(t_i) - r(t_j)\right)^2}{\sum_{t_i - t_j = t_{lag}}} \qquad (4.14)$$

Single molecules moving with constant diffusion parameters can be entirely described using the MSD vs t_{lag} curves. In real measurements, two major problems strongly complicates the analysis. (i) Measurements involving organic dyes with high photobleaching rates only give short trajectories of a few dozens of frames, such that only a limited number of points are obtained, which is not sufficient for the accurate determination of the MSD for a given t_{lag}. Measurements on longer time scales, e.g. QD tracking, can show change in diffusion mode. In both cases analysis of single traces by using MSD vs t_{lag} is not valid.

Short trajectories analysis — Information contained in short single-molecule trajectories can be extracted by method based on the cumulative distribution of the square displacement for each t_{lag}developed by Schmidt and coworkers [86]. The probability to find a molecule in circle of radius, r, after a time, t_{lag} is defined by eq. 4.15, where r_0^2 is the mean square displacement at this t_{lag} [92].

$$P\left(r^2, t_{lag}\right) = 1 - exp\left(\frac{r^2}{r_0^2\left(t_{lag}\right)}\right) \qquad (4.15)$$

This model was extend to calculate the probability to find a molecule in a circle of radius r after t_{lag} when two types of molecules diffuse with diffusion coefficient D_1

and D$_2$ (eq. 4.16) where r_1^2 and r_2^2 are the respective mean square displacement at the measured t_{lag} α is the fraction of molecule of having a diffusion coefficient equal to r_1^2 (fig. 4.5B)

$$P\left(r^2, t_{lag}\right) = 1 - \left(\alpha \cdot exp\left(\frac{r^2}{r_1^2\left(t_{lag}\right)}\right) + (1 - \alpha) \cdot exp\left(\frac{r^2}{r_2^2\left(t_{lag}\right)}\right)\right) \qquad (4.16)$$

The validity of this method has also been demonstrated in the case of non-Brownian diffusion [132].

Analysis of long trajectories — Single molecules imaged for a sufficiently long time (> 50 frames) can be analyzed at the single trajectory level after extracting diffusion parameter from the MSD vs t_{lag} curve. MSD of trajectories of freely diffusing molecules are linearly dependent to t_{lag}. The addition of a velocity of constant direction does not complicate fitting. Thus, in these cases, analyze is straightforward. When single molecules are confined or diffuse with an anomalous behavior, the fit is less robust; the initial value for curve fitting becomes important. However, an algorithm was implemented to prevent fit divergence.

The single trajectory analysis module works in two successive steps. First, all the single molecule MSD vs t_{lag} curves are calculated and fitted with a linear function. The initial coefficient of diffusion, D_{init}, and the noise dependent y-intercept are extracted. This linear fitting is performed on a limited part of the t_{lag} axis. Initially, only the first five points are fitted. Then the sixth value is added and the fit quality is evaluated with the correlation coefficient. If the correlation coefficient decrease after the addition of the point, the iteration loop stops and the values obtained before the last fit are kept. If there is no decrease, the next point is added. If no deviations from the linearity are observed until t_{lag} value of the first third of available t_{lag} range is reached, the loop stops and the last D value is kept. This procedure was implemented after the observation of bias after fits on the shorter MSD only (unpublished results).

During the second step, all the MSD vs t_{lag} curves are fitted with functions for confined, directed and anomalous diffusion. These fits are performed using the initial diffusion coefficient and the noise value as guess. In certain case, it was also possible to set the noise at the value obtained by linear fitting to diminish the degree of freedom of the fit algorithm. The results of these fits were stored for each trajectory. The single-molecules are then classified according to the D and L values obtained in the previous fitting steps.

Moment scaling-spectrum (MSS) method is the analysis of the moment of displacement vs t_{lag}. In the MSD vs t_{lag}, only the moment of order two is analyzed as it is growth linearly with time [131]. This MSS slope give a direct and detailed information
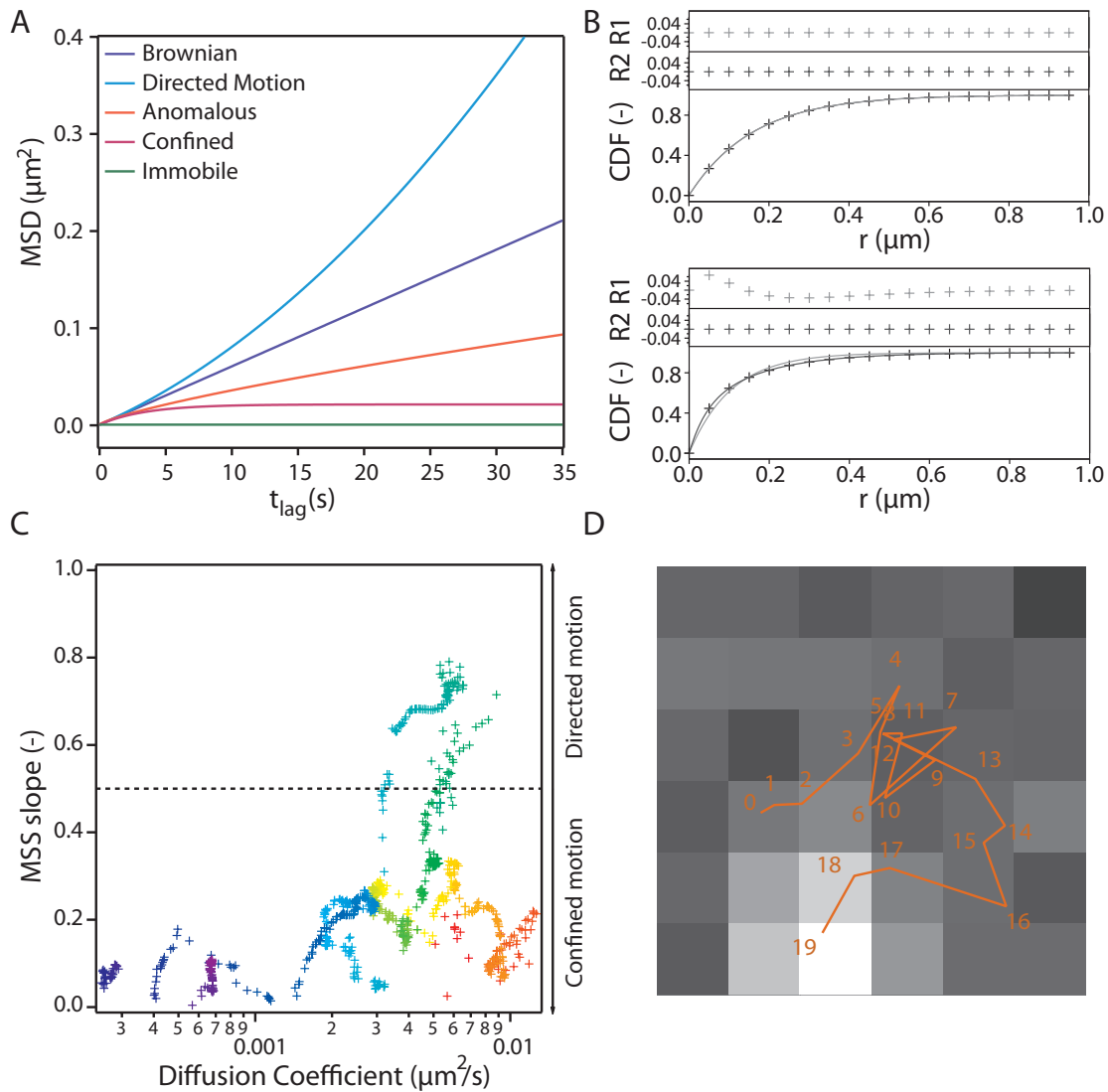
Figure 4.5: Information extracted from single-molecules A. Examples of standard modes of diffusion observed in plasma membrane of cells. In all cases, the diffusion coefficients is D=0.0016·10^{-2} $\mu m^2/s$. The confinement length of the confined molecule is 250 nm, the anomalous factor α=0.75, and the velocity of the directed motion is v=100 nm/s. **B.** Cumulative distribution of square displacement. The top graph depicts the distribution of r^2 of a single population of molecules diffusing with D_1=0.04 $\mu m^2/s$. The bottom graph shows the distribution when 40% of the molecule diffuses with D_2=0.001 $\mu m^2/s$. In both graphs, the grey residual (R1) stems from a single-exponential fit (eq. 4.15) and the black residuals (R2) from a double-exponential fit (eq. 4.16). **C.** Single-trace moment analysis of $5HT_3R$ diffusing in the plasma membrane of HEK cells. This trace was extracted from a receptor labeled with a *tris*-NTA-QD affinity ligand. The receptor undergoes changes between strongly confined to directed motion.

on the type of motion experienced by the protein of interest. When this slope is equal to 0.5 the molecule is moving with Brownian motion, a slope of 1 is characteristic of fully directed motion and a slope of 0 means no motion. Values between 0 and 0.5 come from molecules diffusing confined regions. Values between 0.5 and 1 describe molecules diffusing in flow. This MSS analysis can be performed on trajectories with at least 60 available t_{lag}. For shorter traces, the analysis is not robust enough [131].

4.5.5   Single-trace segmentation

There are several means to analyze changes of diffusion mode in a single trajectory. All the methods apply a segmentation process, which cuts sequentially the original trajectories in smaller subtrajectories. When a long trajectory is cut in shorter trajectories of 100 frames, the first subtrajectory goes from 0 to 100, the second from 1 to 101, this process is repeated iteratively until the higher value reach the last frame of the trajectory. These subtrajectories are analyzed as single traces. With this method, it is possible to extract information on time-dependent evolution of the diffusion.

MSS analysis can be used on segments of a trajectory, so that the type of diffusion with time can be followed (fig. 4.5C)

4.6   Discussion

Accuracy is essential in single-particle tracking experiments. Increases in accuracy can help to decipher new cellular processes. This parameter is particularly important during tracking of confined proteins. Membrane are composed of domains formed by lipids [139] and through cytoskeletal interactions [9]. Improvements in the lateral precision of single molecule microscopy allow the visualization of these nanometric structures. The accuracy is also essential to measure distance between molecules separated by a few tens of nanometers and in co-localization experiments.

The precision of a measurement is strongly dependent on signal-to-noise ratio (fig. 4.3). In an ideal system, the majority of the noise comes from the detection system, light path and detector, which can be improved by technical means. Measurements in living cells deal with uncontrollable noise sources like autofluorescence or cell movements. Furthermore, the use of organic dyes, which have very interesting (small) size and spectral properties, is complicated by the slow rate of photon emission and fast photobleaching. The dynamic range of the majority of the detectors is limited to 8 or 12 bit.

The single particle tracking methods require robust fitting procedures. Instability in fitting procedures can induce artifacts, particularly in the localization steps. The same problem can occur during analysis of trajectories.

The tracking procedure that links the fluorescence maxima to extract trajectory is

a very sensitive step. Errors in trajectory extraction have dramatic effects on the final results.

Most of the analysis techniques are somehow based on the hypothesis that molecules diffusing in cell plasma membrane undergo Brownian diffusion. The time scale dependency of lipid diffusion measured by nanovid microscopy in living cell suggest more complex mechanism of diffusion [140].

The length of the trajectories has a huge effect on the quality of the measurements. Complex analysis performed on too short traces can introduce bias in measurements.

During the last five years the time necessary to analyze single-molecule data has been reduced by constant improvement of the procedures used and the user interface.

4.7   Conclusion

Many improvements in single-molecule tracking and analysis methods in our lab have been made during the last ten years, yielding new ways of localizing and tracking single-molecules in living cells. The analysis procedures used in this thesis are simple and reproducible. Important information is obtained from different types of experiments. The software accepts in principle all types of data formats. Furthermore, the high adaptability and modular features of the procedures used allow constant implementation of additional methods.

Fluorescent energy transfer in living cells

5.1 Introduction

Resonance energy transfer has been discovered in 1932 by Perrin [141] and later explained by Förster in 1948 [142, pages 148-158]. FRET gives the possibility to measure very accurately distances in the nanometer range. This ability has been exploited for motion and distance measurement as well as to detect molecular interactions.

This chapter will focus on the analysis of FRET images with a small designed software.

5.1.1 Förster resonance energy transfer (FRET)

Förster resonance energy transfer (FRET) is a dipole-dipole interaction between two non-identical chromophores. It is a radiationless transfer of an energy quantum. There are no thermal and radiative energy conversion or collision between the two implied molecules. This energy exchange is strongly dependent on the distance and the relative orientation of emission and absorption dipoles of the donor and acceptor, respectively. The donor is the dye that absorbs a photon, the acceptor is the molecule that receives the transferred energy and under certain conditions re-emits a lower energy photon [143].

5.1.2 FRET theory

The FRET efficiency (E) is the ratio of energy transfer rate over the sum of the deactivation rates of donor's excited state (fig. 5.1 and eq. 5.1). It represents the fraction of the photons absorbed by the donor that can induce the promotion of an electron of the acceptor into an excited state.
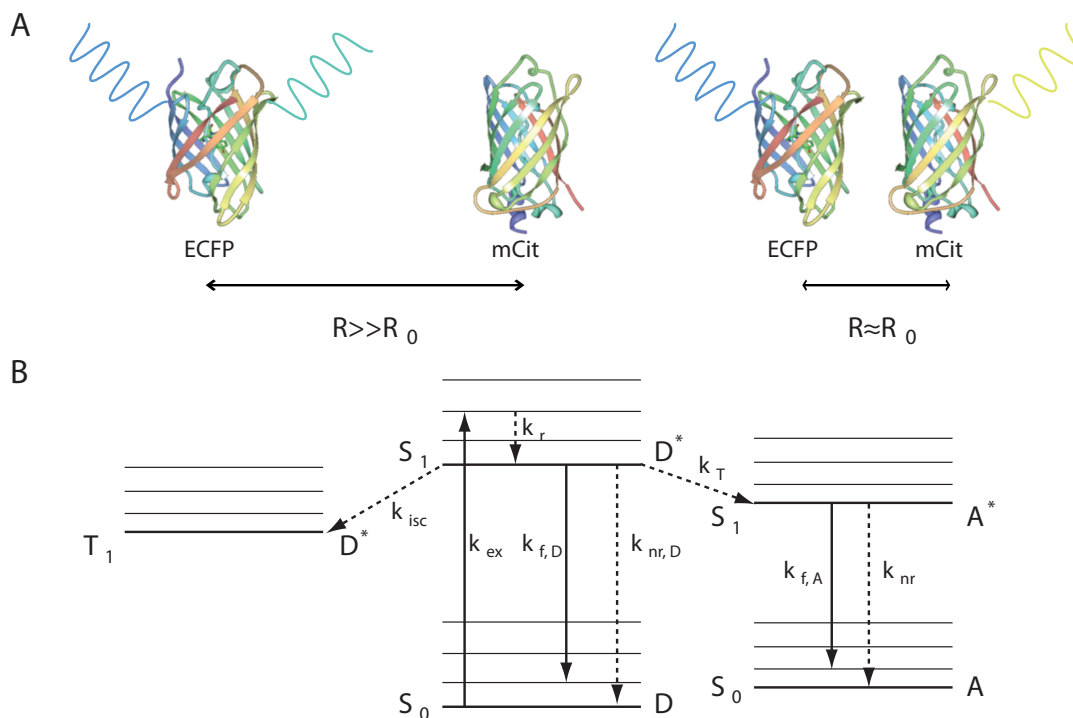
Figure 5.1: Principle of FRET. A. When the distance between the donor and acceptor is large, no transfer occurs. Whereas, when the two chromophore are in close proximity, energy is transferred from the donor to the acceptor. In this example, ECFP acts as donor and mCitrine as acceptor. mCitrine emits a photon after energy transfer. **B.** The Jablonski diagram indicates the energy levels and energy transitions implicated in FRET. Straight lines show radiative transitions (including absorption) and dashed line stands for non-radiative energy transitions. When the donor absorbs a photon, an electron is promoted from the singlet state ground, S_0, to a higher energy electronic level, S_1. After the fast vibrational relaxation (k_r), the electron is in the lowest level of the donor excited state S_1. Spontaneous relaxation of the excited state can follow different ways; non-radiative when the relaxation occurs without emission of a photon (k_{nr}), radiative when a photon is emitted (k_f). The relaxation also happens through the conversion to triplet state, T_1, by intersystem crossing (k_{isc}). FRET occurs when the energy is transferred to an adjacent molecule, which in turn becomes excited.

$$E = \frac{k_T}{k_T + k_{f,D} + k_{nr,D} + k_i sc} \tag{5.1}$$

The rate of energy transfer between donor and acceptor molecule depend strongly on the distance between them (fig. 5.1). Equation 5.2 shows the rate of energy transfer k_T as a function of the distance, R, between the chromophores. τ_D stands for the inverse of the donor decay rate when the donor-acceptor distance is equal to R_0.

$$k_T(r) = \frac{1}{\tau_D} \left(\frac{R_0}{R} \right)^6 \tag{5.2}$$

R_0 has been defined as a function of the donor quantum yield Q_D, an orientation factor κ^2, relating the orientation of the donor emission dipole and the acceptor excitation dipole, the refraction index of the surrounding media$n$, the Avogadro's number N_a, and an overlap integral J (eq. 5.3), which depends on the normalized fluorescence spectra F_D, and the molar extinction coefficient ϵ_A(eq. 5.4).

$$R_0^6 = \frac{9000(\ln 10)\kappa^2 Q_D J}{128\pi^5 n^4 N_a} \tag{5.3}$$

$$J = \int_0^\infty F_D(\lambda)\epsilon_A(\lambda)\lambda^4 d\lambda \tag{5.4}$$

In a system implying only one donor and one acceptor, the efficiency of FRET is related to the distance, R, between the two dyes (eq. 5.5).

$$E = \frac{R_0^6}{R_0^6 + R^6} \tag{5.5}$$

FRET efficiency can be determined from several experimental observables. It is related to the lifetime of the donor in presence τ_{DA}, and in absence of an acceptor τ_D (eq. 5.6).

$$E = 1 - \frac{\tau_{DA}}{\tau_D} \tag{5.6}$$

It can also be calculated with the fluorescence of the donor in presence F_{DA}, and in absence F_D, of an acceptor (5.7).

$$E = 1 - \frac{F_{DA}}{F_D} \tag{5.7}$$

When the acceptor is a fluorescent molecule, it can emit a photon during its excited state deactivation. The fluorescence of the acceptor in presence of the donor (F_{AD}) is enhanced by the energy transfer compared to the fluorescence of the acceptor (F_A) upon excitation of the donor. This emission F_{AD} is named sensitized acceptor emission [144]. E is then dependent on ratio of the molar extinction coefficients of the acceptor $\epsilon_A(\lambda)$ and donor $\epsilon_D(\lambda)$ at the excitation wavelength (λ) of the donor (eq. 5.8).

$$\mathrm{E} = \left(\frac{F_{AD}}{F_A}\right)\left(\frac{\epsilon_A(\lambda)}{\epsilon_D(\lambda)}\right) \tag{5.8}$$

Equations 5.2 to 5.8 are valid for a 1:1 stoichiometry of donor and acceptor and a random relative orientation of the dipoles ($\kappa^2 = 2/3$, eq. 5.3). A full discussion of those parameter can be found in "Resonance Energy Transfer: Theory and Data" [143].

Oligomers of a protein or protein assemblies with multiple interactions are typical non-stoichiometric system. In this case, the apparent FRET efficiency, E_{app}, depends on the molar fractions of donor, x_D, and acceptor, x_A, assuming an identical distance (R) between all the chromophores (eq. 5.9).

$$\mathrm{E}_{app} = \left(\frac{F_{AD}}{F_A}\right)\left(\frac{\epsilon_A(\lambda)}{\epsilon_D(\lambda)}\right)\left(\frac{x_D}{x_A}\right) \tag{5.9}$$

E_{app} varies with the molar fractions according to eq. 5.10, where n is the number of units of an oligomer randomly composed of donor and acceptor. It is thus possible to determine the oligomer composition by varying the molar fractions in sensitized emission measurements [144].

$$\mathrm{E}_{app} = \mathrm{E}\frac{x_D}{1-x_D}\left(1 - x_D^{n-1}\right) \tag{5.10}$$

5.1.3   FRET measurements in cells

Imaging FRET requires the ability to measure the parameters related to the FRET efficiency. There are many methods to obtain FRET related variables [145]. FRET is generally measured using three different microscope channels. The donor channel gives the fluorescence obtained by illuminating the sample with the donor excitation wavelength and measuring resulting signal at the donor emission wavelength. The FRET channel gives the fluorescence values obtained by illuminating the sample with the donor excitation wavelength and measuring the fluorescence signal at the acceptor emission wavelength. The acceptor channel gives the fluorescence values obtained by illuminating the sample with the acceptor excitation wavelength and measuring the fluorescence signal at the acceptor emission wavelength.

Valuable information can be extracted directly from the ratio between different channels (Donor, FRET, or Acceptor) or by intensity changes in a single channel. (i) For the measurement of inter- or intramolecular distances between two chromophores, the exact knowledge of E is required. (ii) Determination of interaction between two molecules does not always require the exact determination of E. The knowledge of the ratio between the donor and the acceptor channels is generally sufficient, when comparison between different experimental conditions are made. (iii) Determination of efficiency is not necessary to measure FRET change in time (e.g. FRET sensors, ligand binding). (iv) Measurements of oligomerization requires the determination of efficiency at different relative concentration of donor and acceptor, as well at different total donor and acceptor concentrations.

Intracellular interactions between proteins can be measured by FRET, using fluorescent derivatives of the proteins of interest. Proteins fused with the donor and the acceptor are transfected and FRET efficiency is measured in cells [146]. This method implies a very careful calculation of FRET efficiency. In cells very high local concentration of protein can be found, in this case it is possible to measure FRET between two proteins, when they are not directly interacting.

FRET-based fluorescent indicators have been developed for intra- and extra-cellular analyte quantification. The first "Chameleon" was designed to determine Ca^{2+} concentration [147]. Further development have permitted the construction of sensors for many kinds of molecules of interest. These indicators are generally based on a pair of fluorescent proteins linked by a peptide which undergoes a conformational change in the presence of the molecule of interest [99]. Knowledge of efficiency is essential only if absolute ions concentrations are needed. Therefore generally only the ratio of donor and acceptor channel are measured.

FRET experiments are shown on chapter 8 where fusion between fluorescent proteins, including a Ca^{2+} indicator have been measured in living cells.

5.1.4   Software principle

The purpose of this small FRET analysis software was to be versatile. In a laboratory, different imaging setups produce many different file types each with their own depth, pixel size, image size, color, header, or image order. This software has been designed to handle multiple file types and experiment kinds. A simple FRET experiment can be performed by measuring only the intensity of one fluorophore (donor, FRET, or acceptor), whereas data files resulting from complex FRET experiments often contain more images (donor fluorescence, FRET channel, transmission, acceptor fluorescence, fluorescent ligand or membrane probes).

The analysis software is composed of three modules (see fig. 5.2); (i) Data are

A

```
┌──────────────┐
│     Data     │
│  importation │
└──────┬───────┘
       │
       ▼
┌──────────────┐
│    Image     │
│  reordering  │
└──────┬───────┘
       │
       ▼
┌──────────────┐
│    Signal    │
│     ROI      │
└──────────────┘
```

B

```
┌──────────────┐
│   Original   │
│    images    │
└──────┬───────┘
       │
       ▼
      ╱◇╲
    ╱ Manual ╲
   ◇ background ◇
    ╲  ROI  ╱
  no ╲◇╱ yes
   ┌───┘   └───┐
   ▼           ▼
┌──────────┐ ┌──────────┐
│Automated │ │   ROI    │
│correction│ │selection │
└────┬─────┘ └────┬─────┘
     └───┐   ┌────┘
         ▼   ▼
     ┌──────────┐
     │Threshold │
     │   mask   │
     └──────────┘
```

C

```
┌──────────────┐
│  Threshold   │
│      +       │
│   ROI mask   │
└──────┬───────┘
       │
       ▼
┌──────────────┐
│    Image     │
│  filtering   │
└──────┬───────┘
       │
       ▼
┌──────────────┐
│   FR value   │
│ calculation  │
└──────────────┘
```
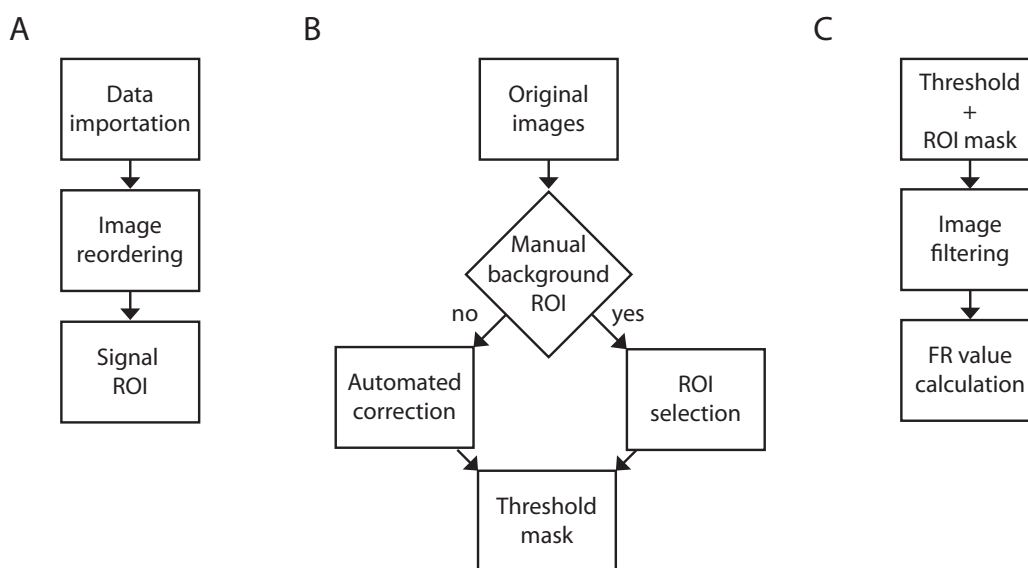
Figure 5.2: Flow chart of the three parts of the FRET analysis software. A. Images series are extracted from microscope file. They reordered and the background and signal regions of interest (ROI) are determined. **B.** Each frame of an image series is thresholded and the effective signal regions are added in a mask file. **C.** The original images are filtered and the FRET parameters are calculated. This process is repeated over the whole image serie.

extracted from microscope output files. (ii) Regions of interest (ROI) are selected. Image are corrected for background, thresholded to remove regions with insufficient signal, and, if required, filtered. (iii) FRET parameters are extracted from corrected images.

5.1.5   FRET imaging

In simple FRET measurements, particularly in case of change in energy transfer during the experiment, it is possible to extract all the information needed from the change in the donor and FRET channels. Furthermore, the change in the ratio between the two channels can be traced in time or with the addition of chemicals. This kind of experiment is called ratiometric.

When FRET is measured on a microscopy system, it is often complicated to separate totally the emission of the donor and the acceptor. The three-cubes method have been established to correct this experimental limitation [148]. This method implies the acquisition of three images, the donor excited by the donor channel (D), the acceptor excited by the donor channel (FRET) and the acceptor excited directly (A). For instance when the donor is ECFP and the acceptor is EYFP, D is the fluorescence intensity measured between 565 and 500 nm upon excitation at 458 nm, A is the fluorescence intensity mea-

sured between 525 and 605 nm upon excitation at 514 nm, and FRET is the fluorescence intensity measured between 525and 605 nm upon excitation at 458 nm.

In the most complex case, six corrections factors must be determined to calculate the efficiency. A good choice of donor and acceptor pair and filter set lead to a simplified version with only two correction factors; s_1 is the ratio of the fluorescence of the donor alone in the donor channel ($F_D(\lambda_D)$) to the donor alone in the FRET channel when illuminated with the donor excitation pathway ($F_{FRET}(\lambda_D)$) (eq. 5.11). This factor is a correction for the donor fluorescence bleed-through in the FRET channels. s_4 is the ratio of the fluorescence of the acceptor illuminated with the donor excitation pathway ($F_{FRET}(\lambda_D)$) to the fluorescence of the acceptor illuminated with the acceptor excitation pathway ($F_A(\lambda_A)$) (eq. 5.12). This factor is a correction for the direct excitation of the acceptor by the excitation channel of the donor. FR is the ratio of the sensitized acceptor fluorescence emission ($F_{FRET,D}$) to fluorescence of the acceptor in absence of the donor (F_{FRET}) (eq. 5.13) [144]. In the three equations (5.11, 5.12 and 5.13), F stands for fluorescence intensity and the subscript to the corresponding channel.

$$s_1 = \frac{F_D(\lambda_D)}{F_{FRET}(\lambda_D)} \tag{5.11}$$

$$s_4 = \frac{F_{FRET}(\lambda_D)}{F_A(\lambda_A)} \tag{5.12}$$

$$FR = \frac{F_{FRET,D}}{F_{FRET}} = \frac{F_{direct} + F_{FRET}}{F_{direct}} = \frac{F - S_1 \cdot D}{s_4 \cdot A} \tag{5.13}$$

FR is directly related to E_{app} (eq. 5.14).

$$E_{app} = (FR - 1) \cdot \frac{\epsilon_A(\lambda_D)}{\epsilon_D(\lambda_D)} \tag{5.14}$$

The FRET analysis software described here has been implemented with the two methods described above.

5.2 Data acquisition

Images, needed to determine FRET in cells, can be measured using all kinds of microscopy systems. For ratiometric measurement, at least two images must be acquired, a donor and a FRET image, both with the donor excitation channel. Image acquisition process is more complex to obtain efficiency of transfer. Indeed, three images must be acquired for each experiments, donor, FRET and acceptor (fig. 5.3A, E and D respectively). Furthermore, these three images must also be taken for samples with donor alone and with acceptor alone, and this for all microscope settings to calibrate the system with correction factors s_1 and s_4.

Studies implying the presence of oligomers requires experiments performed with several molar fractions of donor and acceptor and expression level.

5.3   Analysis software

5.3.1   Data importation

In a first step, image series are extracted from the microscope data file. These image series consist of frames containing all the images needed for FRET analysis for all the concentration or time interval depending of experiment type. Image extraction can be done by two means; the direct importation of a multiple image set or one by one. The calibration images for correction factors calculation are extracted using an independent importation module.

Microscope files resulting from acquisition software can be of multiple types and images can be in any order. A small routine has been written to reorder the image for each frame. Hence, each imported image is tagged as donor, acceptor, FRET or transmission (fig. 5.3A, B, C and D).

Two region are defined on the image series, a region of interest (ROI) and a background region. ROI are selected by the users. Background regions can be selected in two ways. They can be selected manually by the user or automatically. In automatic modes, the narrow low intensity normally-distributed peak is defined as background. Results of a typical automatic background removal is shown on figure 5.3G. In image series, this background selection module can be applied on the three images of each frame (D, FRET, A). In this case only regions where the three image lack fluorescence signal are taken into account as background.

ROI and background informations are stored as a mask. Masks are data array with a value of one for the interest pixels and "Not a Number" (NaN) for pixels not to be considered. Masks can be used at each subsequent steps of data analysis. Multiple masks can be used for signal ROI. This allow FRET parameter extraction on more than one region.

5.3.2   Data analysis

The correction factors required for three-cubes analysis can be calculated at any moment during the analysis. The fluorescence images (D, FRET, and A) of the donor alone excited by the donor excitation pathway and of the acceptor alone excited by both pathways are loaded independently. An automated routine calculates s_4 by linear fitting of the acceptor fluorescence excited with the donor excitation pathway vs the fluorescence of acceptor with direct excitation; s_1 is calculated by linear fitting of the donor in the
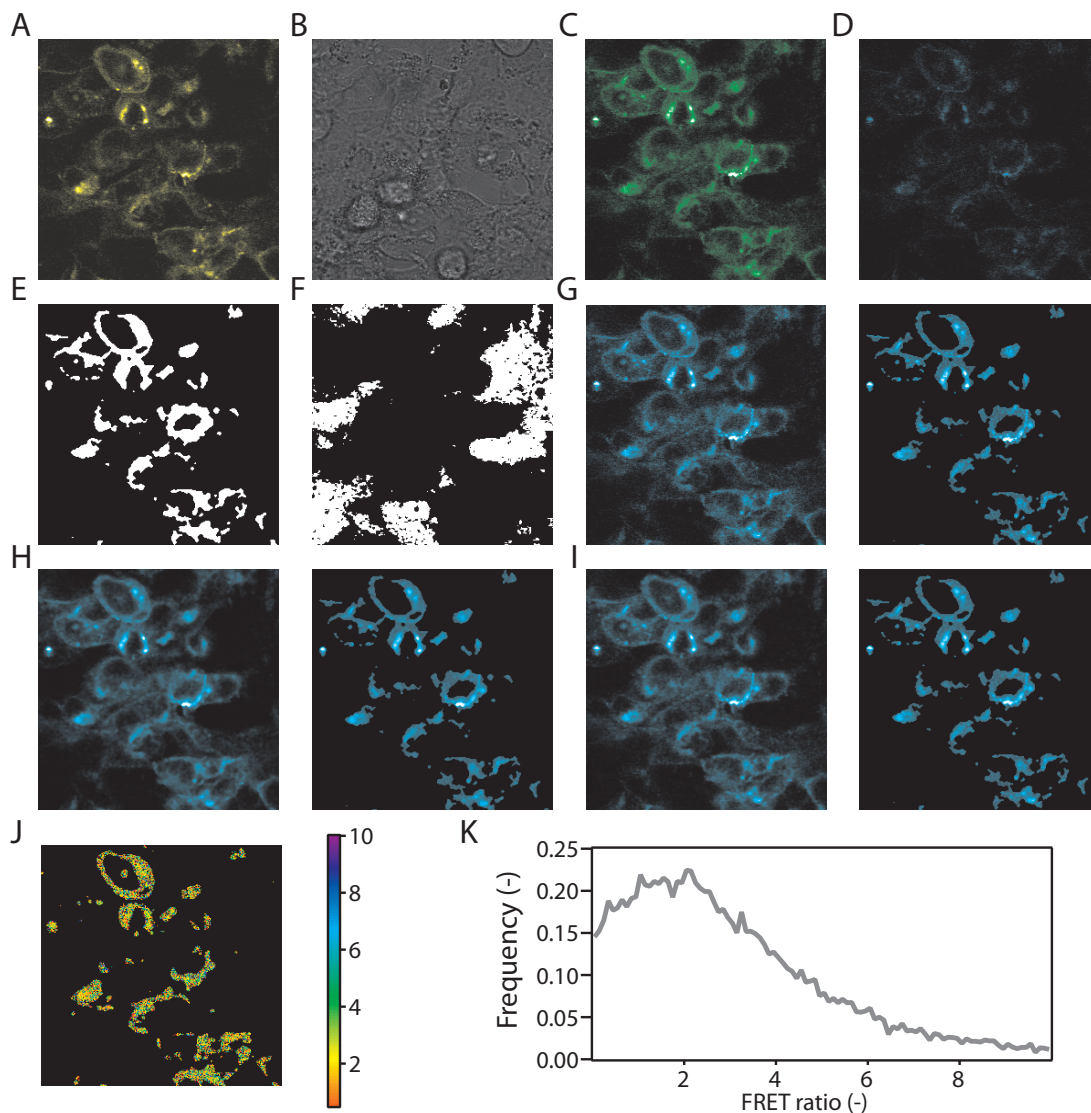
Figure 5.3: Images used during automated analysis. Two fluorescent subunits of the 5HT$_3$Rhave been transfected in HEK cells. These images show all the images used in the data treatment. The original channels are depicted in A, B, C, and D. **A.** Acceptor only channel. **B.** Transmission channel. **C.** Donor channel. **D.** FRET channel. **E.** Thresholding mask, pixels in white are treated as signal and black pixel are not use for analysis. **F.** Background mask, white pixels are treated as background. They are used for background identification in every image. **G.** Original FRET image before and after thresholding and background removal (right). **H.** Average filtered image. The original has been filtered using a 3x3 average filter (left). Resulting image after thresholding and background removal (right). **I.** Median filtered image. The image has been filtered with a median 3x3 filter (left). Resulting image after thresholding and background removal (right). **J.** Image of FRET ratio. **K.** Distribution of the FRET ration over the whole image K.

FRET channels vs the donor in the donor channel. Linearity of the bleed-through curves for s_1 and s_4 can be inspected by the user. Non-linearity indicates a bleed-through dependent on intensity, which generally stems from the measurement setup.

Two FRET analysis methods are used. The first is the determination of only ratio between acceptor and donor upon excitation with the donor excitation pathway, and the second is the three-cube method.

A ROI mask based on threshold of one image selected by the user is determinated. The default image is the FRET channel. The threshold can be determined either manually or with one of the five native automatic algorithms. The available methods are shown in table 5.1. A thresholding mask is made with the obtained signal values. This mask is used in every channel to remove non-interesting regions and avoid artifacts.

Table 5.1: *Available methods for thresholding.*

Name	Method
Iterative	Iteration of the level
Bimodal	Bimodal fit of the pixel values
Adaptive	Threshold calculated on every line portion
Fuzzy Entropy	Minimizing the fuzziness of the image with Entropy function
Fuzzy Means	Probability of a pixel to be either from signal or from background

FRET ratio is determined from the processed images. Ratio is calculated using four differently treated image sets. Each approach gives an average and a standard deviation. The FRET ratio is always calculated using equation 5.13. (i) The simplest is the mean value obtained after pixel by pixel division of unfiltered image (fig. 5.3G). (ii) The value obtained by the same division is used to construct an histogram of FRET ratio (fig. 5.3K). The division can also be made on images filtered with (iii) a 3x3 average (fig. 5.3H), or (iv) a 3x3 median (fig. 5.3I).

The results of all calculations are stored and can be used for further analysis. Images, including ratio images, can be exported as a movie or data set.

5.4 Discussion

5.4.1 FRET microscopy in living cells

FRET can be measured using different techniques. Among these methods, measurements in living cells give very precious and precise information about the distribution of properties between cells and inside a single cells. However, extracting FRET information from microscopy images is complex and requires very robust and reproducible analysis systems. The analysis software described here was set up to fulfill specific needs, partic-

ularly on measurements of protein oligomerization and on FRET evolving with time or experimental conditions.
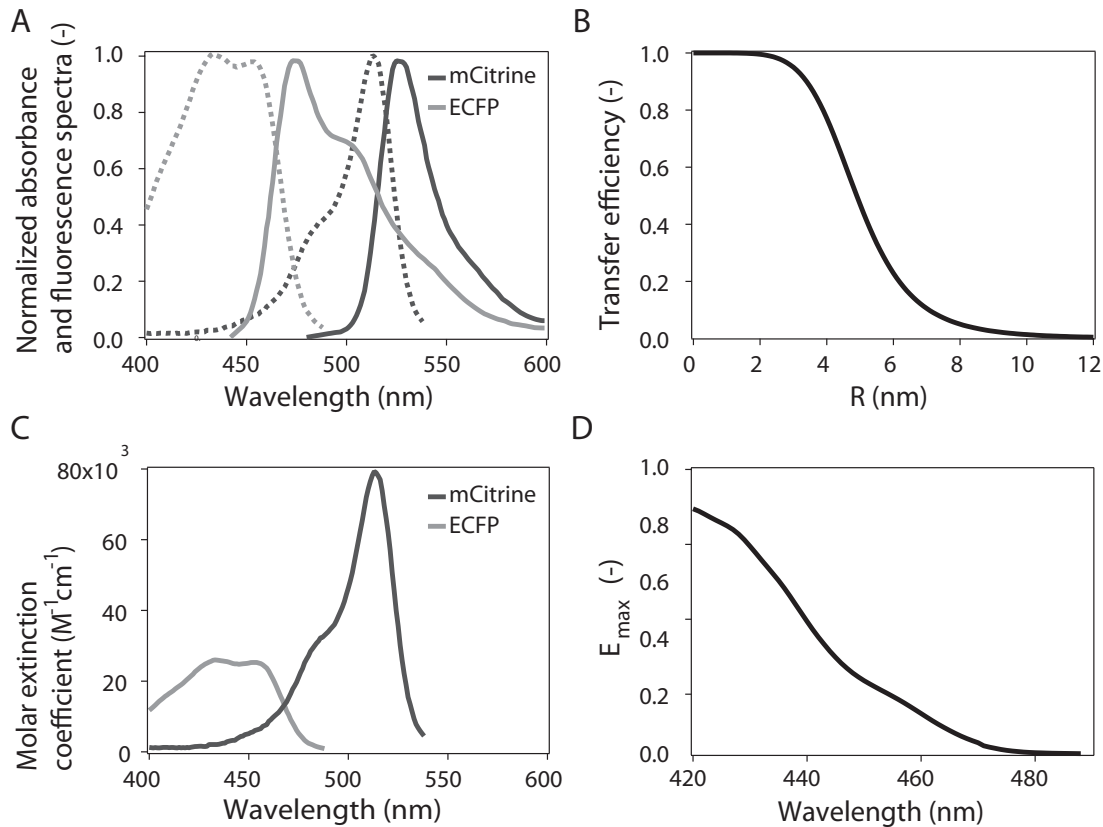
Figure 5.4: Spectral properties of a typical FRET pair, ECFP and Citrine. A. Absorption (dashed lines) and emission (continuous lines) of ECFP and mCitrine. These chromophore forms a useful FRET pair for measurement in living cells as ECFP emission and mCitrine absorption spectra are overlapping. The theoretical (R_0) Förster radius is 4.9 nm. **B.** Efficiency vs intermolecular distance, R. The FRET efficiency decreases quickly between 3 and 9 nm for this fluorophore pair. **C.** Molar extinction coefficient of the two molecules vs wavelength. **D.** Maximum FRET efficiency measurable at different wavelength due to the ratio between ϵ_{ECFP} and ϵ_{mCit}. This maximum efficiency is directly related to the dynamic range of the measured FRET ratio (FR).

The major difficulties arise from the measurement system itself, i.e. sample and instrument. In an hypothetic ideal system, with totally separated excitation and detection channels, and known chromophore local concentrations, FRET determination is trivial. In real experiments, emission and excitation spectra of typical chromophores are overlapping (e.g. mCFP and mCitrine fig. 5.4A). This problem has been resolved with the corrections of the bleed-through.

The use of genetically encoded fluorescent proteins for energy transfer experiments is complicated not only by the high overlap of the spectra, but also by the low stability, quantum yields, and absorption coefficients compared to modern organic dyes. This leads to a lower range of measurable distance between fluorophores (fig. 5.4B). It also decreases the reachable maximum FR value (see eq. 5.13), decreasing the sensitivity of measurements, i.e the maximal E available (fig. 5.4D).

In spite of very important drawbacks, FRET measurements in living cells is a highly valuable tools to study molecular interactions. Furthermore, the existence of many genetically encoded fluorophores pairs allows a wide variety of combinations. This variety has enabled dual FRET measurements in cells [149].

5.4.2   FRET software

The FRET analysis software described above has been designed to simplify and generalize the treatment of data obtained by microscopy on living cells. The software contains three independent parts; a file importer, a module for bleed-through correction and an automated FRET calculation routine. These three parts can be performed alone without interfering with other processes.

The image acquisition module allows one to work on different measurement setup without conversion problem. The reordering module enhances software versatility and lower analysis time.

The bleed-through correction is one of the major issue in FRET analysis. This feature has been extensively discussed and softwares have been developed to deal with the non linearity of the correction factor with the intensity of the fluorophores (e.g. [150]). This feature is not yet available in this software. However, such dramatic deviation from linearity has not been observed with the DA pairs studied until now (ECFP-EYFP, mCFP-Citrine, mGFP-mCherry, Cy3-Cy5, Atto555-Cy5) using the thresholding module of the software. If needed a procedure for the correction could be easily implemented in the existing software.

The signal ROI determination is easy to perform. The ROI can be determined at any step of the calculation. Two methods of background removal have been implemented. The first method is a standard method based on the manual determination of background region. This technique was not appropriate for the simultaneous analysis of several micrographs obtained with different conditions. A second method was developed where the background is automatically extracted using value rejected after thresholding. The only limitation of this methods is the need of region without fluorescence signal. This condition is fulfilled in the majority of microscopy experiments on adherent cells.

The image filtering has two main functions. First, it corrects the small defaults in alignment of the microscope channels used in the experiments, a feature that is never-

theless not sufficient for large shift between channels. The second effect is the removal of many of the uncertainties arising from the measurement system. The measurement noise is lowered by gaussian and median filtering. Furthermore, median filtering decrease dramatically the artifacts coming from fluorescent spikes and other defect in the detection. These filtering steps improve the calculated FRET values from images. However, filtering could also introduce slight artifacts in the final results.

FRET calculation by this software on movies, or with multiple conditions treated in the same analysis step, dramatically decreased the analysis time compare to single-image treatment softwares. Furthermore, this batch analysis insures an equal treatment for the different conditions of time frame and dramatically reduces operator bias.

5.5   Conclusion

This chapter described the functioning and possibility of a small FRET microscopy analysis software. It has been successfully used for different FRET microscopy experiments (unpublished yet). The results were reproducible and available in different output formats.

Organization of nAChR in membrane domains

6.1 Abstract

Nicotinic acetylcholine receptors (nAChR) in muscle fibers are densely packed in the post-synaptic region at the neuromuscular junction (NMJ). Rapsyn plays a central role in directing and clustering nAChR during cellular differentiation and NMJ formation, however, it has not been demonstrated whether rapsyn is the only cause of receptor immobilization. Here, we used single-molecule tracking methods to investigate nAChR mobility in plasma membrane of myoblasts cells during their differentiation to myotubes in the presence and in absence of rapsyn.

In C2C12 myoblasts, nAChR were mainly immobile, with only few freely mobile receptors. However, about 20% of the nAChR were diffusing confined in small domains with a median size of 46 nm. The proportion of confined receptors varied slightly during cell differentiation. In R11 myoblasts, devoid of rapsyn, the fraction of mobile nAChR was increased strongly with a concomitant 3-fold decrease of the immobile population of nAChR with respect to C2C12 cells. However, half of the mobile receptors were confined to domains with a median size of 117 nm.

Measurements performed in heterologously transfected HEK293 cells confirmed the direct immobilization of nAChR by rapsyn. However, irrespective of the presence of rapsyn, about a third of nAChR were confined in 300 nm-sized domains.

Our results show that rapsyn immobilizes nAChR efficiently independently of other post-synaptic scaffold components, and that nAChR is constrained by confinement independently of rapsyn in cell that do not express other scaffolding proteins, whoever that in the presence of rapsyn the size of these domains is strongly reduced.

6.2   Introduction

Neuromuscular junctions (NMJ) are long-lasting synapses mediating signal transmission between neurons and skeletal muscle cells [37]. The postsynaptic membrane of NMJ comprises a high density (ca. 10,000 copies/μm^2) of nicotinic acetylcholine receptors (nAChR) bound non-covalently to a specific scaffolding protein network through a 1:1 interaction with rapsyn [73, 80, 151, 152]. The high density and the precise location of nAChR in the muscle fibre directly beneath a nerve terminal are essential for fast and robust signal transmission.

The presence of nAChR at the NMJ during development depends on agrin, a heparan sulphate proteoglycan secreted by the pre-synaptic motor neuron [153] and rapsyn [154]. Agrin activates the muscle-specific tyrosine kinase MuSK through binding to its co-receptor LPR4 [43, 42], which leads to phosphorylation of the β-subunit of nAChR [73], and in turn to local receptor clustering at the nerve terminus [155]. Rapsyn binding to MuSK is required for this phosphorylation steps [156, 44]. Recently, Wnt signaling has been found to play a role in nAChR cluster formation during muscle development [48]. Agrin and Wnt seem to regulate the distribution of nAChR in the postsynaptic membrane in an antagonistic manner by increasing receptor density in the NMJ and decreasing receptor density outside the NMJ [49]. During these processes rapsynÕs major role appears to be to bring nAChR into contact with other NMJ proteins without altering channel function [157].

Rapsyn is also found at high concentrations in membranes of the electric organ of Torpedo [158] and in the developing neuromuscular synapse of *Xenopus*[154].

The myristoylated N-terminus of rapsyn targets the protein to the plasma membrane where it participates in a number of important additional molecular interactions [159]: (i) Rapsyn self-associates through its seven tetratrichopeptide repeats [68, 69]. (ii) It binds to the cytoskeleton via an ACF7-containing network [75]. (iii) It also binds to other molecules of the NMJ, such as calpain [77], β-catenin [160], and α-actinin [76].

Failure of nAChR anchoring at the NMJ endplate causes defects on the neuromuscular synaptic transmission leading to severe myopathies [161]. Understanding the mechanism of nAChR anchoring is therefore of importance for finding ways to treat muscular diseases.

Here, we use single molecule microscopy to investigate the mobility of individual nAChR in muscle cells. Our results show that rapsyn immobilizes nAChR efficiently, independently of other post-synaptic scaffold components and that nAChR is immobilized independently of rapsyn in cells that do not express the scaffolding protein.

6.3 Materials and methods

6.3.1 Cell culture and transfection

Myogenic cell lines C2C12 (myoblast) and R11 (rapsyn$^{-/-}$ myoblast) were grown and differentiated to myotubes. C2C12 obtained from U. Rüegg (University of Geneva) were grown in DMEM/F12 (Invitrogen) supplemented with 10% fetal bovin serum (FBS), 100 units/ml penicillin and 100 μg/ml streptomycin. R11 myoblasts obtained from C. Fuhrer [157], were grown in DMEM (Invitrogen) supplemented with 10% FBS (Sigma), 100 units/ml penicillin, 100 μg/ml streptomycin and 4 U/ml γ-interferon (Sigma). Cells were maintained at 34 °C in humidified 5% CO2 atmosphere. For imaging experiment, cells were seeded on 0.17 mm thick glass coverslips. Differentiation to myotubes was induced at 80 % confluency by switching medium to DMEM supplemented with 5% horse serum (Sigma), and growth at 37 °C in a humidified 5% CO2 atmosphere.

HEK 293T cells (ATCC) were grown in DMEM/F12 supplemented with 10% FBS, at 37 °C in humidified 5% CO2 atmosphere. Cell were plated, on 25 mm glass coverslip posed in a 30 mm well, transfected 24 hours later using Effectene (Qiagen) with cDNA of nAChR subunits (60 ng α-subunit, 30 ng β-subunit, 30 ng γ-subunit, 30 ng δ-subunit) and 30 ng of either EGFP (Clontech) or Rapsyn-GFP (Generous gift from J. Cohen) [69]. Single-molecule fluorescence experiments were performed 24 to 48h after transfection in colorless DMEM or HBSS (both Gibco) without antibiotics and serum.

6.3.2 Receptor labeling

nAChR in living cells were visualized using toxins labeled by either α-conotoxin-GI (α-CnTx) conjugated by organic fluorophores or semiconductor nanoparticles (NP) coupled to α-bungarotoxin (α-BgTx). Labeling of nAChR with α-CnTx conjugated with either Cy5 (α-CnTx-Cy5) or Atto647N (α-CnTx-Atto647N) as performed using the repetitive, reversible method described in detail elsewhere [105]. Briefly, cells were perfused, using a VC-77SP fast step perfusion system (Warner Instruments Corp), for 10 seconds with 30 nM fluorescent α-CnTx labeling about 1-5% of the nAChR expressed on the cell surface, followed by 20 seconds with HBSS after which fluorescence image series were acquired. This sequence was repeated at wish, enabling to measure diffusion of large number of individual receptors on single cells, despite fast bleaching of the organic dyes. Alternatively, streptavidin-coated fluorescent semiconductor NP's were incubated with α-BgTx-biotin (Sigma) at a ratio of 0.5 toxin molecule per NP. Myoblasts were labeled with 500 pM α-BgTx-NP conjugates in DMEM for 60 min at 37 °C. Prior microscopy measurements, the cells were rinsed 3 times in colorless DMEM to remove unbound probes.

6.3.3   Single-molecule microscopy

Cells glass coverslips were mounted on a modified epiluminescence wide-field microscope (Axiovert 200, Zeiss). The fluorescently labeled α-CnTxs were excited with circularly polarized light of the 632.8 nm line of a HeNe laser (Coherent) that was directed by a dichroic mirror (Q645LP, Chroma Corp) into a microscope objective (C-Apochromat 63x W Corr, 1.2 NA, Zeiss) to illuminate a 22 μm diameter region of the sample. Fluorescence emission was collected by the same objective, passed through a filter (HQ710/100, Chroma) and imaged on an intensified CCD camera (Ixon 887BV, Andor). To minimize photobleaching of organic dyes, cells were illuminated for 50 ms with excitation intensities around 0.5 kW/cm^2 only during image acquisition using a shutter (LS3T2, Vincent Associates). Single-molecule images were recorded at a frequency of 4-20 Hz. Dissociation of α-CnTx from nAChR was much slower than photobleaching as described in detail elsewhere [105].

α-BgTx-NP conjugates were excited at 488 nm (Ar+ laser, Innova Sabre). A circularly polarized laser beam was directed into the objective by a Q495LP dichroic mirror (Chroma Corp.) into the objective. Fluorescence emission was collected by the same objective and imaged after passing through a HQ595/50 filter (Chroma) dichroic. Single-molecules images were recorded at a frequency of 20 Hz, illuminating the cells for 48.3 ms with excitation intensities around 0.1 kW/cm^2.

Single-molecule trajectories have been measured at the apical membrane of the cells to avoid unwanted effects of the cell adhesion and fluorophore accumulation on the glass surface.

6.3.4   Data evaluation

Image sequences were treated using a home-written Igor Pro (Wavemetrics) procedure. Each image was first filtered to remove long-range structures such as laser intensity profile and auto-fluorescence of the cells. Next, local fluorescence intensity maxima were identified on the filtered image. Fluorescence peaks associated to these maxima were then fitted with a 2D-Gaussian on the original unfiltered image. Fitted fluorescent peaks, evaluated for intensity, size and shape to select only potential single-molecules, were then tracked over series of images to evaluate single molecule trajectories. Characteristic one-step photobleaching or blinking events were taken as criterion of acceptance for every single-molecule trace. Finally, square displacements (r^2) were evaluated for every time interval of a single trajectory.

Single-molecule traces were treated using two different strategies. Datasets of short traces resulting from experiments with organic dyes were evaluated according to Schütz et al. [86]. Briefly, the normalized cumulative probability density function P(r^2,t) of r^2 was evaluated for each time lag t$_{lag}$. This P(r^2,t) was then fitted using equations 4.15

or 4.16, yielding one or two average square displacement (r_0^2), respectively. In eq. 4.16, α yielded the fraction of the two populations. D for each population is then deduced using a standard MSD vs t_{lag} fit, according to eq. 4.10 & 4.11.

Whenever possible, in longer trajectories, the apparent confinement length L_c and initial diffusion coefficient D_0 were also evaluated. D_0 was determined from a linear fit of the points 2, 3 and 4 of the plot of the mean square displacement (MSD) versus the t_{lag} (eq. 4.10). This value was used to separate mobile and immobile receptors by setting a noise-dependent threshold. MSD plots of individual receptors were fitted using an approximation of a single molecule in a square yielding an apparent diffusion coefficient D_0 and confinement length L_c corresponding to the length of the diagonal of a rectangle enclosing the diffusing object [86, 91, 162] (eq. 4.11). The noise term added in each equation is composed of the lack of precision of the an the position and the movement of the particle during the acquisition time.

As the diffusion of a particle is a self-similar process, long single-molecule trajectories can be treated using the moment scaling spectrum (MSS). This method gives more accurate information about the motion type and, as it involves only linear fit, avoids error coming from complex multivariated fit ([131, 163]. The MSS-slope is a single parameter describing anomalous, directed and confined diffusion: A slope of 0.5 defines Brownian motion; values below 0.5 are characteristic of confined motion, value equal to zero indicating immobility; results above 0.5 describe superdiffusion (e.g. directed diffusion). This method is used to analyze segments of single traces to map changes in diffusion mode [131]. Each of MMS-slope has been computed using a sliding window of 60 frames.

6.4 Results

6.4.1 Mobility of nAChR in C2C12 mouse muscle cells

C2C12 muscle cells differentiate into functional myotubes within 5 days after addition of 5% horse serum to the cell culture medium. Diffusion of nAChR in the cell plasma membrane was measured by single-receptor tracking before and 2, 3, 5, 8 and 11 days after induction of differentiation. During this time period, significant changes were observed in the membrane distribution of nAChR, visualized using fluorescent toxins (fig. 6.1). Before differentiation nAChR was homogenously distributed in the membrane (fig. 6.1A). The same homogenous distribution was observed after two days (fig. 6.1B). Mononucleated cells began to align after 3 days and dense receptor clusters became visible at the cell membrane even in the absence of presynaptically secreted agrin (fig. 6.1C). After 5 days, when most of the cells were fused to multinucleated cells and began to form myotubes, dense clusters of nAChR appeared (fig. 6.1D).
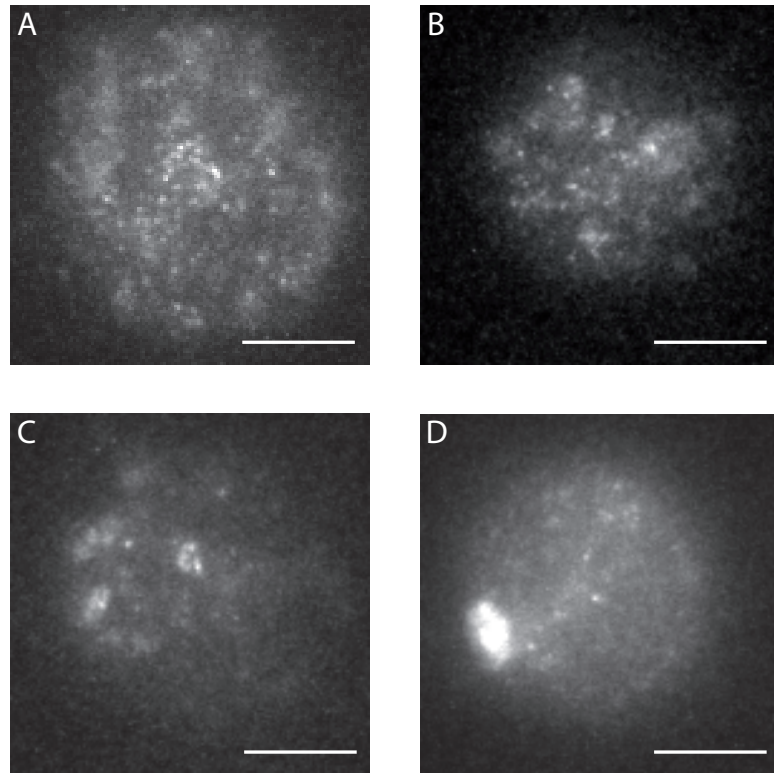
Figure 6.1: Fluorescence micrographs of nAChR in the apical membrane of C2C12 myotubes under differentiation. nAChR were labeled with α-CnTx-Cy5. IImages were taken by a wide-field microscope after 5 frames corresponding to a total illumination time of 250 ms. The illuminated area is limited to a single cell. **A.** Myoblast cells before differentiation nAChR are homogenously distributed. **B.** Two days after culture medium exchange, receptor distribution is still homogenous.. **C.** Three days after culture medium exchange, denser and larger regions are visible. **D.** Multinucleated cell eight days after culture medium exchange, dense clusters of receptors are visible. Bars: 10 μm.

Three different populations of nAChR were observed on muscle cells: Immobile, confined and freely diffusing receptors. Figure 6.2 depicts representative plots of the mean square displacement (MSD) versus time lag (t_{lag}) of single receptor trajectories. For Brownian diffusion, the MSD is linearly dependent on time; deviations from linearity indicate non-ideal diffusion [129]. Here, we characterized trajectories of individual nAChR according to two parameters, (i) the receptor's initial diffusion coefficient D_0, and (ii) the length L_c of its confinement region. The value of D_0 was used to distinguish between mobile and immobile receptors, and that of L_c to discriminate confined ($L_c < 280$ nm) from freely diffusing receptors.

Individual nAChR were visualized after binding of α-conotoxin covalently labeled
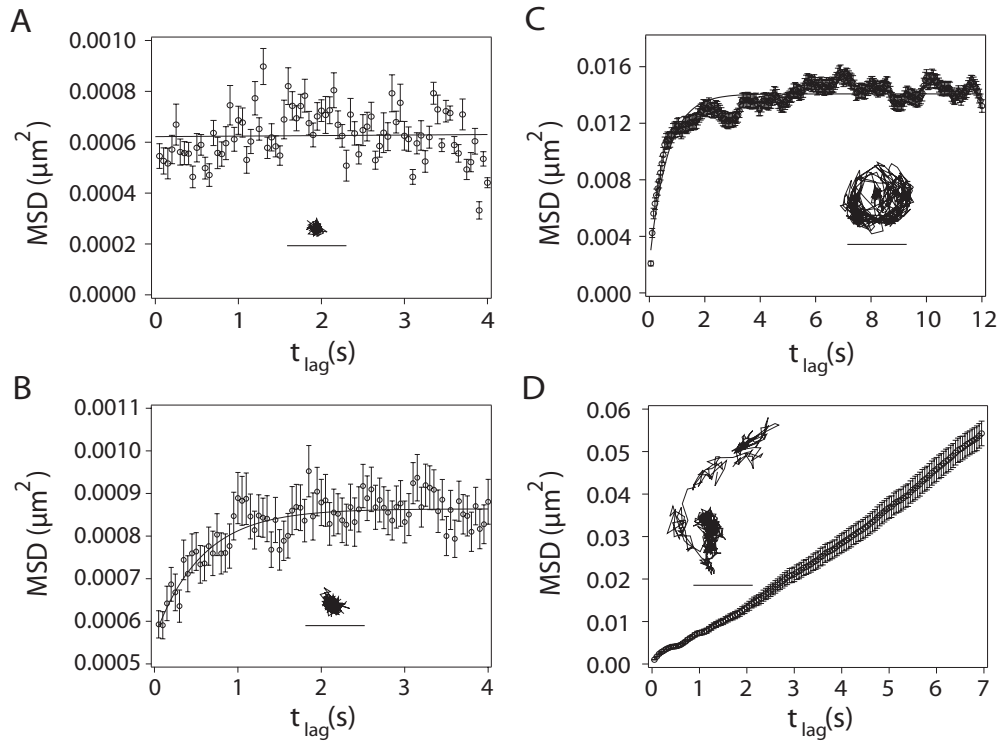
Figure 6.2: Typical MSD vs tlag plots. The three characteristic modes of motion observed for nAChR labeled with α-BgTx-QD in C2C12 muscle cells. Each particular trajectory evaluated is depicted in the corresponding MSD plots (scale bars: 100 nm). **A.** An immobile receptor; the positive y-intercept is due to experimental noise. In this case, the accuracy of measurement is 12 ± 2 nm, which is typical for quantum dots on living cells in our experimental setup. **B.** A receptor confined in a small domain of characteristic length $L_c = 30 \pm 1$ nm and a diffusion coefficient of $D = 1.3 \pm 0.2 \cdot 10^{-4}$ $\mu m^2/s$. **C.** Receptor confined in a domain of characteristic length $L_c = 189 \pm 1$ nm and a diffusion coefficient of $D = 4.6 \pm 0.2 \cdot 10-3$ $\mu m^2/s$. **D.** Mobile receptor. The receptor moving with a diffusion coefficient $D = 1.48 \pm 0.03 \cdot 10^{-3}$ $\mu m^2/s$. The receptor exhibits a small positive deviation from the linearity due to sample movement and deviation from pure Brownian diffusion of the receptor. The speed of this supplementary motion is 15 nm/s.

with the fluorescent probe Cy5 (α-CnTx-Cy5), yielding single-receptor trajectories of up to 40 frames acquired at 4 Hz. Single receptor trajectories have been measured using cells at three different states of development: before induction (undifferentiated myoblasts), during differentiation (days 2, 3 and 5) and after differentiation (multinucleated myotubes, days 8 and 11) (fig. 6.3). Before differentiation, only 2% of the receptors showed free brownian diffusion, 24% diffused in confined regions and 74% were immobile. During differentiation and cell fusion, the immobile receptor fraction increased slightly without a significant effect on the two other types of receptor mobility. However, in differentiated multinucleated cells, the proportion of immobile receptors decreased strongly, with a concomitant increase of the fraction of confined diffusing receptors from 20 to 34% and of freely diffusing receptors up to 10%. At all time points, the majority ($> 60\%$) of the confined receptors were present in regions with L $_c$ < 100 nm.
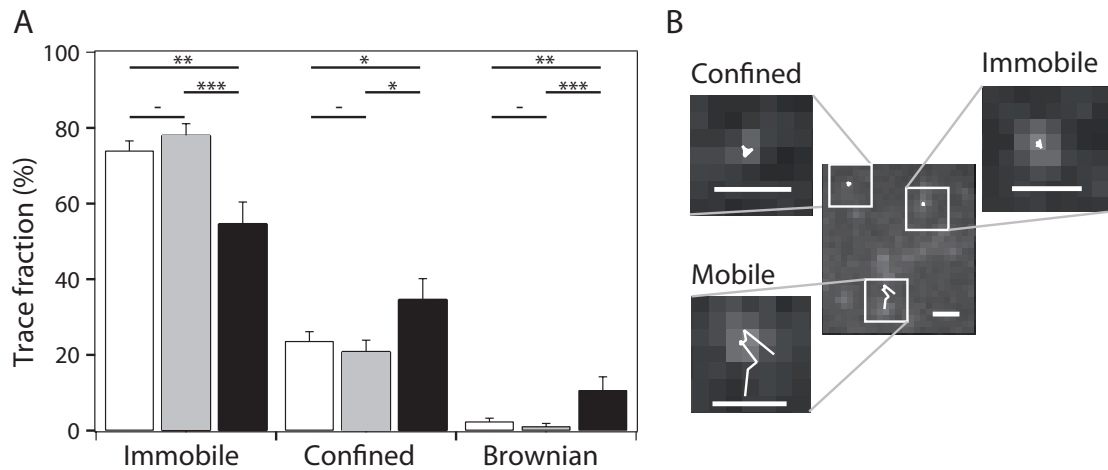
Figure 6.3: Evolution of the fraction of immobile, confined and freely diffusing receptors in differentiating C2C12 muscle cells. A. nAChR was labeled with α-CnTx-Cy5 and images were acquired at 4 Hz. White columns correspond to measurements on C2C12 myoblasts before induction of differentiation (n=292). Gray columns show receptor mobility during differentiation (days 2, 3, and 5) (n=182). Black columns describe receptors in multinucleated muscle fibers (days 8 and 12) (n=75). T-test: * p < 0.05; ** p < 0.01; *** p < 0.001 **B**. Trajectories corresponding to the three characteristic modes of motion. Scale bars: 1μm.

6.4.2 Diffusion of nAChR in muscle cells devoid of rapsyn

In order to measure the direct effect of rapsyn on receptor mobility, trajectories of individual nAChR have been measured on R11 rapsyn$^{-/-}$ mouse muscle cells that are

devoid of rapsyn (both alleles are inactive). Because R11 muscle cells are difficult to differentiate into multinucleated myotubes, comparative experiments have been carried on myoblasts.

In order to investigate the direct effect of rapsyn on receptor mobility, trajectories of individual nAChR have been measured on R11 rapsyn$^{-/-}$ mouse muscle cells that are devoid of rapsyn (both alleles inactivated). Because R11 muscle cells are difficult to differentiate into multinucleated myotubes, comparative experiments have been carried on myoblasts. Single receptor trajectories of enhanced quality were obtained using toxins labeled with fluorescent probes of increased photostability, i.e. quantum dots on α-Bungarotoxin (α-BgTx-QD) and Atto647N on α-Conotoxin GI (α-CnTx-Atto647N), yielding extremely long trajectories of up to 6,000 frames at 20 Hz, i.e. 5 minutes. For most experiments, however, we measured only up to 300 frames to reduce phototoxicity; the average length of the traces for C2C12 and R11 cells was 254 and 159, respectively, due to trace interruption by blinking and bleaching. The yet substantially improved quality of the MSD vs tlag plots allowed us to determine particular D_0 and L_c values with considerably increased accuracy. Moreover, the long traces allowed the use of the moment scaling spectrum (MSS) data evaluation method ([131]) to unequivocally classify the type of mobility for single trajectories (see Material and Methods). Figure 6.4 shows the resulting graph of the MSS-slope versus D_0. There is a shift from immobile and confined receptors in presence of rapsyn (0 < MSS-slope < 0.4) to confined and freely mobile receptors in absence of rapsyn (0.1 < MSS-slop e< 0.8). The median size of the observed confinement regions increased from 46 nm for C2C12 to 117 nm for R11 cells. Moreover, in the absence of rapsyn the mobility of nAChR strongly increased as determined by D_0.

In spite of the considerably long duration of the trajectories, up to 100 s, not a single case has been observed where an initially immobile or confined molecule switched to Brownian diffusion. However, some of the apparently freely diffusing receptors exhibit transient clustering. Figure 6.5 shows one of the initially freely diffusing receptor being transiently trapped in domains, featuring transitions between free and confined motion, and immobility.

6.4.3 Heterologous expression of nAChR and rapsyn

In muscle cells many different proteins participate in scaffolding the nAChR within the NMJ. To investigate the interaction between nAChR and rapsyn in the cellular plasma membrane in the absence of other components of the NMJ, we expressed the proteins heterologously in HEK 293T cells. The mobility of nAChR was investigated under two different conditions: Cells have been transfected with cDNA of nAChR subunits
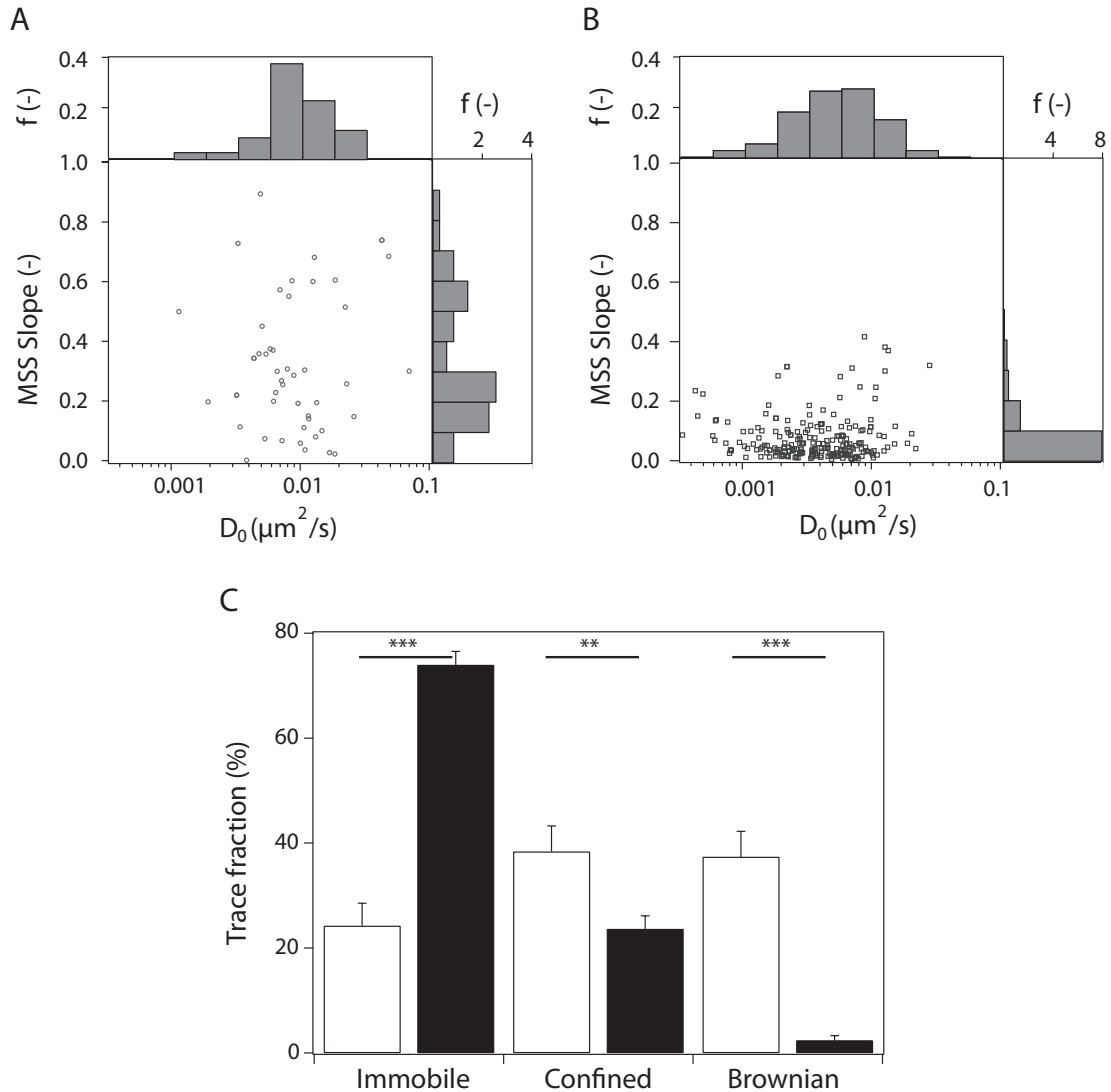
Figure 6.4: Mobility of nAChR in muscle cells evaluated by MSS data treatment. MSS slope versus D_0 for rapsyn$^{+/+}$ (C2C12) cells, **A**, and rapsyn$^{-/-}$ (R11) cells, **B**. Each of the point has been computated from a receptor trajectory longer than 100 frames. For Brownian diffusion, the Hurst parameter is equal to 0.5. Results under 0.5 denote a confined receptor, 0 meaning immobile molecule. Values above 0.5 show super diffusion, 1 meaning totally directed motion. **C.** Fractions of receptors in the three different categories in R11 (white bars) and C2C12 (black bars) myoblasts. *** p < 0.001 and ** p < 0.01.
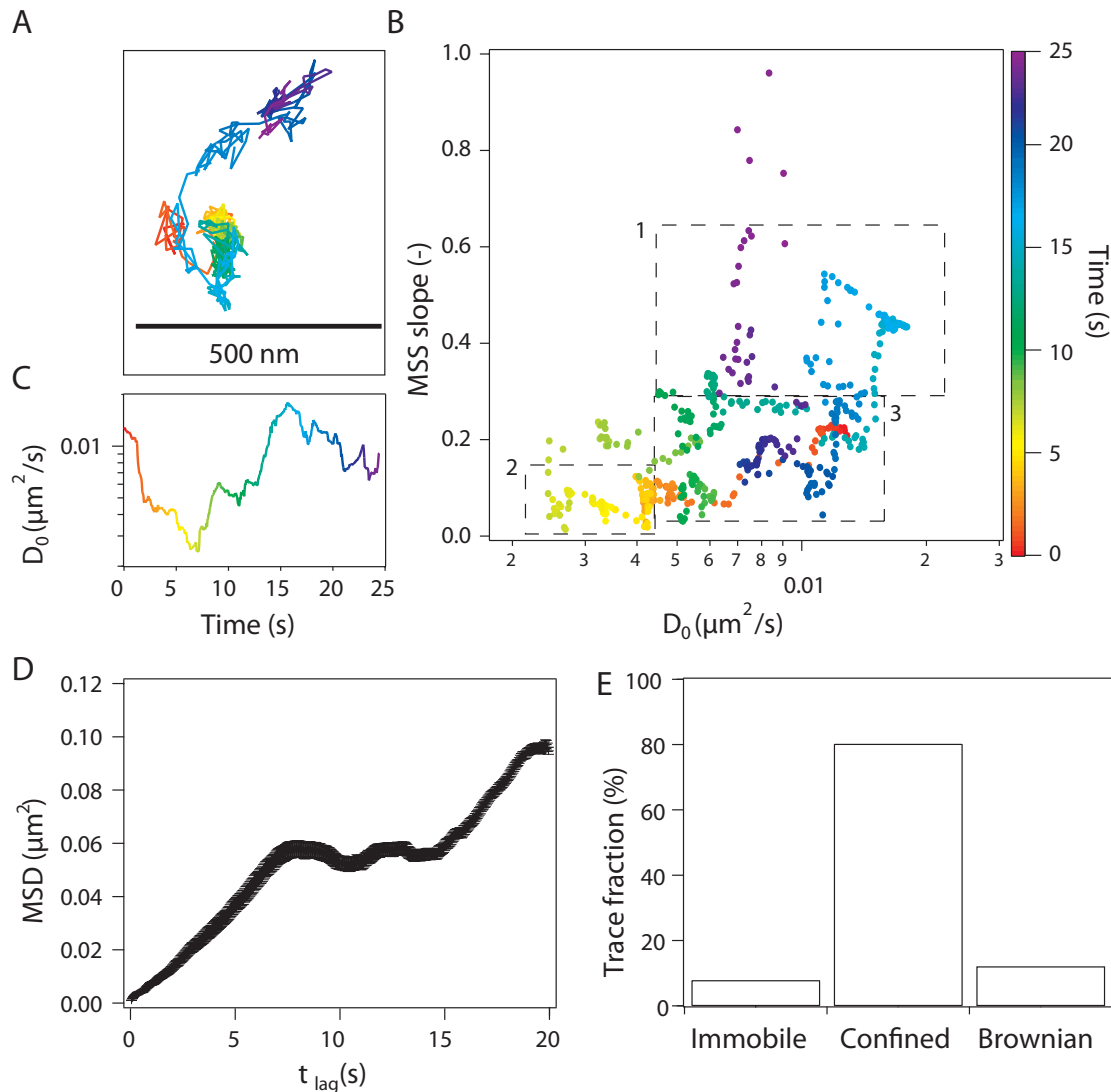
Figure 6.5: Different representations and evaluations of the mobility of a single nAChR in the cell membrane. This trajectory is one of the only two nAChR exhibiting changes in diffusion modes during the measurement. Receptors, in R11 rapsyn$^{-/-}$ muscle cells labeled with α-BgTx-QD and imaged at 20 Hz show transient recruitment in membrane domains. **A**. Trajectory of a single receptor. The color code indicates the time scale. **B**. MSS-slope vs D$_0$, indicating different modes of diffusion of a single receptor. Region 1 corresponds to freely diffusing receptor in the plasma membrane. Region 2 to confined diffusion. Region 3 corresponds to immobilized receptor. At t = 0, the receptor is diffusing in a confined domain. Between t = 2 s to t = 10 s it is immobile. Then it is alternating between confined and free Brownian motion. **C**. Initial diffusion coefficient of each segment of the trajectory. This representation also shows transient trapping between 5 and 8 s. Color code as in B. **D**. MSD vs tlag of this particular trajectory. The multiple diffusion modes of the particle are not visible in this representation. E. Histogram representing the 3 modes of mobility. The distribution is in good agreement with the values obtained by the MSS data evaluation of figure 6.5B.

together with either rapsyn-GFP or, as a control, cytosolic EGFP. As for experiments in
C2C12 muscle cells (fig. 6.2), receptor mobility has been classified into three categories,
according to the same criteria.

Upon expression of only nAChR in HEK 293T cells no immobile receptors have been
observed (fig. 6.6). Mobile receptors can be distinguished as those featuring Brownian
or confined diffusion according to a cumulative distribution analysis ([86, 162]). Freely
diffusing ($55 \pm 2\%$) nAChR had a $D_0 = 0.043 \pm 0.002$ $\mu m^2/s$, those showing confined
diffusion were characterized by an initial $D_0 = 0.016 \pm 0.005$ $\mu m^2/s$ and a domain size
of $L_c = 320 \pm 20$ nm.

Co-transfection of rapsyn-GFP and nAChR plasmids in a 1:1 molar ratio in HEK
cells led to the formation of dense rapsyn clusters at the cell membrane (fig. 6.7B).
Very strikingly, we observed a large population of immobile receptors (19%), with D_0
< 0.005 $\mu m^2/s$; a decreased population of the freely diffusing receptors (53%); virtually
unchanged fraction of receptors with confined diffusion (28%) with slightly increased L_c
from 322 ± 21 to 377 ± 33 nm (p < 0.001) as compared to the absence of GFP-rapsyn.
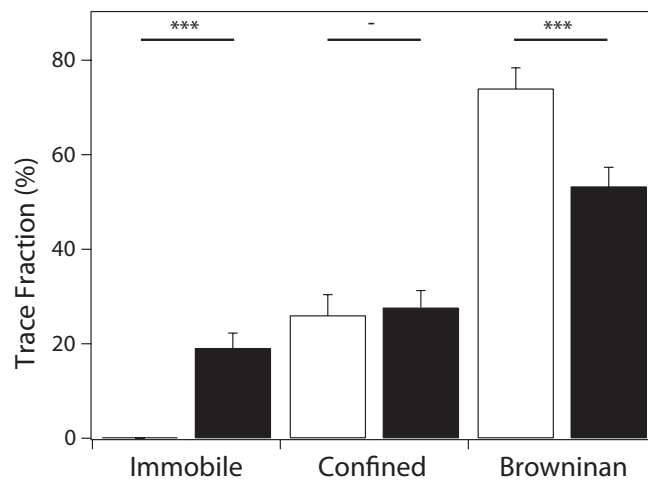
Figure 6.6: Diffusion of nAChR in HEK 293T cells. Fraction immobile, con-
fined and freely diffusing nAChR in HEK 293T cells. White columns refer to cells co-
transfected with nAChR and EGFP (n=108). Black columns refer to cells co-transfected
with nACHR and rapsyn-GFP (n=163). *** p < 0.001.

The low proportion of labeled nAChR used for each image series did neither allow
to detect clusters of receptors nor to identify regions on the cell membrane of restricted
nAChR diffusion.

6.5 Discussion

6.5.1 Visualizing nAChR with fluorescently labeled toxins

At high concentration (30 nM) of fluorescent α-CnTx, nAChR could be stained on the surface of myotube both inside receptors clusters, i.e. in regions of high receptor density and in membrane areas featuring low surface density. The binding of α-CnTx could be reversed allowing sequential re-staining [105]. This yielded a large number of trajectories of single receptors sampling many different receptors on the same cell and thus resulted in a substantial improvement of the statistics. On the other hand, staining the nAChR with virtually irreversibly bound α-BgTx-NPs made it possible to acquire very long traces, revealing changes in diffusion modes.

6.5.2 Nicotinic receptor mobility during myotubes formation

C2C12 mouse myoblasts form postsynaptic-like structures after differentiation [40] and therefore serve as a suitable experimental system to study receptor mobility in model synapses. In undifferentiated C2C12 cells no nAChR clusters were resolved, despite the fact that approximately 70% of the receptors were immobile. Clusters of nAChR and rapsyn did appear only after two days of incubation in the differentiating culture medium, still before fusion of myoblasts to tubes. No significant changes of receptor mobility were detected until the cells became multinucleated and the fraction of mobile receptors increased. This might be explained by the observation that during differentiation rapsyn expression remained unchanged while expression of nAChR subunits increased, i.e. the rapsyn/nAChR ratio decreased [164]. On the other hand, an increasing rapsyn/nAChR ratio is known to slow down receptor turnover [165], which corroborates our finding that the nAChR mobility is lower in undifferentiated C2C12 cells than in differentiated cells. Our results suggest that individual nAChR are released from receptor-dense regions to move freely in the surrounding membrane bulk phase. Such a release could be important either for receptor recycling or for serving as buffer of receptors, outside the synapses.

In order to estimate the rate of change, in nAChR mobility, k_{change}, we divided the number of changes observed by the total duration of all single-molecule trajectories. The rather short single molecule trajectories obtained using aCnTx labeled with organic fluorophores did not feature any change of receptor mobility within any of the 292 traces evaluated. This implies that for the duration of a few seconds per trace, the molecular interactions that keep the individual receptor molecules in a particular state did not change ($k_{change} < 2 \cdot 10^{-3}$ s^{-1}). This result on short trajectories was confirmed on long trajectories, of which a large majority did not show any changes. They were obtained with the photostable aBgTx-NP and typically span tens of seconds. Only two single receptors ($< 1\%$ of the total number of trajectories) exhibited changes in diffusion types

yielding a $k_{change} < 3 \cdot 10^{-4} s^{-1}$. This low switching rate could contribute to the stability of the NMJ.

Upon heterologous expression of nAChR in HEK cells devoid of the scaffolding protein rapsyn only a low number of receptors ($< 1\%$) were immobile, whereas, heterologous expression of rapsyn in HEK cells resulted in the appearance of a large fraction of immobilized nAChRs (fig. 6.6). These results confirmed that rapsyn alone immobilize nAChR at the single molecule level. Rapsyn also induced a small but significant increase of L_c.

Muscle cells presented a very different picture featuring a very large immobile fraction. Throughout differentiation, a substantial fraction of receptor diffused in confined regions (fig. 6.3A). Thus, confinement of nAChR is not directly related to an increased expression of muscle specific proteins associated with myotubes formation and could be due to direct interactions of the receptor with the plasma membrane [58]

Immobile or strongly confined receptors were also found outside of nAChR clusters in C2C12 muscle cells. This observation suggests that not all complexes between rapsyn and nAChR are recruited in clusters in neuronal myotubes.

6.5.3 Formation of nAChR clusters

Rapsyn forms dense domains at the cell membrane of both myoblast and HEK cells (fig. 6.7). However, nAChR does not form clusters. There are two possible explanations for this observation: (i) The number of receptors is too low compared to rapsyn diluting them over the entire rapsyn-covered membrane domains; (ii) Differentiation triggers receptor clustering. The absence of nAChR clustering in HEK can be explained by its low expression upon transient transfection (< 1000 copies/cell) [105].

6.5.4 Recruitments of nAChR in membrane domains

Receptors diffusing in confined domains have been observed in both rapsyn$^{+/+}$ and rapsyn$^{-/-}$ myoblasts indicating rapsyn-independent recruitment of nAChR in muscle cells, however, L_c is smaller if rapsyn present. Membrane domains of nAChR of small dimension have been observed using STED microscopy in chemically fixed CHO cells expressing nAChR [166]. Moreover, in presence of rapsyn, the fraction of confined receptor remained constant while the immobile fraction increased drastically in the expense of mobile which become almost absent (fig. 6.4).

The existence of very stable receptor-rich domains in the membrane might be due to endocytocytotic pathway; nAChR are known to colocalize with caveolin-3, a major functional component of caveolea, which is involved in agrin induced clustering of nAChR [57, 167, 168]. The values for the length of confinement, L_c, found here are comparable with the dimensions of 25-100 nm reported for caveolae [57]. The small number of
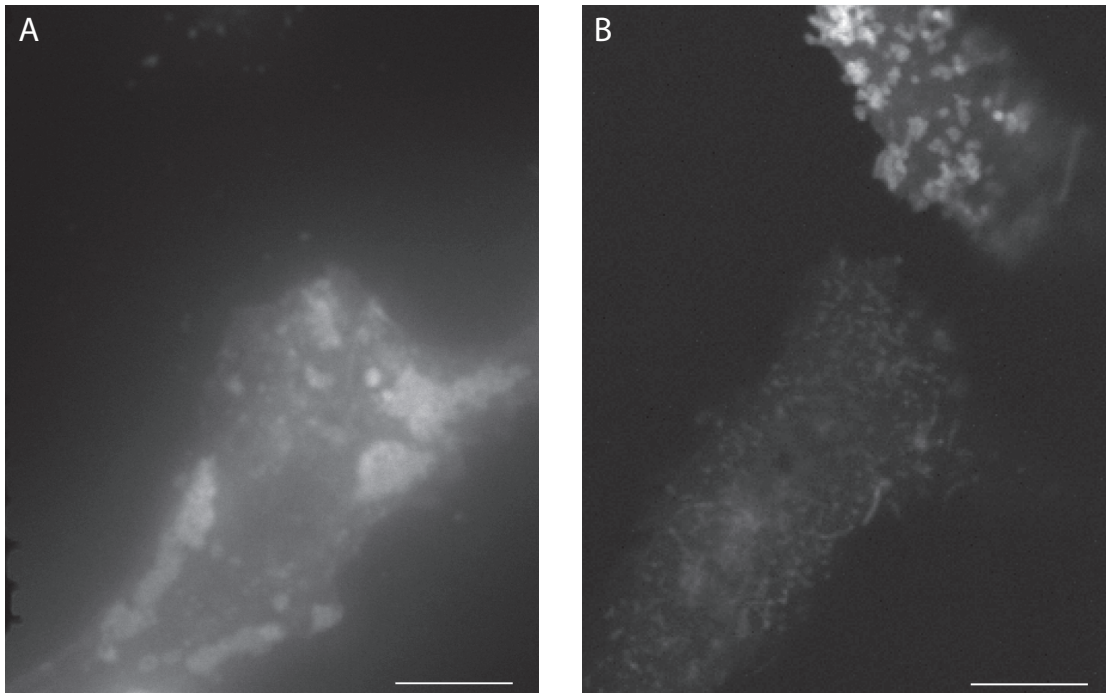
Figure 6.7: Distribution of fluorescent rapsyn in myoblast and HEK cells.A.
Wide-field laser excitation of C2C12 myoblast reveals large bright regions (> 1 μm) corresponding to high density of rapsyn-GFP. **B**. Confocal fluorescence micrograph of HEK
cells transiently expressing rapsyn-GFP, acquired with an LSM510 confocal microscope
(Zeiss). The size of the bright domains is much smaller in the heterologous expression
system than in the C2C12 myoblasts of figure 6.7A. White bars are 10 μm long.

immobile receptors observed in R11 cells suggests the existence of a less efficient, rapsyn-
independent mechanism of receptor immobilization. The long immobilization time of
≥ 15 seconds, (≥ 300 frames) observed in our present study, is not fully comparable
with transient receptor recruitment occurring in 50 nm sized membrane lipid domains
within the range of 0.5 s as observed by Suzuki et al. [169]. Specific and longer lasting
interactions with cytoskeleton components could explain our findings. However, the
existence of a substantial fraction of nAChR diffusing in confined region in HEK cells
reinforces the hypothesis a lipids dependent mechanism.

6.5.5   Transient recruitment of nAChR

The very rare, transient recruitment events of nAchR, shown in figure 6.5, are char-
acteristic of either hindered diffusion in the cellular plasma membrane [12], transient
interactions [170], or recruitment in specific domains [171]. nAChR is claimed to parti-
tion into cholesterol-rich membrane domains after agrin activation [63]. The transient
immobilization events observed here might stem from transient unstable membrane do-

mains.

6.6   Chapter conclusion

Single-receptor tracking showed a complex mobility pattern of muscle-type nAchR in the plasma membrane of different cell types: The presence of rapsyn increases the number of immobilized receptors and change the size of the confinement both as naturally abundant in muscle cells and when heterologously expressed in HEK cells. In muscle cells devoid of rapsyn, a fraction of the nAChR remains immobilized and confined by an unknown mechanism. Single-receptor imaging also revealed the existence of small membrane regions comprising confined nAChR which are not related to large receptor clusters associated to rapsyn. The small confinement regions may serve as a complementary regulatory mean for receptor store and release.

<div style="text-align: right">Chapter 7</div>

Diffusion of pentameric ligand-gated ion channels (pLGIC)

7.1 Abstract

Diffusion and trafficking of pentameric ligand-gated ion channels (pLGIC) is very important for correct receptors localization at e.g. synapses. The mechanisms leading to receptor immobilization or non-ideal diffusion are not known.

In this study, we use a novel small, specific and bright affinity label (*tris*-NTA-8Pro-Atto647N) enabling long term observations with high spatial resolution. We followed the diffusion of a series of mutants of the serotonin type 3 receptor ($5HT_3R$) with progressive deletions in the intracellular loop, and ELIC, a prokaryotic ligand-gated ion channel analogue devoid of intracellular loop, in the plasma membrane of living cells.

Two regions of the intracellular loop of the $5HT_3R$, aa 343-350 and aa 413-422, have been found to modulate receptor immobilization and directed motion, respectively. The initial diffusion coefficient of all $5HT_3R$ loop-deletion mutants and of ELIC were comparable to that of the wildtype $5HT_3R$.

Unexpectedly, a large fraction of ELIC was found to perform directed diffusion, although it has no intracellular loop.

7.2 Introduction

The movements and organization of cellular plasma membrane proteins are not fully understood. Early models described membrane proteins as randomly distributed objects

freely diffusing in a two-dimension fluid lipid bilayer [2], while recently biological membranes are viewed as complex heterologous dynamic 2D mixture of lipids and proteins. Membranes are complex systems regulating exchanges of matter and information between cells and their environment [172]. Previous work on 5HT$_3$R has shown a complex diffusion pattern of the receptor in the plasma membrane [173].

7.2.1 Ligand-gated ion channels

5HT$_3$R is a member of the pentameric ligand-gated ion channel (pLGIC) receptor superfamily, more specifically of the mammalian cys-loop receptor familly comprising the nicotinic acetylcholine receptor, the GABA receptor or the glycine receptor. All these receptors contain a large intracellular loop [174]. This receptor subtype is characterized by a conserved sequence comprising disulphide bond between to cysteins residues separated by 13 amino acids [26]. The structure of the 5HT$_3$R seems to be closely related to the nicotinic acetylcholine receptor based on sequence homology, biological and biophysical data [175]. Five 5HT$_3$R subunits have been cloned (A-E), only type A and B have been found to be present in the central nervous system. The 5HT$_{3A}$R is the only subunit that can form a functional homopentamer, all the others are expressed as heteropentamers in combination with the A subunit [176, 177].

5HT$_3$Rs are ionotropic serotonin receptors, the other sixteen are G protein coupled receptors. They are widely distributed in many mammalian tissues, mainly in the central and peripheric nervous systems [178, 179].

Recently, the atomic structure of two potential prokaryotic members of the pLGIC superfamily have been solved by X-ray crystallography [20, 19, 21], giving new insight in the general structure of the superfamily. These two proteins are thought to be directly related to the ancestor of the mammalian pLGIC [18]. Their function has not been determined yet. The major structural difference with the mammals pLGIC is the lack of the intracellular loop between the transmembrane segment TM3 and TM4. The length of transmembrane spanning domains of both prokaryotic and eukaryotic pLGIC is comparable [17, 19, 20, 21].

The intracellular loop of eukaryotic pLGIC has two major functions: modulation of the channel gating and interaction sites for cytoplasmic proteins [175, 180, 181]. No structural data are available for the major part of this loop but refined structure obtained by cryo-electron microscopy revealed the existence of a α-helical structure termed MA helix [17, 175].

5HT$_3$R interacts with the myotubules trough MAP1B-Lc1(light chain of microtubule-associated protein 1B), this interaction modulates the pharmacology of the receptor [180]. Ric-3, a chaperone, has been found to be essential for receptor subunits composition and trafficking to plasma membrane [182, 183]. In HEK 293 cells, Ric-3 is not

endogenously expressed [120], unlike MAP1B-Lc1 [180].

7.2.2   Protein labeling

General methods to label proteins in living cells are prerequisite to image proteins over time and space within a cell.

Methods involving short tags introduced in the protein sequence have been widely used for membrane protein labeling [107]. $5HT_{3A}R$ has been labeled in living cells using a metal-chelating groups such as oligohistidine tagged proteins and an organic fluorophore coupled to a nickel-nitrilotriacetate (NTA) [108, 173]. Short tags such as hexahistidine or decahistidine are widely used in protein affinity-purification. Histidine-tag labeling of polyhistidine sequence is fast and reversible and, therefore, is ideally suited to stain membrane proteins on the extracellular surface. However, the complex between the probes and the protein has a short lifetime of $\tau_{1/2} = 27$ s. Different strategies have been used to circumvent this drawback by increasing the affinity of the label for the tag. Molecules containing multiple nitrilotriacetate moieties (*bis-*, *tris-* and *tertrakis*-NTA) have been developed and exhibit strongly increased affinites for his-tagged proteins [109]. The *tris*-NTA-chelator has been used successfully as a very specific and long-interacting, virtually irreversible probe to explore protein complex formation [100]. Mono- and *tris*-NTA have been coupled on quantum dots surface, yielding very useful but large and potentially multivalent probes [115, 184]. Here, we used a new NTA-chelator combining the highly photostable fluorescent dye Atto647N [111], and the high affinity label *tris*-NTA-with a linker containing 8 prolines, that greatly enhanced the brightness of the probe. This new probe increased the single-molecule precision localization and the length of the traces.

7.2.3   Single-particle tracking of membrane proteins

Since the first experiments of single-molecule tracking in cells with colloidal gold particles [89] and fluorescent dyes [92], major advances have been made on the understanding on the function and structure of cell plasma membrane. The initial fluid lipid mosaic model with random distribution of membrane protein within the lipid bilayer [2] has been refined to obtain a model where lipids and proteins are dynamically partitioned in domains that can be of small size (down to a few nanometer) and short lived [12, 13, 9].

7.2.4   Diffusion of the serotonin type 3 receptor

$5HT_3R$ movements in the HEK cell membranes has been shown to be highly heterogenous [173], which could be related to numerous interactions with cytoplasmic and plasma-membrane components. In this work, we used single-molecule tracking to study variations in the diffusion properties of the wildtype $5HT_3R$, and receptors where different

deletions of the intracellular loop have been made (fig. 7.1). For comparison, we included in this study ELIC, a prokaryotic homologue of pLGIC, which lacks the M3-M4 intracellular loop. To enable labeling with Atto647N-8Pro-*tri*-NTA, all constructs comprised a C-terminal oligohistidine tag.

7.3   Material and methods

7.3.1   Molecular biology

Mouse $5HT_3R$ cDNA carrying a decahistidine-tag in the pEAK8 vector (Edgebio) was used as template for 7 deletions in the cytoplasmic loop of the receptor subunits (Δ337-413, Δ337-422, Δ337-446, Δ343-413, Δ343-422, Δ350-413, Δ350-422,). These deletions were made using 6 different primers (sense : 5'- CCA AGG GAG GCC TCA CTG GCT GTG CGT GGT -3', 5'- GGT CTC TTG CAA GAG CTA TCC TCC ATC CGC -3', and 5'- GAC TGG CTG CGG GTG GGA TAC GTG CTG GAC -3', anti-sense : 5'- CTT ATG CAC CAG CCG CAC AAT GAA GAT GGT -3', 5'- TGG CCG CTG TAG GTC CTG CTT ATG CAC CAG -3', and 5'- GAC TGG CTG CGG GTG GGA TAC GTG CTG GAC -3') using phusion DNA polmerase (Finnzyme). All these deletions were subcloned into the T-REx/Flp-In vector pcDNA5/FRT/TO vector (Invitrogen).

cDNA encoding ELIC a kind gift of Raimund Dutzler [19], it was subcloned into pcDNA5/FRT/TO behind the $5HT_{3A}$ signal sequence and followed by a decahistidine tag. All constructs were confirmed by sequencing.

His_{10}-EGFP was expressed in *E.coli* and purified as described elsewhere [108].

7.3.2   T-REx/Flp-In cell lines

Stable cell lines were generated using FRT translocase based expression system. T-REx/Flp-In 293 (Invitrogen), HEK 293 cells carrying a single genomic integration site, were transfected with Fugene 6 (Roche) at 80 % confluency using 0.25 μg pcDNA5/FTR/TO containing the receptor constructs and 0.75 μg pOG44 (Invitrogen) per well in 12-wells plate. Positive cells were selected using 100 μg/ml hygomycin (Sigma) and 100 μg/ml blasticidin (Invitrogen).

T-REx/Flp-In 293 cells were maintained in DMEM/F12 (Gibco) supplemented with 100 μg/ml hygromycin (Sigma) and 100 μg/ml zeocin (Invitrogen). Cells were split when reaching 80% confluency.

7.3.3   Metal chelator affinity tags

Two metal chelators affinity tags have been used in this study (fig. 7.2). A *tris*-NTA-8Pro-Atto647N where the fluorophore Atto647N is coupled to a *tris*-NTA moiety [109]
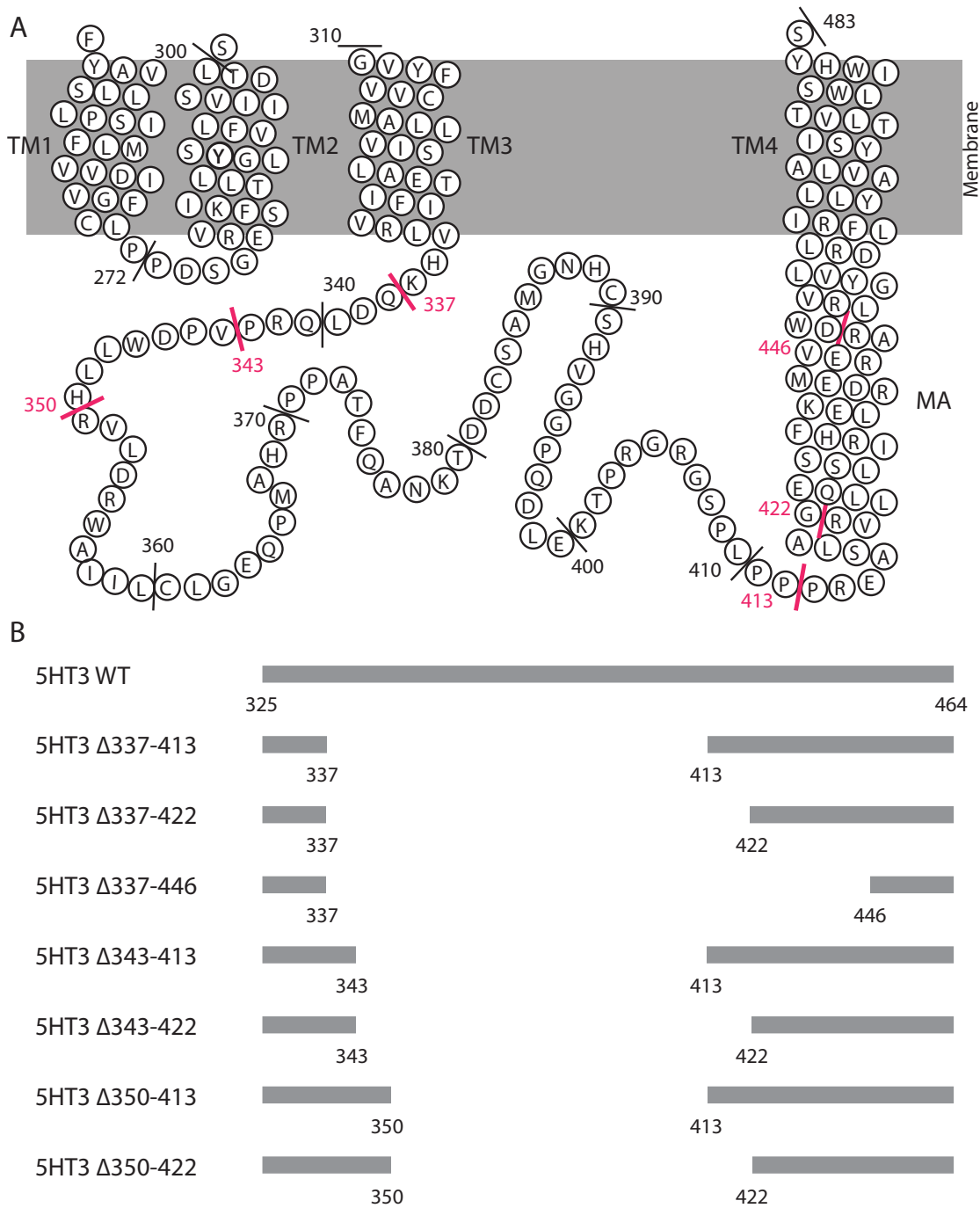
Figure 7.1: Scheme of the amino acid sequence of the 5HT$_{3A}$ receptor. A. Model of the topology of the membrane traversing and intracellular part of the 5HT$_{3A}$ starting from the first transmembrane helix (TM1). The extracellular loop between TM2 and TM3 has not been depicted for clarity. Red amino acids are starting and ending points for deletions **B.** Schematic representation of the different deletion in the TM3-TM4 loop. The exact size of the loop has not been completely determined yet.

with a linker composed of eight prolines and a NHS group and *tris*-NTA-Atto647N where the dye is directly coupled to the *tris*-NTA with a NHS group.
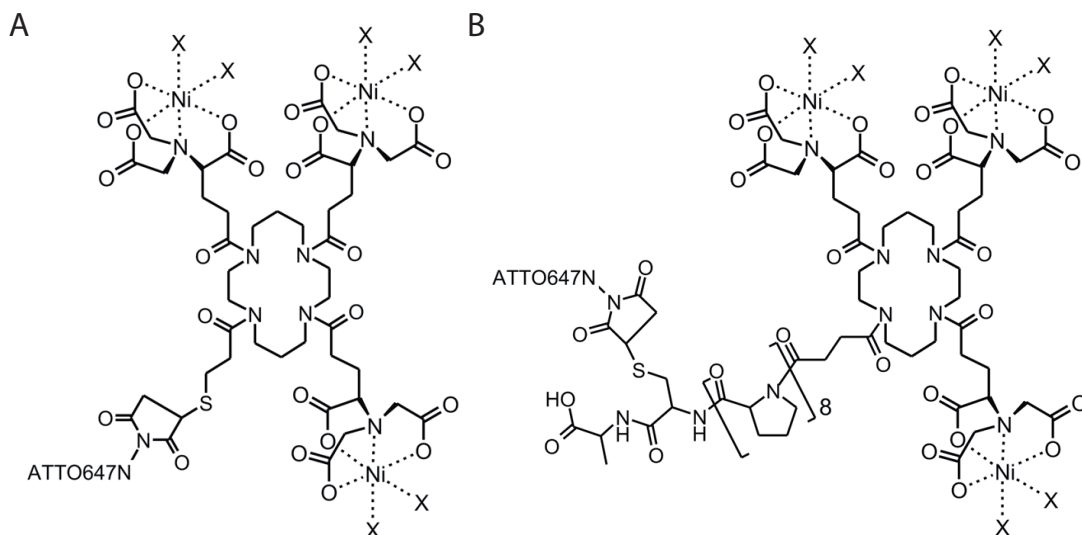
Figure 7.2: Structure of the *tris* **-NTA affinity tags. A.** *tris*-NTA-Atto647N. The dye is directly bound to the *tris* moiety by a NHS. **B.** *tris*-NTA-8Pro-Atto647N. An octa-proline linker has been added between the dye and the *tris* moiety.

7.3.4 Ligand characterization

Fluorescence intensity measurements were performed on a SPEX Fluorolog II (Instruments S.A.) using 3.6 and 1.8 or 7.2 nm band passes for excitation and emission, respectively. The solutions were placed in 10 x 4 mm quartz cuvettes (Hellma) and were continuously stirred with a magnetic bar. Emission spectra of Atto647N were acquired from 605 to 750 nm upon excitation at 600 nm. Kinetics of Tris-NTA-Atto647N binding to His10-EGFP by measuring EGFP fluorescence at 520 nm upon excitation at 488 nm.

The rate constants (k_{on} and k_{off}) and the dissociation constant (K_d) were measured on His_{10}-EGFP as described elsewhere. [108]. Four concentrations ranging from 10 to 100 nM of *tris*-NTA compounds were added to 1 nM of fluorescent protein in PBS buffer supplemented with 80 μM C12E9 detergent to suppress interaction of fluorophores with EGFP. The specificity of binding was tested by addition of a final concentration of 12.5 to 25 mM EDTA.

The fluorescence lifetime of the free and bound to His_{10}-tag was measured on a home-built lifetime imaging setup. The lifetime of *tris*-NTA-8Pro-Atto647N and *tris*-NTA-Atto647N was measured at 10 nM of affinity ligand in PBS only, with 25 mM EDTA at pH 7.4, or with 124 nM His_{10}-EGFP.

7.3.5 Receptor labeling

Three days before measurements, cells were seeded on 0.17 mm glass coverslips and grown in DMEM/F12 supplemented with 10% FBS. Expression of proteins of interest was induced by adding tetracycline (Sigma) to the medium to a final concentration of 5 μg/ml 36 hours prior to measurements. Standard cell medium was changed 12 h before measurements to DMEM containing 15 mM HEPES (Invitrogen) supplemented with 2% FBS but without phenol red.

Receptor proteins have been labeled by adding *tris*-NTA-Atto647N (8-pro) or *tris*-NTA-Atto647N to a final concentration of 100 pM for 30 min without changing the culture medium. Then, cells were rinsed twice with DMEM supplemented with 15 mM HEPES without phenol red before measurements.

7.3.6 Calcium assay

Inducible T-REx/Flp-In 293 cell lines were seeded into black clear bottom 96 well plates (Wallac) 3 days before experiments. Cells were induced with tetracycline at a final concentration of 5 μg/ml 36 hours prior to measurements. Assays were performed using a microplate reader (Flexstation, Molecular Devices).

Fluo-4 NW (Invitrogen) fluorescent calcium dye was loaded into cells according to manufacturer instructions. m-chlorophenylbiguanide was added after 18 seconds to a final concentration of 10 μM. Fluorescent dye was excited using a 488 nm excitation bandpass filter and detected above 515 nm.

7.3.7 Microscopy

Single-molecule microscopy was performed on an Axiovert 200 inverted microscope (Zeiss) with a wide-field illumination. A 632.8 nm He-Ne laser was directed to the back aperture of an Apochromat 63x water immersion objective (Zeiss) by a 645HQ dichroic mirror (Chroma). The system was set to give a 20 μm diameter region at an intensity of 0.5 kW/cm^2. Resulting fluorescence was filtered out by the same dichroic and a 710/100HQ bandpass filter (Chroma) and finally detected using an Ixon 887BV electron-multiplied CCD (Andor). Images were acquired at 20 Hz in frame transfer mode with an effective acquisition time of 49.86 ms per frame.

Confocal micrographs were taken using a LSM510 confocal microscope (Zeiss) using the 488 nm line of a Ar laser. Fluorescence was detected using photomultiplier tubes (PMT) or avalanche photo diodes (APD) depending on the experiment.

7.3.8 Data treatment

Single molecule images were analyzed using a home-made software running on Igor Pro 6 (Wavemetrics) [185]. Briefly single-molecule fluorescence peaks were searched in each frame of the image sets, and were tested for intensity, geometry and single-step photobleaching to remove aggregates, CCD spikes and bright autofluorescence spots. Single-molecule position were tracked over consecutive frames of the entire movie to obtain single-molecule trajectories. The mean square displacements (MSD) were calculated for each time interval (t_{lag}) within each trajectories, yielding MSD vs (t_{lag}) plots. The shape of these plots is correlated to the type of diffusion; free-brownian motion, diffusion in confined domains, directed motion and anomalous diffusion (fig. 7.4) [129].

7.4 Results

7.4.1 Ligand binding

Both *Tris*-NTA compounds are binding decahistidine tags with a picomolar affinity (Table 7.1).

Table 7.1: *Characterization of* tris-*NTA compounds*

Parameters	*tris*-NTA-Atto647N	*tris*-8Pro-NTA-Atto647N
QY^a [τ (ns)] + EDTA^b	1.0 [3.99 ± 0.02]	1.0 [3.94 ± 0.02]
QY^a [τ (ns)]	0.31 [2.137 ± 0.007]	0.84 [3.38 ± 0.01]
QY^a [τ (ns)] + His$_{10}$-EGFP^c	0.24 [1.709 ± 0.004]	0.65 [3.42 ± 0.01]
k_{on} ($M^{-1}s^{-1}$)	($1.9 \pm 0.1) \cdot 10^6$)	($1.9 \pm 0.1) \cdot 10^6$)
k_{off} (s^{-1})	($1.4 \pm 0.2) \cdot 10^{-4}$)	($1.5 \pm 0.1) \cdot 10^{-4}$)
K_d (pM)	74 ± 4	79 ± 4
Position precision^d (nm)	23	10

200 mM of *tris*-NTA compounds. ^{a} quantum yield relative to Atto647N in presence of 12.5 mM EDTA assuming a constant molar extinction coefficient. ^{b} 12.4 mM EDTA. ^{c} In presence of 11 μM His$_{10}$-EGFP. ^{d} Maximal position precision obtained during single-molecules experiments.

7.4.2 Receptor expression and functionality

Stable inducible HEK 293 cell lines of 5HT$_{3A}$R with loop deletions and ELIC in pcDN5/FRT-TO vectors were established using the T-REx/Flp-In system. Two weeks after transfection cells were growing in selection medium and were expressing proteins after induction with tetracycline.

Expression of receptors on the cell surface was measured 36 hours after induction by tetracycline, staining cells with the high affinity fluorescent antagonist GR186741X [186] using a standard confocal microscope. On the six tested deletion mutant receptors, five exhibited significant membrane staining. The Δ337-422 deletion did not show fluorescent staining (data not shown).

The expression of the $5HT_3R$ constructs was quantified by a saturation radioligand binding essay using ^3H-GR65630, yielding the average number of receptors per cell and the receptor affinity for the radioligand (K_D). This expression level is comparable to the wildtype receptor under the same conditions (Table 7.2) for all the constructs except the Δ337-422, which was not functional.

Table 7.2: *Characterization of $5HT_{3A}R$-mutants: K_D values for radiolabeled antagonist $[^3H]$-GR65630 and serotonin-induced channel gating*

Mutant	K_d (nM) for GR65630	Channel gating
wt-$5HT_{3A}$	0.31 ± 0.03	$EC_{50} = 0.2\ \mu M^a$
Δ337-413	0.23 ± 0.06	
Δ337-446	0.37 ± 0.15	
Δ343-413	0.21 ± 0.05	
Δ343-422	0.14 ± 0.02	
Δ350-413	0.13 ± 0.04	
Δ350-422	0.15 ± 0.02	

^{a} EC_{50} values of the channel gating has been measured by fluorescence spectroscopy. This value is comparable to those obtained by electrophysiology (1 μM).

Δ343-413 and Δ350-422 constructs in pEAK8 vector were transiently expressed in HEK 293 cells. Membrane expression was investigated by confocal microscopy with GR-Flu staining. Both constructs exhibited membrane staining.

Receptor functionality of inducible cell lines was tested using an intracellular calcium assay. Δ337-413, Δ337-446, Δ343-422, and Δ350-413 responded to serotonin addition (fig. 7.3). No response was observed for Δ337-422 cell line. Signal was normalized to the response of non induced T-REx/Flp-In 293 cells.

7.4.3 Receptor labeling and tracking using *tris*-NTA-8Pro-Atto647N probe

In this study, we used two new *tris*-NTA-Atto647N affinity label combining the relative photostability of the Atto647N dye and the nanomolar affinity of the *tris-NTA* to the decahistidine-tag .
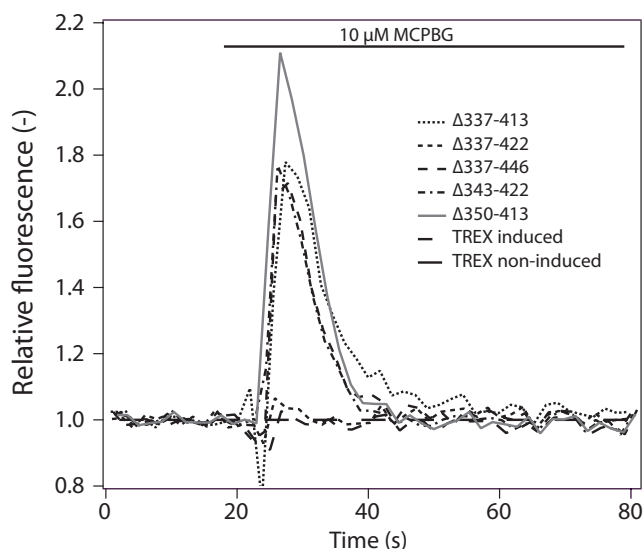
Figure 7.3: Calcium ion concentration in cells expressing 5HT$_3$R with modified intracellular loops after addition of receptor agonist. The calcium signal was measured after addition of 10 μM MCPBG. Response curves were normalized by the signal of non-induced T-REx/Flp-In 293. Fluo4-NW calcium dye was excited at 488 nm and fluorescence was detected above 515 nm.

Receptors were labeled using 100 pM *tris*-NTA-8Pro-Atto647N or *tris*-NTA-Atto647N. After rinsing, bright fluorescence spots were visible on the upper cell membrane of cell expressing 5HT$_{3A}$R variants with both affinity label. Fluorescence peaks have been tracked up to 2000 video frames until single-step fluorescence disappearance, equivalent to 98.6 s of total illumination. However, measurements have been limited to 300 frames to avoid changes in cell shape and large data files. The median length of the complete set of trajectories was 131.

The use of the *tris*-NTA-Atto647N with a 8-pro linker allowed to obtain a lateral precision down to 10 nm, while for the probe without the linker this was only 23 nm. This enhanced precision can be explained from the higher brightness of the probe with the 8Pro linker due to reduced quenching or non-radiative de-excitation of the Atto647N.

7.4.4   pLGIC diffusion in the plasma membrane

Diffusion for the 5HT$_{3A}$R wild type and the different loop deletions along with ELIC has been measured in the plasma membrane of living HEK 293 cells using single molecule tracking. Three kinds of receptor mobility were observed; immobile, free-diffusing and directed diffusion. Fig. 7.4 shows the corresponding MSD vs t_{lag} plots. Only a few, $<$ 5%, of the receptors were diffusing in confined regions.
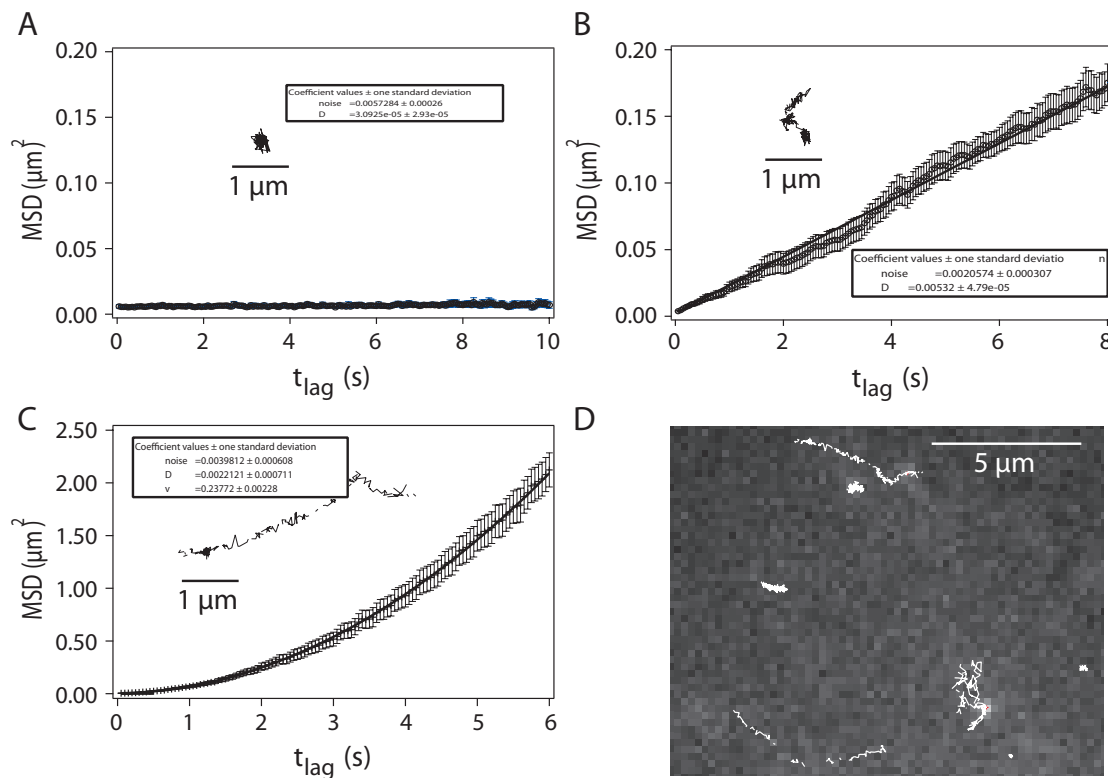
Figure 7.4: Typical examples of the three different diffusion modes measured in this study. A. An immobile 5HT$_3$R-Δ350-413 receptor with a MSD that does not increase with t$_{lag}$. The position of this molecule has been measured with a precision of 38 nm. **B.** A 5HT$_3$R-Δ350-413 freely moving with a diffusion coefficient of 5.32 $\pm$ 0.05$\cdot$10^{-3} μm^2/s **C.** 5HT$_3$R-Δ337-413 featuring directed motion characterized by an initial diffusion coefficient of 2.2 $\pm$ 0.7$\cdot$10^{-3} μm^2/s and a velocity of 237 $\pm$ 3 nm/s. Y-scale is 12.5 larger than A and B. **D.** T-REx/Flp-In 293 cell expressing 5HT$_3$R-Δ337-413 labeled with *tris* NTA-8Pro-Atto647N. The different types of diffusion are visible on the upper membrane of the cell.

The initial diffusion coefficient was extracted from each single-molecule trajectory. In order to increase the quality of the estimated value, an algorithm was developed to fit the MSD vs t_{lag} curve until the MSD deviated from linear time-dependence. Briefly, data were fitted between the first and ith t_{lag} starting with i=5. The value of i was increased iteratively and for each fit a normalized chi-square value was evaluated. Each calculated value was compared to the distribution of all the precedent chi-squares. The iteration loop stopped when the last chi-square was significantly different from the previous (p<0.05). The distribution of the resulting initial diffusion coefficients, D_{init}, is shown in fig. 7.5.
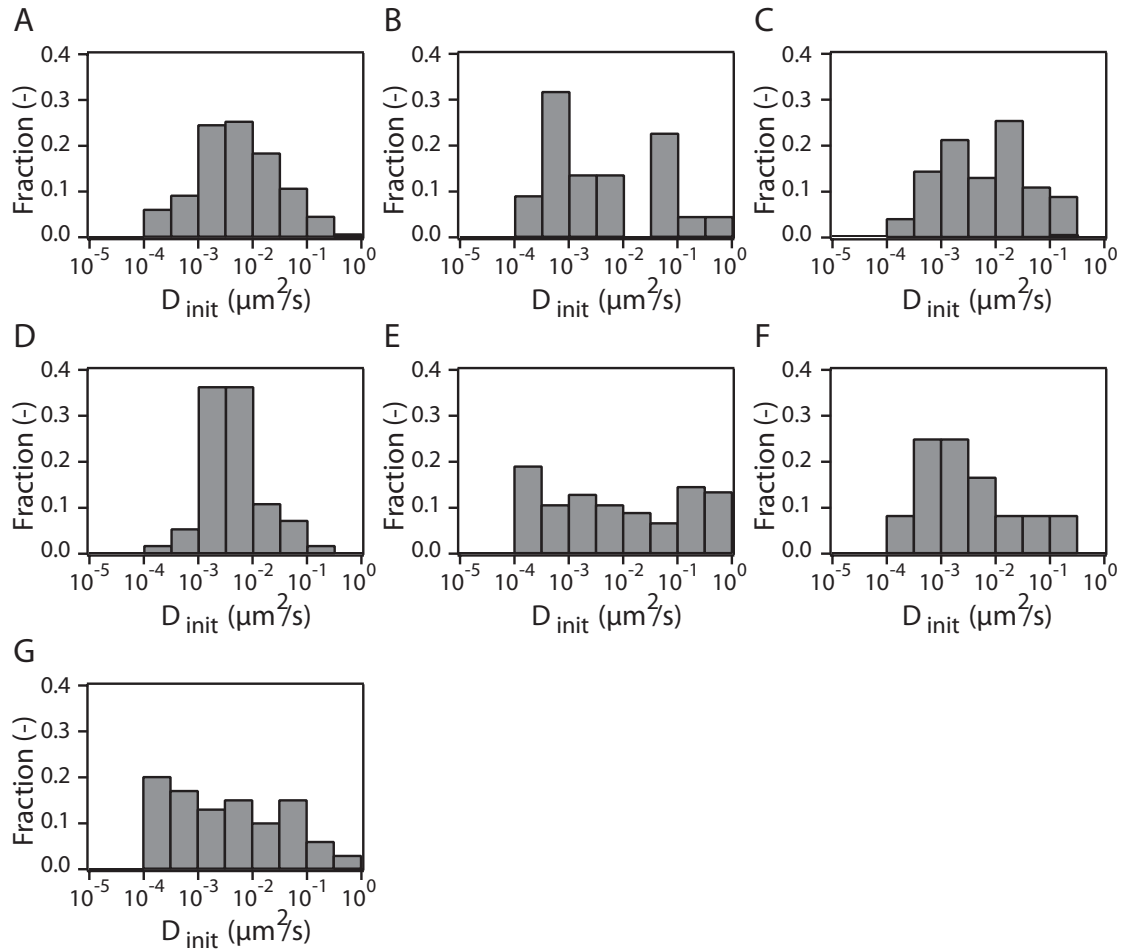
Figure 7.5: Distribution of the initial diffusion coefficient of mobile and directed receptors with logarithmic bins. A. Δ337-413, **B.** Δ337-446,**C.** Δ343-413, **D.** Δ343-422, **E.** Δ350-413, **F.** Δ350-422,and **G.** Δ350-422. The variability of the initial diffusion coefficient is very low. No significant difference has been observed using a ranking comparison test (Mann-Whitney U-Test).

The MSD vs t_{lag} plot of the trajectories were fitted for directed motion using eq. 4.12.

For each 5HT$_3$R deletion mutant and for ELIC, the fraction of molecules exhibiting a velocity, v, above 12 nm/s was determined. This value was chosen to be independent of motion coming from the measurement system (microscope stage shift or cell movements). The seven proteins studied formed two distinct groups; the first composed of 5HT$_3$R mutants Δ337-413, Δ343-413 and Δ350-413 had a fraction of receptors with directed diffusion below 20% and the second containing Δ350-446, Δ343-422, Δ350-422 and ELIC had a fraction of receptors with directed diffusion above 25 %. Results are shown on fig. 7.6A. The fraction of receptors with directed diffusion is related to the presence of the region comprised between a.a. 413 and 422. The fraction of ELIC with directed diffusion is comparable to three of the receptors lacking the 413-422 region.

Receptors with an initial diffusion coefficient below 10^{-4} μm^2/s were considered as immobile. Below this threshold, it was not possible to measure D$_{init}$ accurately due to cell movements and noise. The fraction of immobile receptors for the different proteins formed two well-defined groups, one with the immobile fraction below 20 % for Δ337-413, Δ337-446, Δ343-413, Δ343-413 and the other with the fraction above 30% for Δ350-413, Δ350-422 and ELIC (fig. 7.6B). The immobile fraction of receptor is related to the presence of the region between the amino acids 343 and 350. The immobile fraction of ELIC is high and comparable to receptor having the region 343-350.
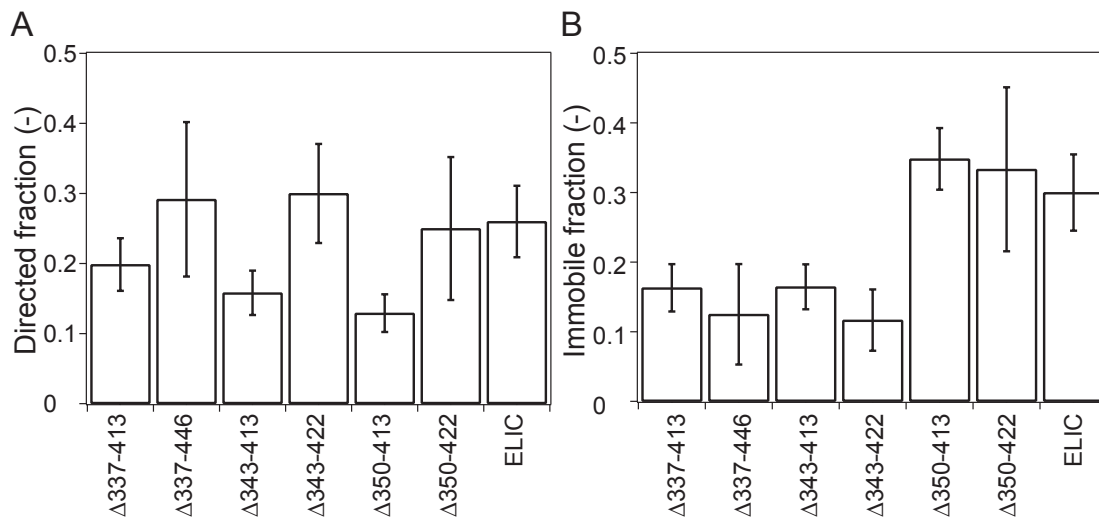
Figure 7.6: Receptors showing directed diffusion and immobile receptors. A. Fraction of receptors showing directed diffusion. These receptors are diffusing with a velocity higher than 12 nm/s. **B.** Fraction of immobile receptor. A receptor is considered as immobile when its initial diffusion coefficient is lower than $1 \cdot 10^{-4}$ μm^2/s. Error bars in A and B stem from counting noise.

Initial diffusion coefficients of receptors that were not classified as directed motion or immobile were not significantly different (Mann-Withney U-test). Some of these

receptors ($< 5\%$) diffused in confined domains as previously described [173]. Thus, they were classified as mobile receptors.

7.5   Discussion

7.5.1   Labelling with *tris*-NTA-Atto647N on histidine tag

We measured the diffusion of pLGIC using a new affinity label for single molecule tracking. The ease of use of labels based on Ni-NTA interaction with histidine have been previously demonstrated [173]. The combination of a relatively photostable organic dye and a high affinity multivalent chelators had two new major effects. (i) It was possible to measure many cells after one labeling step while keeping the possibility to reverse and renew the labeling. (ii) The length of single molecule trace was substantially increased compared to receptor labeled with mono-NTA chelator. The increased trace lengths allowed to determine diffusion coefficients down to 10^{-4} $\mu\mathrm{m}^2/\mathrm{s}$, more than one order of magnitude lower than previous experiments performed on the same microscope setup [185, 173]. The 8-proline linker increased the brightness of the Atto647N dye, and in turn the positional accuracy to less than 20 nm. It is well known that the metal ion complexed by NTA decreases fluorescence intensity of the attached probe [187]. This increase was not observed in all the measured trajectories, mainly because of the cellular autofluorescence.

7.5.2   Diffusion of 5HT3 loop deletion mutant proteins

The intracellular deletions are not altering the binding activity of $5\mathrm{HT}_3\mathrm{R}$ to the $^3\mathrm{H}$-GR65630, whereas the motion of the receptors was notably modified. The deletions modified two main parameters; the fraction of receptors featuring directed motion or the immobile receptors. We did not observe change in the fraction of receptor diffusing in confined region

For all the construction a non-negligible fraction of the receptors exhibited directed motion even after correction of the drift of the measurement system. This fraction of receptors with directed motion was increased in the deletion that missed nine amino acids between 413 an 422 (PREASLAVR) in the putative intracellular MA-helix and in ELIC. Directed motion is linked to an active transport of protein in the cell membrane. There are no known functional reason which could explain an active transport of these receptors This transport could be related to a general pathway for removal of non functional proteins from the plasma membrane. The determined amino acid sequence could therefore serves as a recognition motif used to maintain pLGIC in the membrane. However, the velocity of the directed motion was evenly distributed from 12 to a few hundred nm/s. It was thus difficult to relate the motion to the activity of a particular

motor.

In the present study, we found that the mobility of the 5HT3R was strongly affected by the deletion of seven amino acids between 343 and 350 (VPDWLLH). This region is thought to be part of a predicted small alpha-helical region in the predicted unstructured intracellular region termed MX.

$5HT_{3A}R$ are not natively expressed in HEK 293 cells; these cell line is used extensively as an heterologous expression system for ionotropic receptors [188]. Recently, MAP1B-LC1, a myotubule associated protein, was identified as an interacting and modulating protein of the $5HT_{3A}R$ in neurons. This protein was found to be natively expressed in HEK cells [180]. The interaction of this cytoskeleton related protein could be related to $5HT_{3A}R$ immobilization or directed motion.

7.5.3   Diffusion of ELIC

We expressed ELIC in T-REx/Flp-In HEK cells.The structure of this prokaryotic ligand-gated ion channel was the first to be determined by X-ray crystallography [19]. The major interest of this protein for this work was the lack of the large intracellular part, moreover, this protein was assumed not to interact specifically with the mammal cytoskeleton and be a protein featuring simple free diffusion in the membrane with a size comparable to $5HT_{3A}R$. However, the diffusing scheme of ELIC presented two unexpected characteristics. First, a high fraction of directed motion similar to deletions of the $5HT_{3A}R$ lacking the 413-422 amino acids sequence was observed. This motion might also stem from membrane protein trafficking and recycling. A large immobile fraction, comparable to the short $5HT_{3A}R$ deletions mutant, containing the amino acids 343 to 350, was found. This restriction in motion cannot be explained by only membrane properties. These unexpected features could stem from the strong structural similarity between ELIC and the mammalian pLGIC. They can be related to similar membrane partitioning or common recognition strutures.

7.6   Conclusion

We measured the diffusion of $5HT_{3A}R$ with different deletions of the intracellular loop between the transmembrane helix M3 and M4. Two loci of putative recognition or interactions of the $5HT_{3A}R$ with cytoplasmic proteins were identified. The diffusion of a prokaryotic pLGIC, ELIC, in the mammalian cell plasma membrane was also measured yielding an unexpected large immobile fraction for a protein lacking a large intracellular loop.

Fluorescent rapsyn

8.1 Abstract

Rapsyn is one of the most important scaffolding proteins in the postsynaptic side of the neuromuscular junction. Rapsyn links nAChR to other components of the NMJ and stabilizes the postsynaptic density. It is, therefore, essential for proper neuronal signal transmission from motor nerves to muscle fibers.

Rapsyn-deficiency provokes myasthenia. Point mutations in rapsyn have been found to lead to severe diseases in human. In this chapter, we studied the expression of fluorescent rapsyn derivatives, which each contains one of four such mutations (i.e. A25V, N88K, R91L and L361R), that change rapsyn distribution in HEK cells. A25V increased rapsyn retention in endoplasmic reticulum. N88K and R91L decreased the membrane localization of rapsyn. Finally, L361R was expressed but not located at the cell plasma membrane. Rapsyn forms oligomers at the plasma membrane. FRET measurements between co-expressed rapsyn mutants showed difference in the oligomerization level for different mutants. Rapsyn patches at the cell plasma membrane seem to be weakened by mutations.

Thanks to its high enrichement and high density in NMJ, rapsyn can be used as a neuromuscular junction marker. We developed several fluorescent derivatives of rapsyn to measure density, shape of rapsyn patches, and function of NMJ.

We have genetically engineered a rapsyn fused with a FRET ratiometric calcium sensor. This sensor was functional in HEK 293 cells.

A library of photo-activatable and photo-switchable fluorescent derivatives has been built. Preliminary experiments have permitted activation of a fluorescent protein fused to rapsyn.

Finally, a mammalian expression plasmid containing the mouse rapsyn promoter has been genetically engineered to avoid protein overexpression and accumulation in the

expression pathway. This plasmid has been shown to express a rapsyn A25V-CFP fusion fluorescent derivative in C2C12 myoblasts.

This rapsyn-based fluorescent toolbox for the study has not been completely tested yet. The preliminary experiments performed up to now were very promising for future work to study the NMJ using cultured cells.

8.2   Introduction

Rapsyn, initially known as 43 kDa protein, is an essential protein of the neuromuscular junction, and is anchored to the cell plasma membrane by a myristoyl moiety. It is essential for proper NMJ functioning as a linker between several important NMJ components through its different interacting regions (see section 1.5 and fig. 1.3 of the introduction for an extensive description).

In this study, we were interested in the formation of rapsyn clusters, and their stability and shape. When transfected in mammalian cells rapsyn spontaneously clusters at the cell membrane, forming dense patches. The density of these patches is strongly dependent on the strength of rapsyn self-interaction.

This chapter present fluorescent and genetic tools that were developed to study rapsyn in living cells. They were designed to probe the localization, shape and density of rapsyn clusters and to probe the functionality of the synapses containing rapsyn in muscle cells and in HEK cells.

A cassette system was developed in order to easily modify the C-terminal fluorescent protein linked to the mouse wild-type raypsyn coding sequence [69]. This versatile cloning system based on rapsyn was used to construct multiple coloured derivatives from cyan to cherry, fluorescent-based Ca^{2+} indicators and photo-switchable mutants.

An engineered expression plasmid containing the C2C12 native rapsyn promoter was made for the expression of rapsyn in muscle cells at native levels.

8.2.1   Rapsyn expression in muscle cells

Rapsyn is expressed at an almost constant level at every stage of muscle development. Its promoter is regulated by kaiso and δ-catenin [189]. Rapsyn turnover is very fast in C2C12 cells [80]. Expression and turnover of rapsyn are not correlated to that of nAChR in C2 muscle cells [66].

8.2.2   Fluorescent proteins

Since the discovery and cloning of the green fluorescent protein (GFP) from *Aequoria victoria* , the use of fluorescent has become an essential tool in cell biology [190]. In *Aequoria victoria* , GFP converts the blue chemiluminescence of aequorin, to green

fluorescence. The generalized use of GFP began with the heterologous expression of the protein in *E. coli* and *C. elegans* [191]. Fluorescent proteins have been modified for an enhanced expression in mammals [192]. GFP has been used early for a wide range of applications (reviewed by R. Tsien [190])

Up to now, dozens of fluorescent proteins have been cloned and mutated to give a library of color and functionality . A large choice of fluorescent reporters is available with emission spectra ranging from blue to far-red (for example see [193, 194, 195, 196, 197]. During the last fifteen years the fluorescent proteins have enabled a giant step forward for imaging living cells *in vivo* and *in vitro* [198].

Fluorescent protein based calcium sensors — Cellular calcium is one of the most important signal messengers in living organisms. The propagation of the action potential in the central nervous system is mediated by changes in intracellular calcium concentration. Calcium is also involved in muscle contraction. For two decades, calcium sensing has been a very important research area.

Calmodulin-based calcium sensors are based on fluorescent proteins and calmodulin [199] [200]. These genetically encoded fluorescent Ca^{2+}-indicator proteins have been widely used for *in vivo* calcium level determination. They have been used to measure single-action potentials in living mice [201].

D2cpv and D3cpv are sensors composed of a CFP linked to variant of the genetically engineered yellow fluorescent protein, venus [202]. The linker between both fluorescent proteins is composed of a calmodulin (CaM) and M13, the CaM-binding peptide of skeletal muscle myosin light chain kinase. Upon calcium addition, the affinity of M13 for CaM is increased and the shape of the linker is modified, changing the distance between the two fluorescent proteins. Several modifications has been made on the sensor. CaM has been genetically modified to modulate its affinity for calcium ions. Furthermore, venus has been circularly permuted (cpv) to modify the relative orientation of the donor and acceptor fluorophore and therefore increase the FRET efficiency of the sensor when calcium is bound.

Photo-switchable proteins — Photo-switchable proteins can undergo changes in their absorption and/or emission spectra upon irradiation by light of a certain wavelength. This phenomenon was first observed on YFP by R. Tsien and coworkers [203]. An engineered stable photo-activatable derivative of GFP was released in 2002 [204]. Several photo-activatable and photo-switchable fluorescent proteins have been cloned and used in microscopy.

The first experiments involving photo-activatable proteins in living cells dealt with protein expression, trafficking, and motion [205]. They were quickly used for nanometer resolution optical microscopy with the invention of photo-activated localization mi-

croscopy (PALM or FPALM) [206]. Along with other recent super resolution techniques, PALM has dramatically changed microscopy on living cells.

8.3   Material and methods

8.3.1   Molecular biology

All the standard molecular biology steps have been performed using the methods described in chapter 3. All chemicals were purchased from Sigma-Aldrich.

Fusion with fluorescent proteins — Rapsyn-GFP was a kind gift from Jonathan Cohen [69]. The original construct was a fusion protein between the mouse rapsyn and a humanized GFP [192]. The rapsyn coding sequence was subcloned in pEYFP-N1 and pECFP-N1 plasmids (Clontech) between HindIII and SacII. In order to simplify the subsequent fluorescent protein modifications, an NcoI site in the nucleotide sequence of rapsyn was removed by a silent mutation (675 A->G). This mutated rapsyn was subcloned in pEAK8 (Edgebio) lacking NcoI restriction site using HindIII and NotI. This construct was designed as a cassette system having the possibility to easily exchange the fluorescent protein by simple molecular biology steps (fig. 8.1). This plasmid was called p8NC.

Two ratiometric Ca^{2+} sensors, D2cpv and D3cpv, were subcloned in p8NC using the cassette system. These sensors were kind gifts from Roger Tsien.

A library of photo-switchable and photo-activatable fluorescent rapsyn derivatives, composed of mEOS2 [207], rsCherry, rsCherryrev [208], and PA-GFP [204] was constructed using the same cloning method. A photo-activatable was engineered by making three point mutations on the EGFP coding sequence, T203H, M153T and V163A, yielding PA-EGFP.

Rapsyn mutation — Mutation of rapsyn coding sequence were done using either Quikchange (Stratagene) or Phusion (Finnzymes). Primers were designed following the supplier's guidelines. Five different mutants were made; A25V, N88K, R91L, L361R and a deletion of the coiled-coil domain (CCdel). Mutation were performed on the rapsyn coding sequence in plasmids containing fluorescent proteins. Mutations were verified by sequencing.

Isolation of the muscle rapsyn promoter — Adherent C2C12 cells were trypsinized and centrifuged 5 min at 500xg at 4 ˚C. The pellet was resuspended in digestion buffer containing 100 mM NaCl, 10 mM Tris·Cl at pH8, 25 mM EDTA at pH8, 0.5% SDS and 0.1 mg/ml proteinase K. The sample was incubated with shaking at 50 ˚C for 18h. It was
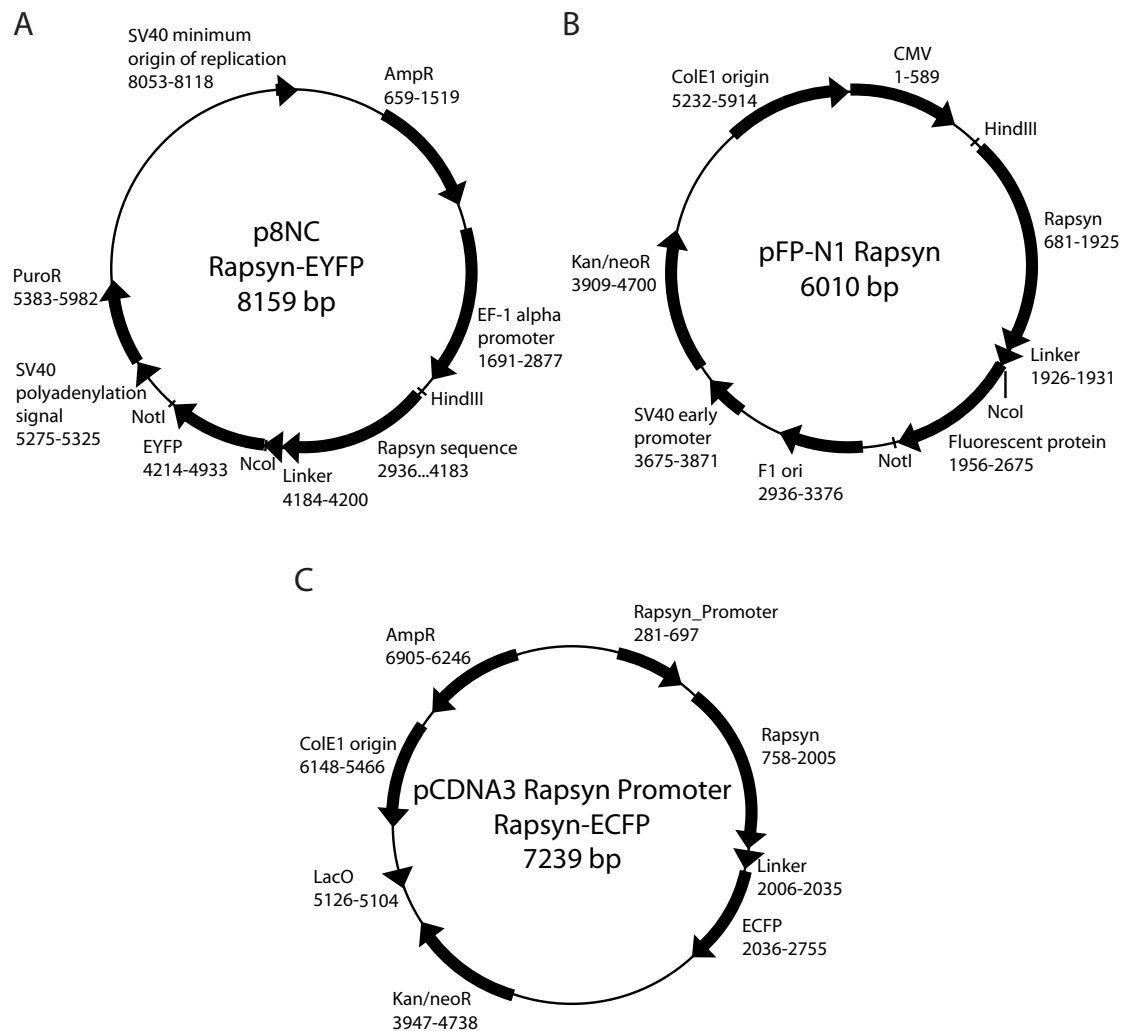
Figure 8.1: The expression vectors used in this chapter. A. A mammalian expression vector based on the commercial pEAK8 plasmid. This vector contains a cassette allowing the fast exchange of the fluorescent protein. This system was designed to be used with the Clontech pEGFP-N1 plasmid. **B.** Standard expression plasmid for fluorescent protein fusion constructs. **C.** pcDNA3 plasmid modified to contain the mouse rapsyn promoter.

then extracted with a phenol/chloroform/isoamyl mix. Genomic DNA in the aqueous fraction was then precipitated using 7.5 M ammonium sulfate and 100 % ethanol. DNA was dissolved in TE buffer.

PCR was made on 1 μl of the resuspended genomic DNA solution using a sense (5'-CCC AGA TCT GGG GGA ATG GGG TGG AAT-3') and an antisense (5'-CCC AAG CTT ATC TCT TTG TAG CGG CCC ATC-3') primers [189]. The PCR fragment was inserted between the BglII and HindIII restriction site of pcDNA3 (Invitrogen), replacing the original cytomegalovirus promoter of the plasmid. The final vector was verified by sequencing.
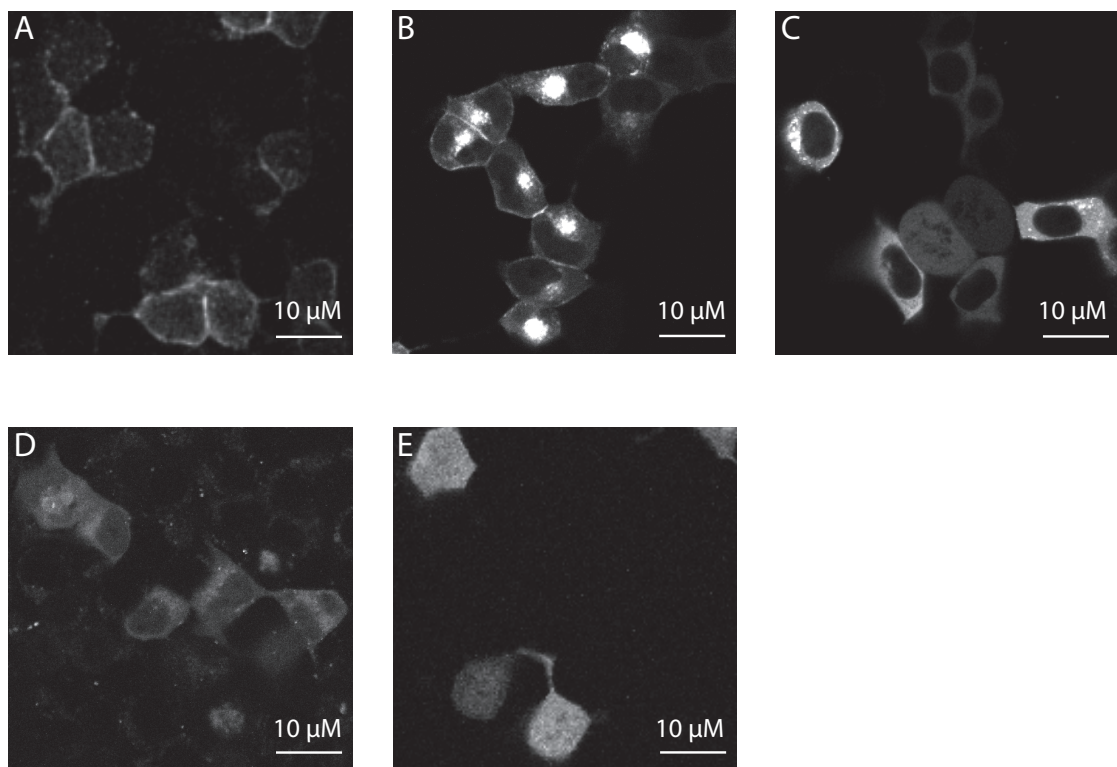
Figure 8.2: Confocal micrographs of fluorescent rapsyn mutants expressed in HEK 293 cells. A. Rapsyn-EYFP wild-type. **B.** Rapsyn-A25V-ECFP. **C.** Rapsyn-N88K-EYFP. **D.** Rapsyn-R91L-ECFP. **E.** Rapsyn-L361R-mCherry. Bars are 10 μm long. ECFP was excited at 458 nm, EYFP at 514 nm and mCherry at 562 nm. Fluorescence was measured using appropriate emission filters.

Cell transfection — HEK 293 T cells were transfected 24-36 hours before measurement using Fugene 6 transfection reagent (Roche) or Lipofectamin 2000 (Invitrogen). Transfection were performed with 1.5 μl Fugene and 0.5 μg of DNA or 8 μl of Lipofectamin and 4.8 μg of DNA for 1 ml of cell culture (5 cm^2 of adherent cells). When multiple

plasmid were transfected their proportions were calculated according to the total mass of DNA. Before every experiment transfection efficiency was estimated on a standard epifluorescence microscope (Zeiss). No measurements were made with a transfection efficiency lower than 60%.

8.3.2 Microscopy

FRET and proteins localization — FRET measurement were made on a confocal and a wide-field microscope. Cells were transfected with rapsyn fused to ECFP and mCitrine. Each experiment required transfection of the donor alone, the acceptor alone and at least one mixture of both.

Each quantitative FRET measurement required the acquisition of four images, donor channel with direct excitation at 458 nm (D), acceptor channel excited at 514 nm (A), acceptor channel excited at 458 nm (F) and a transmission image. Images resulting from transfection of ECFP alone or mCitrine alone were used as calibration for the calculation of the correction factors described in section 5.1.5.

FRET microscopy evaluation was performed according to the methods described in chapter 5. Calcium signaling measurements were performed using the ratio method and quantitative FRET was calculated with the method of Meyer et al. [144].

Photo-activatable proteins — Photo-switching of protein was made using the microscopy setup described on fig. 3.2 in chapter 3. Briefly, cells transfected with rapsyn-PA-EGFP were illuminated with a 405 nm laser at 50 W/cm^2 for 100 ms to photo-activate the fluorescent protein. Cells were then imaged using a 488 nm laser at 0.5 W/cm^2. Image were acquired using an iXon 887BV EMCCD (Andor) in frame transfer mode with an acquisition time of 100 ms and an EM gain of 211.

8.4 Results

8.4.1 Expression and localization of rapsyn in cells

Fluorescent rapsyn derivatives were transiently expressed in HEK 293 T and in C2C12 muscle cells. Two mammalian expression vectors, p8NC (the cassette plasmid described above, based on pEAK8) and pEFP-N1 were used featuring different promoters. In HEK 293 T, the expression level of fluorescent rapsyn was not significantly different for the to plasmids. In C2C12, the transfection efficiency was very low with p8NC plasmids and almost no expression was observed using pEFP-N1 plasmids (data not shown).

Rapsyn expression was measured by confocal microscopy in HEK cells. Fluorescent derivatives of wild-type rapsyn and four mutants were expressed using p8NC plasmid.
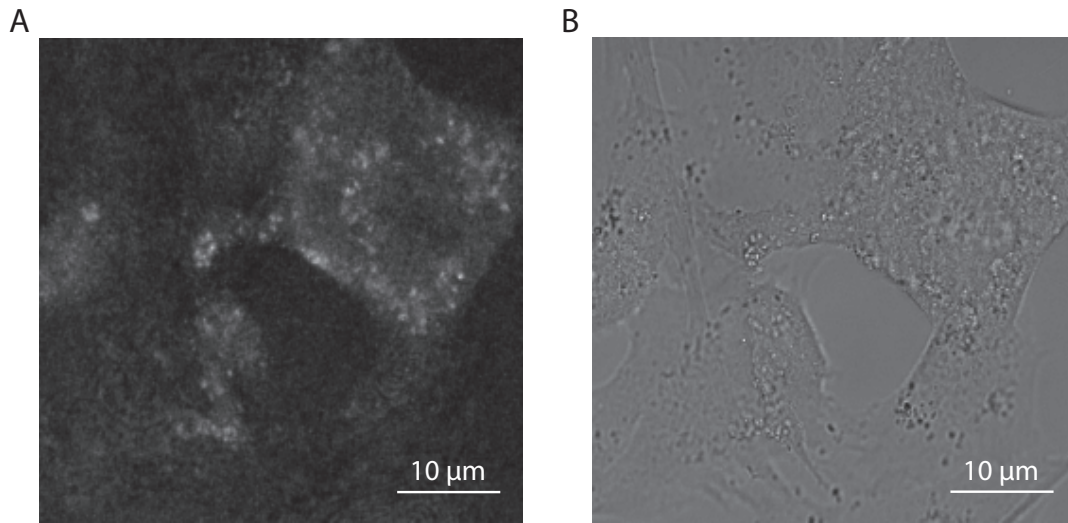
A

B

Figure 8.3: Expression of rapsyn-A25V-EYFP in undifferentiated C2C12 my-oblasts using a plasmid containing the native rapsyn promoter. A. Fluorescent confocal micrograph of rapsyn-A25V-EYFP with excitation at 514 nm. **B.** Transmission image.

The five different rapsyn constructs exhibited varied expression pattern. Wild-type rapsyn was expressed almost exclusively at the cell membrane and formed large and bright clusters (fig. 8.2A). Rapsyn-A25V was also expressed at the cell membrane but the endoplasmic reticulum was also highly fluorescent (fig. 8.2B). Rapsyn-N88K and R91L were expressed at the cell membrane but most of the fluorescence was cytosolic. L361R was expressed in the complete cell.

8.4.2 Rapsyn promoter-mediated expression in C2C12 myoblasts

Rapsyn-A25V-EYFP was expressed in C2C12 myoblasts using the extracted rapsyn promoter present in this mouse cell type. The observed fluorescence was very low. Among five different rapsyn derivatives subcloned in this plasmid, this protein was the only exhibiting detectable fluorescence level in C2C12 cells. There was a substantial fluorescence localized near the nucleus but very low level at the cell membrane (fig. 8.3).

8.4.3 Membrane calcium-ion sensing

Rapsyn-D3cpv was co-expressed with $5HT_3R$ in HEK 293 cells. The fluorescence was not only located at the cell membrane but also in the cytoplasm (fig. 8.4). Under the excitation of ECFP at 458 nm, the addition of 10 μ mCPBG, a $5HT_3R$ agonist, the fluorescence intensity of cpv increased, while the fluorescence intensity of CFP decreased. The donor-acceptor ratio exhibited a 32% decrease, indicating an increase of intracellular

calcium (fig. 8.4B). The same experiment has been performed with D2cpv without any visible change in ratio.
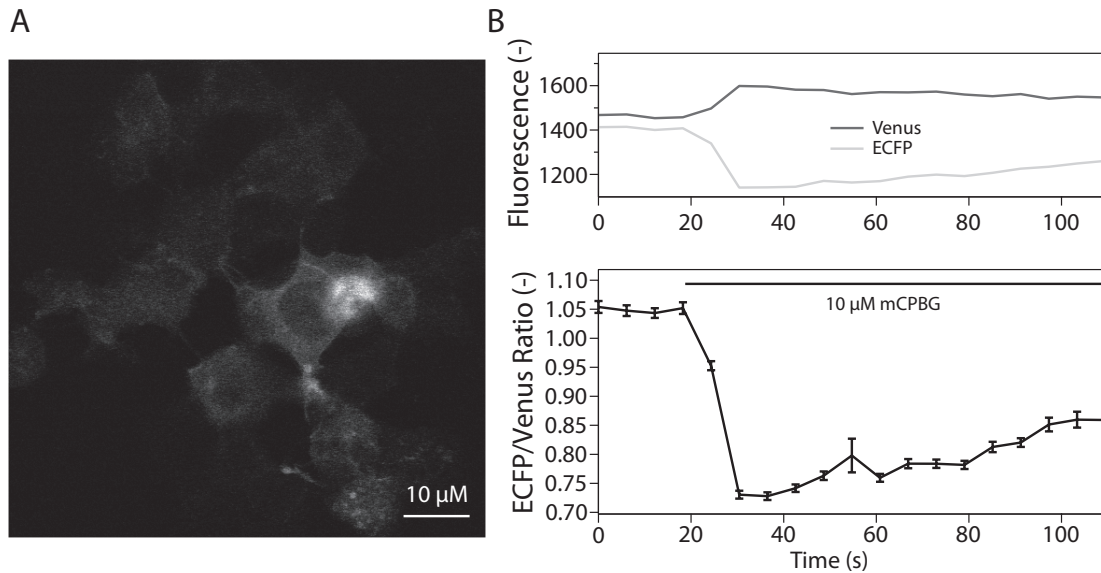
Figure 8.4: Rapsyn as a ratiometric calcium FRET sensor. A. Confocal micrographs of rapsyn-D3cpv construct co-expressed with 5HT$_3$R in HEK 293. **B.** Top panel shows fluorescence change in CFP and cpv (FRET) detection channels after addition of 10 μM of the 5HT$_3$R agonist mCPBG. Lower panel depicts the ratio of CFP/FRET channels. Confocal image was taken with a 458 nm laser excitation and the appropriates detection channels for CFP and cpv.

8.4.4 Photo-activatable proteins

Rapsyn-PA-EGFP, a photo-activatable derivative of rapsyn was expressed in HEK cells. The cellular localization observed was similar to the other fluorescent rapsyn derivatives. The photo-activatable fluorescent protein was functional (fig. 8.5), and could be activated using a 405 nm laser. A small activation by the 488 nm readout laser was observed during the measurement of fluorescence (fig. 8.5B and 8.5C).

8.5 Discussion

8.5.1 Dependence on cell type

HEK cells have been used as model cell for the study of fluorescent rapsyn derivatives. These cells are widely used in electrophysiology for their capacity to be easily transfected and the absence of expression of functional endogenous pLGIC. In HEK cells, wild-type

Figure 8.5: Photo-activation and measurments of rapsyn-PA-EGFP. A. Wide-field micrograph of rapsyn-PA-EGFP in HEK 293 cells. The four region of interests were used to measure the average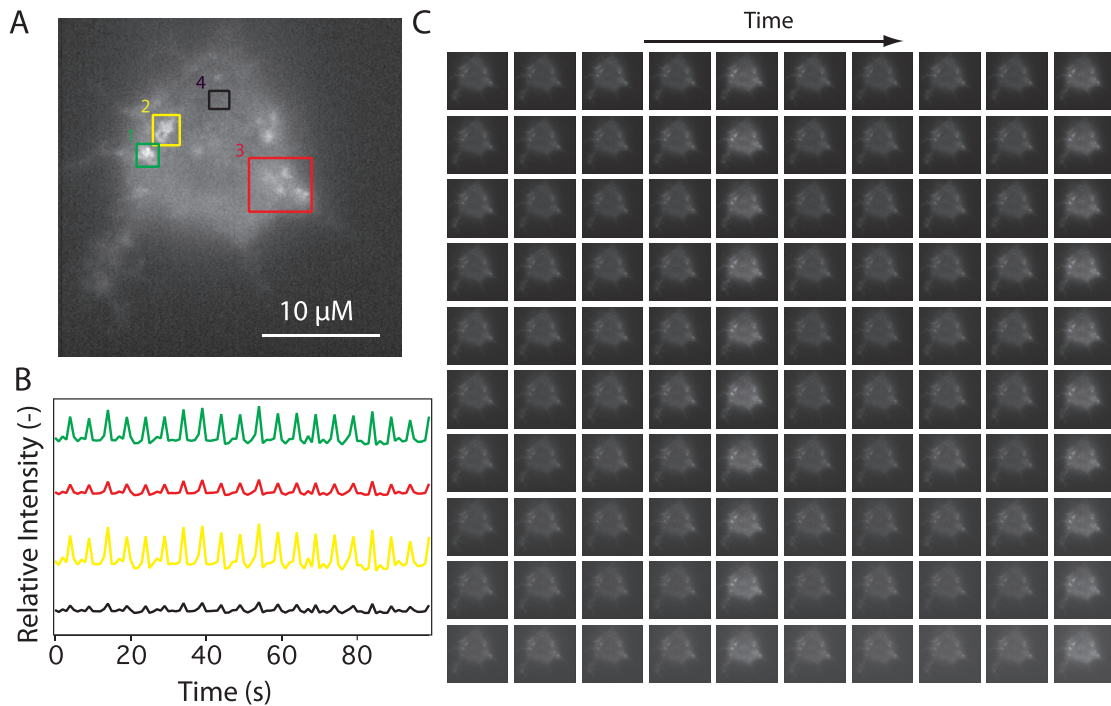 intensity shown in B. **B.** Average fluorescence intensity of the image during protein switching and readout cycles. After 4 images, a pulse of a 405 nm laser was made, this pulse was repeated every five images inducing increase of fluorescence intensity. This cycle was repeated 20 times. **C.** All the images of the cells expressing rapsyn-PA-EGFP during a measurement.

rapsyn form dense clusters comparable to those found in muscle cells (fig. 8.2A). HEK cells have been used to probe the rapsyn self-interaction and so far give reliable results, i.e. comparable in line with data obtained with muscle cells, for experiments on rapsyn.

Fluorescent rapsyn mutants have been imaged in C2C12 and R11 muscle cells. In these cell lines, the overexpression of rapsyn yielded strong accumulation in the ER (results not shown). The genetical engineering of a new vector for rapsyn expression in muscle using the genuine rapsyn promoter (described in section 8.3.1) was made to circumvent this ER accumulation issue. A fluorescent derivative of rapsyn A25V was weakly expressed using this vector (fig. 8.3) However, no relevant rapsyn expression images of the other mutants have been obtained with this vector.

8.5.2   Expression of mutant proteins

Expression of fluorescent derivatives of rapsyn mutants has given unexpected results. The mutants have the general tendency to exhibit a lower membrane expression than

the wild-type.

Rapsyn-A25V mutant is strongly retained in the ER, but is still expressed at the cell membrane (fig. 8.2B). As the mutant's binding site for nAChR should not be affected by the mutation, the defects on receptor clustering observed with this mutant could stem from either a low membrane expression of rapsyn, impairing proper cluster stabilization or by the retention of the receptor bound to rapsyn in the ER. These two hypothesis could also explain the low co-localization of rapsyn-A25V with nAChR at the cell membrane observed before [83].

Rapsyn-N88K is the most reported rapsyn mutant in patient suffering from congenital myasthenic syndromes [209]. The myasthenia of patient having only one allele with the N88K mutation were less severe than the patient with homzygous mutations. Fluorescent derivatives of rapsyn-N88K was localized in the cell cytosol with a very small fraction at the membrane (fig. 8.2C).

Fluorescent derivative of rapsyn-R91L had a cellular localization comparable to N88K (fig. 8.2D). This mutation is known to impair nAChR clustering. Our experiments did not show a clear difference between R91L and N88K mutants [83].

Fluorescent derivative of rapsyn-L361R was spread in the whole cell (fig. 8.2E). This spread was most likely due to protein clipping as the fluorescence distribution is comparable to CFP alone (data not shown).

Membrane anchoring with a myristoyl chain is weak; Alone it is not sufficient for membrane anchoring of protein [210]. Wild-type rapsyn forms very dense clusters of interacting proteins, which can be considered as oligomers. It is likely that with a strong rapsyn self-interaction, the anchoring is reinforced by the presence of more than one anchor by oligomer. When rapsyn self-interaction is impaired by mutations (like N88K and R91L) this synergistic effect could decrease.

Rapsyn self interaction can therefore has a double effect, densifying nAChR at the NMJ and maintaining the postsynaptic density at the membrane. This second effect would be increased by the interaction of rapsyn with nAChR.

8.5.3 FRET

All the fluorescent derivatives of rapsyn mutants were designed to measure rapsyn self-interaction by FRET. This experiment was made to be able to measure the effect of homo- and heterozygous mutations. Preliminary FRET measurements between different fluorescent derivatives of rapsyn mutants have shown a substantial effect of the mutations on the FRET efficiency and on the rapsyn oligomerization level (data not shown).

Further FRET experiments must be performed on R11 myoblasts, which do not express rapsyn. The use of the rapsyn promoter-mediated expression vector could maintain a physiological rapsyn level.

8.5.4   Calcium sensor and photo-activatable proteins

The calcium sensor and photo-activatables derivatives of rapsyn were genetically engineered for advance studies of the NMJ. The fonctionality of both proteins have been demonstrated and further experiments can readily be performed.

Rapsyn-D3cpv was shown to be functional, whereas the same experiments performed with rapsyn-D2cpv did not show sensor activity. Apparently D2cpv is not appropriated for measurements in living cells. Furthermore, repeated experiments using this sensor alone did not show any change upon calcium concentration changes (data not shown).

The D3cpv derivative was made to probe *in vitro* synapse formation and functionality in nerve muscle co-culture [211]. Up to now, NMJ formation in co-culture has not been observed with the sensor.

8.6   Conclusion

The fluorescent rapsyn derivatives shown in this chapter were designed to study different features of the neuromuscular junction. They can be used as tool for future studies on different aspects of the mouse neuromuscular junction. These proteins were all made for study in mouse cell lines but as human rapsyn is highly homologous, they can be readily use in human.

Summarizing conclusions and outlook

In this thesis, advanced fluorescence microscopy methods were developed and used to study the dynamics of nAChR and 5HT$_3$R, two pentameric ligand-gated ion-channels, and rapsyn, a scaffolding protein associated with nAChR in the post-synaptic membrane of the neuromuscular junction.

Single-molecule tracking has been used to investigate the dynamics and mobility of nAChR and 5HT$_3$R in the cellular plasma membrane. The measurement and analysis methods have been improved by several technical and computational means.

We have developed home-built softwares for the analysis of advanced microscopy experiments. One was dedicated to track single-molecules in the membrane of living cells. This time-consuming task has been rationalized to become faster and more reproducible. Different analysis procedures have been implemented for various single-molecule experiments. The second software was written to simplify the FRET microscopy data analysis while keeping the possibility to easily implement the available features. These software packages were designed to limit the *a priori* assumptions during data analysis.

An existing wide-field microscope setup was modified by installing, (i) lasers with additional excitation wavelengths and (ii) separated detection pathways. These modifications allowed multicolor fluorescence measurements and FRET detection in living cells. Furthermore, these features allowed to photo-activate fluorescent proteins for super-resolution microscopy.

Two labeling techniques were used and improved to track receptors in the cellular plasma membrane; the first used affinity tags and the second involved fluorescent derivatives of natural ligands. The length of the trajectories of fluorescent molecule involving fluorescent organic dyes and affinity labels was significantly increased by the combination of Atto647N, a very photostable dye, and the use of *tris*-NTA, a multivalent metal chela-

103

tor. The use of quantum dots has increased the duration of observing single-molecule traces by two order of magnitudes.

The dynamic of the native acetylcholine receptor was studied in muscle cells by single-molecule tracking. Receptors were labeled using quantum dots linked to α-bungarotoxin with a streptavidin-biotin linker. This technique has allowed to track the nAChR over a few thousand imaging frames, yielding new insight on the change of diffusion types of single receptor.

nAChR has been found almost always immobile in muscle cells. This is mainly due to its interaction with rapsyn, which has been demonstrated to strongly immobilize nAChR when both proteins are expressed heterologously in HEK 293 cells. However, we have found that receptor immobilization was not only due to rapsyn but also to a very efficient domain confinement.

The homo-pentameric $5HT_{3A}$ was used as a model to investigate the importance of the large intracellular loop shared by the majority of the mammals pLGIC. Astonishingly, successive deletions in the intracellular loop had a very small impact on the diffusion coefficient, whereas the type of motion experienced by the modified receptor changed significantly. This suggests the presence of localized binding sites for receptor associated proteins. Furthermore the removal of a defined region of the intracellular loop increased the $5HT_3R$ undergoing directed motion.

Single-molecule tracking of a prokaryotic pLGIC in mammalian cells yielded astonishing results. ELIC, natively expressed in a totally different organism interacts with the human cells in the same way as the $5HT_3R$. This suggests common trafficking pathway and similar recognition sequences. However, the lack of a large intracellular loop in ELIC could imply membrane associated dynamic processes.

A plasmid for the expression of rapsyn in muscle cell containing the native C2C12 rapsyn promoter was constructed to limit the expression of the artificial rapsyn derivative close to the natural expression level.

Fluorescent derivatives of rapsyn have been engineered by molecular biology for multiple application. Rapsyn has been used as a Swiss-army knife to analyze the neuromuscular junction. (i) The fusion of rapsyn with several fluorescent proteins was made to image the cellular localization of disease-related mutants and to measure rapsyn self-interactions by FRET. (ii) The fusion with a FRET-based calcium sensor was designed to probe the functionality of neuromuscular junction containing the different mutants. (iii) Rapsyn containing photoactivable or photoswitchable fluorescent protein were constructed to perform super-resolution FPALM microscopy on neuromuscular junction. These photoactive proteins could also be used to measure the dynamics of cellular trafficking.

Taken together, all these experiments, technical and computational developments were designed to measure dynamics of the functional neuromuscular junction in cul-

tured nerve and muscle cells forming neuromuscular junction. The combination of single receptor tracking and rapsyn as a marker of the shape, strength or functionality of the neuromuscular junction will give precious information on the synaptic function. Furthermore, it could decipher the effect of certain genetic myasthenia on the phenotype of the neuromuscular junction *in vitro*.

Abbreviation list

5HT$_3$R	5-hydroxyptamine type 3 receptor
AOTF	accousto-optic tunable filter
APD	avalanche photodiode
α-BgTx	α-bungarotoxin
CaM	calmodulin
CCD	charge-coupled device
CFP	cyan fluorescent protein
CMS	congenital myasthenic syndrom
CNS	central nervous system
α-CnTx-GI	α-conotoxin-GI
cpv	circularly permuted venus
D	diffusion coefficient
ECFP	enhanced cyan fluorescent protein
EGFP	enhanced green fluorescent protein
ELIC	*Eliobacter* ligand-gated ion channel
EMCCD	electron multiplying CCD
EYFP	enhanced yellow fluorescent protein
FBS	fetal bovine serum
FCS	fluorescence correlation spectroscopy
FP	fluorescent protein
FRAP	fluorescence recovery after photobleaching
FRET	Förster resonance energy transfer
GLIC	*Gloeobacter* ligand-gated ion-channel
HEK 293 T	human embryonic kidney cells
mCFP	monomeric cyan fluorescent protein
mGFP	monomeric green fluorescent protein
mCit	monomeric Citrine
MSD	mean square displacement
MSS	moment-scaling spectrum

MuSK	muscle-specific kinase
nAChR	nicotinic acetylcholine receptor
NHS	N-hydroxysuccinimide
NMJ	neuromuscular junction
NTA	nitrilotriacetic acid
PA-GFP	photoactivable green fluorescent protein
PALM	photoactivatation localization microscopy
pLGIC	pentameric ligand-gated ion channel
PMT	photomultiplier tube
PSD	postsynaptic density
PSF	point spread function
QD	quantum dot
ROI	region of interest
SNR	signal to noise ratio
SPT	single-particle tracking
SMM	single-molecule microscopy
t_{lag}	time lag between frames
TPR	tetratricopeptide repeats

Bibliography

[1] Danielli, J. and H. Davson. A contribution to the theory of permeability of thin films. *J Cell Compar Physl*, 5(4):495–508, 1935.

[2] Singer, S. J. and G. L. Nicolson. The fluid mosaic model of the structure of cell membranes. *Science*, 175(23):720–31, 1972.

[3] van Meer, G., D. R. Voelker, and G. W. Feigenson. Membrane lipids: where they are and how they behave. *Nat Rev Mol Cell Biol*, 9(2):112–24, 2008.

[4] Fadok, V. A., D. L. Bratton, D. M. Rose, A. Pearson, R. A. Ezekewitz, and P. M. Henson. A receptor for phosphatidylserine-specific clearance of apoptotic cells. *Nature*, 405(6782):85–90, 2000.

[5] Marchand, S., A. Devillers-Thiéry, S. Pons, J.-P. Changeux, and J. Cartaud. Rapsyn escorts the nicotinic acetylcholine receptor along the exocytic pathway via association with lipid rafts. *J Neurosci*, 22(20):8891–901, 2002.

[6] Edidin, M. Lipid microdomains in cell surface membranes. *Curr Opin Struct Biol*, 7(4):528–32, 1997.

[7] Kusumi, A. and Y. Sako. Cell surface organization by the membrane skeleton. *Curr Opin Cell Biol*, 8(4):566–74, 1996.

[8] Morone, N., T. K. Fujiwara, K. Murase, R. S. Kasai, H. Ike, S. Yuasa, J. Usukura, and A. Kusumi. Three-dimensional reconstruction of the membrane skeleton at the plasma membrane interface by electron tomography. *J Cell Biol*, 174(6):851–62, 2006.

[9] Kusumi, A., Y. M. Shirai, I. Koyama-Honda, K. G. N. Suzuki, and T. K. Fujiwara. Hierarchical organization of the plasma membrane: investigations by single-molecule tracking vs. fluorescence correlation spectroscopy. *FEBS Letters*, 584(9):1814–23, 2010.

[10] Simons, K. and E. Ikonen. Functional rafts in cell membranes. *Nature*, 387(6633):569–72, 1997.

[11] Edidin, M. Membrane cholesterol, protein phosphorylation, and lipid rafts. *Sci STKE*, 2001(67):pe1, 2001.

[12] Kusumi, A., C. Nakada, K. Ritchie, K. Murase, K. G. N. Suzuki, H. Murakoshi, R. S. Kasai, J. Kondo, and T. K. Fujiwara. Paradigm shift of the plasma membrane concept from the two-dimensional continuum fluid to the partitioned fluid: High-speed single-solecule tracking of membrane molecules. *Annu. Rev. Biophys. Biomol. Struct*, 34:351–378, 2005.

[13] Lingwood, D. and K. Simons. Lipid rafts as a membrane-organizing principle. *Science*, 327(5961):46–50, 2010.

[14] Specht, C. G. and A. Triller. The dynamics of synaptic scaffolds. *Bioessays*, 30(11-12):1062–74, 2008.

[15] Tasneem, A., L. M. Iyer, E. Jakobsson, and L. Aravind. Identification of the prokaryotic ligand-gated ion channels and their implications for the mechanisms and origins of animal Cys-loop ion channels. *Genome Biol*, 6(1):R4, 2005.

[16] Bocquet, N., L. P. de Carvalho, J. Cartaud, J. Neyton, C. L. Poupon, A. Taly, T. Grutter, J.-P. Changeux, and P.-J. Corringer. A prokaryotic proton-gated ion channel from the nicotinic acetylcholine receptor family. *Nature*, 445(7123):116–9, 2007.

[17] Unwin, N. Refined structure of the nicotinic acetylcholine receptor at 4Å resolution. *J Mol Biol*, 346(4):967–89, 2005.

[18] Corringer, P.-J., M. Baaden, N. Bocquet, M. Delarue, V. Dufresne, H. Nury, M. Prevost, and C. V. Renterghem. Atomic structure and dynamics of pentameric ligand-gated ion channels: new insight from bacterial homologues. *The Journal of Physiology*, 588(Pt 4):565–72, 2010.

[19] Hilf, R. J. C. and R. Dutzler. X-ray structure of a prokaryotic pentameric ligand-gated ion channel. *Nature*, page 6, 2008.

[20] Hilf, R. J. C. and R. Dutzler. Structure of a potentially open state of a proton-activated pentameric ligand-gated ion channel. *Nature*, page 5, 2008.

[21] Bocquet, N., H. Nury, M. Baaden, C. L. Poupon, J.-P. Changeux, M. Delarue, and P.-J. Corringer. X-ray structure of a pentameric ligand-gated ion channel in an apparently open conformation. *Nature*, page 4, 2008.

[22] Duclert, A. and J.-P. Changeux. Acetylcholine receptor gene expression at the developing neuromuscular junction. *Physiol Rev*, 75(2):339–68, 1995.

[23] Corringer, P. J., N. L. Novère, and J.-P. Changeux. Nicotinic receptors at the amino acid level. *Annu Rev Pharmacol Toxicol*, 40:431–58, 2000.

[24] Bouzat, C., N. Bren, and S. M. Sine. Structural basis of the different gating kinetics of fetal and adult acetylcholine receptors. *Neuron*, 13(6):1395–402, 1994.

[25] Unwin, N. Nicotinic acetylcholine receptor at 9 Åresolution. *J Mol Biol*, 229(4):1101–24, 1993.

[26] Karlin, A. Emerging structure of the nicotinic acetylcholine receptors. *Nat Rev Neurosci*, 3(2):102–14, 2002.

[27] Brejc, K., W. J. van Dijk, R. V. Klaassen, M. Schuurmans, J. van Der Oost, A. B. Smit, and T. K. Sixma. Crystal structure of an ACh-binding protein reveals the ligand-binding domain of nicotinic receptors. *Nature*, 411(6835):269–76, 2001.

[28] Hansen, S. B., T. T. Talley, Z. Radic, and P. Taylor. Structural and ligand recognition characteristics of an acetylcholine-binding protein from Aplysia californica. *J Biol Chem*, 279(23):24197–202, 2004.

[29] Castillo, J. D. and B. Katz. Interaction at end-plate receptors between different choline derivatives. *Proc R Soc Lond, B, Biol Sci*, 146(924):369–81, 1957.

[30] Prinz, H. and A. Maelicke. Ligand binding to the membrane-bound acetylcholine receptor from Torpedo marmorata: a complete mathematical analysis. *Biochemistry*, 31(29):6728–38, 1992.

[31] Daly, J. W. Nicotinic agonists, antagonists, and modulators from natural sources. *Cell Mol Neurobiol*, 25(3-4):513–52, 2005.

[32] Holbrook, J. D., C. H. Gill, N. Zebda, J. P. Spencer, R. Leyland, K. H. Rance, H. Trinh, G. Balmer, F. M. Kelly, S. P. Yusaf, N. Courtenay, J. Luck, A. Rhodes, S. Modha, S. E. Moore, G. J. Sanger, and M. J. Gunthorpe. Characterisation of 5-HT3C, 5-HT3D and 5-HT3E receptor subunits: evolution, distribution and function. *J Neurochem*, 108(2):384–96, 2009.

[33] Niesler, B., B. Frank, J. Kapeller, and G. A. Rappold. Cloning, physical mapping and expression analysis of the human 5-HT3 serotonin receptor-like genes HTR3C, HTR3D and HTR3E. *Gene*, 310:101–11, 2003.

[34] Walstab, J., C. Hammer, F. Lasitschka, D. Moeller, C. N. Connolly, G. Rappold, M. Bruss, H. Bonisch, and B. Niesler. RIC-3 exclusively enhances the surface

expression of human homomeric 5-hydroxytryptamine type 3A (5-HT3A) receptors, despite direct interactions with 5-HT3A, C, D and E subunits. *Journal of Biological Chemistry*, pages 1–20, 2010.

[35] Alberts, B., A. Johnson, J. Lewis, M. Raff, K. Roberts, and P. Walter. *Molecular Biology of the Cell* (Garland Science), fourth edition, 2002.

[36] Lodish, H., A. Berk, P. Matsudaira, C. A. Kaiser, M. Krieger, M. P. Scott, L. Zipursky, and J. Darnell. *Molecular Cell Biology* (W. H. Freeman), third edition, 2003.

[37] Sanes, J. R. and J. W. Lichtman. Development of the vertebrate neuromuscular junction. *Annu Rev Neurosci*, 22:389–442, 1999.

[38] Akaaboune, M., S. M. Culican, S. G. Turney, and J. W. Lichtman. Rapid and reversible effects of activity on acetylcholine receptor density at the neuromuscular junction in vivo. *Science*, 286(5439):503–7, 1999.

[39] Kummer, T. T., T. Misgeld, J. W. Lichtman, and J. R. Sanes. Nerve-independent formation of a topologically complex postsynaptic apparatus. *J Cell Biol*, 164(7):1077–87, 2004.

[40] Gajsek, N., M. Jevsek, T. Mars, K. Mis, S. Pirkmajer, J. Brecelj, and Z. Grubic. Synaptogenetic mechanisms controlling postsynaptic differentiation of the neuromuscular junction are nerve-dependent in human and nerve-independent in mouse C2C12 muscle cultures. *Chem Biol Interact*, 2008.

[41] Hughes, B. W., L. L. Kusner, and H. J. Kaminski. Molecular architecture of the neuromuscular junction. *Muscle Nerve*, 33(4):445–61, 2006.

[42] Zhang, B., S.-W. Luo, Q. Wang, T. Suzuki, W.-C. Xiong, and L. Mei. LRP4 serves as a coreceptor of agrin. *Neuron*, 60(2):285–97, 2008.

[43] Kim, N., A. L. Stiegler, T. O. Cameron, P. T. Hallock, A. M. Gomez, J. H. Huang, S. R. Hubbard, M. L. Dustin, and S. J. Burden. Lrp4 is a receptor for Agrin and forms a complex with MuSK. *Cell*, 135(2):334–42, 2008.

[44] Antolik, C., D. H. Catino, W. G. Resneck, and R. J. Bloch. The tetratricopeptide repeat domains of rapsyn bind directly to cytoplasmic sequences of the muscle-specific kinase. *Neuroscience*, 141(1):87–100, 2006.

[45] Sadasivam, G., R. Willmann, S. Lin, S. Erb-Vögtli, X. C. Kong, M. A. Rüegg, and C. Fuhrer. Src-family kinases stabilize the neuromuscular synapse in vivo via protein interactions, phosphorylation, and cytoskeletal linkage of acetylcholine receptors. *J Neurosci*, 25(45):10479–93, 2005.

[46] Linnoila, J., Y. Wang, Y. Yao, and Z.-Z. Wang. A mammalian homolog of Drosophila tumorous imaginal discs, Tid1, mediates agrin signaling at the neuromuscular junction. *Neuron*, 60(4):625–41, 2008.

[47] Finn, A. J., G. Feng, and A. M. Pendergast. Postsynaptic requirement for Abl kinases in assembly of the neuromuscular junction. *Nat Neurosci*, 6(7):717–23, 2003.

[48] Henriquez, J., A. Webb, M. Bence, H. Bildsoe, M. Sahores, S. Hughes, and P. Salinas. Wnt signaling promotes AChR aggregation at the neuromuscular synapse in collaboration with agrin. *Proc Natl Acad Sci USA*, 2008.

[49] Wang, J., N.-J. Ruan, L. Qian, W.-L. Lei, F. Chen, and Z.-G. Luo. Wnt/beta-Catenin Signaling Suppresses Rapsyn Expression and Inhibits Acetylcholine Receptor Clustering at the Neuromuscular Junction. *J Biol Chem*, 283(31):21668–75, 2008.

[50] Falls, D. L. Neuregulins and the neuromuscular system: 10 years of answers and questions. *J Neurocytol*, 32(5-8):619–47, 2003.

[51] Li, Q., R. M. Esper, and J. A. Loeb. Synergistic effects of neuregulin and agrin on muscle acetylcholine receptor expression. *Mol Cell Neurosci*, 26(4):558–69, 2004.

[52] Bruneau, E. G., J. A. Esteban, and M. Akaaboune. Receptor-associated proteins and synaptic plasticity. *FASEB J*, 23(3):679–88, 2009.

[53] Willmann, R. and C. Fuhrer. Neuromuscular synaptogenesis: clustering of acetylcholine receptors revisited. *Cell Mol Life Sci*, 59(8):1296–316, 2002.

[54] Luo, S.-W., B. Zhang, X.-P. Dong, Y. Tao, A. K. L. Ting, Z. Zhou, J. Meixiong, J. Luo, F. C. A. Chiu, W.-C. Xiong, and L. Mei. HSP90beta regulates rapsyn turnover and subsequent AChR cluster formation and maintenance. *Neuron*, 60(1):97–110, 2008.

[55] Strochlic, L., A. Cartaud, and J. Cartaud. The synaptic muscle-specific kinase (MuSK) complex: new partners, new functions. *Bioessays*, 27(11):1129–35, 2005.

[56] Luo, Z., Q. Wang, G. C. Dobbins, S. Levy, W.-C. Xiong, and L. Mei. Signaling complexes for postsynaptic differentiation. *J Neurocytol*, 32(5-8):697–708, 2003.

[57] Allen, J. A., R. A. Halverson-Tamboli, and M. M. Rasenick. Lipid raft microdomains and neurotransmitter signalling. *Nat Rev Neurosci*, 8(2):128–40, 2007.

[58] Barrantes, F. J., V. Bermudez, M. V. Borroni, S. S. Antollini, M. F. Pediconi, J. C. Baier, I. Bonini, C. Gallegos, A. M. Roccamo, A. S. Valles, V. Ayala, and

C. Kamerbeek. Boundary lipids in the nicotinic acetylcholine receptor microenvironment. *J Mol Neurosci*, 40(1-2):87–90, 2010.

[59] Zhu, D., W.-C. Xiong, and L. Mei. Lipid rafts serve as a signaling platform for nicotinic acetylcholine receptor clustering. *J Neurosci*, 26(18):4841–51, 2006.

[60] Willmann, R., S. Pun, L. Stallmach, G. Sadasivam, A. F. Santos, P. Caroni, and C. Fuhrer. Cholesterol and lipid microdomains stabilize the postsynapse at the neuromuscular junction. *EMBO J*, 25(17):4050–60, 2006.

[61] Roccamo, A. M., M. F. Pediconi, E. Aztiria, L. Zanello, A. Wolstenholme, and F. J. Barrantes. Cells defective in sphingolipids biosynthesis express low amounts of muscle nicotinic acetylcholine receptor. *Eur J Neurosci*, 11(5):1615–23, 1999.

[62] Pediconi, M. F., C. E. Gallegos, E. B. D. L. Santos, and F. J. Barrantes. Metabolic cholesterol depletion hinders cell-surface trafficking of the nicotinic acetylcholine receptor. *Neuroscience*, 128(2):239–49, 2004.

[63] Pato, C., F. Stetzkowski-Marden, K. Gaus, M. Recouvreur, A. Cartaud, and J. Cartaud. Role of lipid rafts in agrin-elicited acetylcholine receptor clustering. *Chem Biol Interact*, 175(1-3):64–7, 2008.

[64] Baier, C. J., C. E. Gallegos, V. Levi, and F. J. Barrantes. Cholesterol modulation of nicotinic acetylcholine receptor surface mobility. *Eur Biophys J*, 39(2):213–27, 2010.

[65] Froehner, S. C., V. Gulbrandsen, C. Hyman, A. Y. Jeng, R. R. Neubig, and J. B. Cohen. Immunofluorescence localization at the mammalian neuromuscular junction of the Mr 43,000 protein of Torpedo postsynaptic membranes. *Proc Natl Acad Sci USA*, 78(8):5230–4, 1981.

[66] Frail, D. E., L. S. Musil, A. Buonanno, and J. P. Merlie. Expression of RAPsyn (43K protein) and nicotinic acetylcholine receptor genes is not coordinately regulated in mouse muscle. *Neuron*, 2(1):1077–86, 1989.

[67] Marchand, S., F. Bignami, F. Stetzkowski-Marden, and J. Cartaud. The myristoylated protein rapsyn is cotargeted with the nicotinic acetylcholine receptor to the postsynaptic membrane via the exocytic pathway. *J Neurosci*, 20(2):521–8, 2000.

[68] Ramarao, M. K., M. J. Bianchetta, J. Lanken, and J. B. Cohen. Role of rapsyn tetratricopeptide repeat and coiled-coil domains in self-association and nicotinic acetylcholine receptor clustering. *J Biol Chem*, 276(10):7475–83, 2001.

[69] Ramarao, M. K. and J. B. Cohen. Mechanism of nicotinic acetylcholine receptor cluster formation by rapsyn. *Proc Natl Acad Sci USA*, 95(7):4007–12, 1998.

[70] Margaret M Maimone, e. a., M. M. and R. E. Enigk. The intracellular domain of the nicotinic acetylcholine receptor alpha subunit mediates its coclustering with rapsyn. *Mol Cell Neurosci*, 14(4-5):340–54, 1999.

[71] Huebsch, K. A. and M. M. Margaret M Maimone. Rapsyn-mediated clustering of acetylcholine receptor subunits requires the major cytoplasmic loop of the receptor subunits. *J Neurobiol*, 54(3):486–501, 2003.

[72] Borges, L. S., S. Yechikhov, Y. I. Lee, J. B. Rudell, M. B. Friese, S. J. Burden, and M. J. Ferns. Identification of a motif in the acetylcholine receptor beta subunit whose phosphorylation regulates rapsyn association and postsynaptic receptor localization. *J Neurosci*, 28(45):11468–76, 2008.

[73] Lee, Y., J. Rudell, and M. Ferns. Rapsyn interacts with the muscle acetylcholine receptor via alpha-helical domains in the alpha, beta, and epsilon subunit intracellular loops. *Neuroscience*, 163(1):222–32, 2009.

[74] Bartoli, M., M. K. Ramarao, and J. B. Cohen. Interactions of the rapsyn RING-H2 domain with dystroglycan. *J Biol Chem*, 276(27):24911–7, 2001.

[75] Antolik, C., D. H. Catino, A. M. O'Neill, W. G. Resneck, J. A. Ursitti, and R. J. Bloch. The actin binding domain of ACF7 binds directly to the tetratricopeptide repeat domains of rapsyn. *Neuroscience*, 145(1):56–65, 2007.

[76] Dobbins, G. C., S. Luo, Z. Yang, W. C. Xiong, and L. Mei. alpha-Actinin interacts with rapsyn in agrin-stimulated AChR clustering. *Molecular brain*, 1(1):18, 2008.

[77] Chen, F., L. Qian, Z.-H. Yang, Y. Huang, S. T. Ngo, N.-J. Ruan, J. Wang, C. Schneider, P. G. Noakes, Y.-Q. Ding, L. Mei, and Z.-G. Luo. Rapsyn interaction with calpain stabilizes AChR clusters at the neuromuscular junction. *Neuron*, 55(2):247–60, 2007.

[78] Hanna, R. A., R. L. Campbell, and P. L. Davies. Calcium-bound structure of calpain and its mechanism of inhibition by calpastatin. *Nature*, 456(7220):409–12, 2008.

[79] Wang, J., Z. Jing, L. Zhang, G. Zhou, J. Braun, Y. Yao, and Z.-Z. Wang. Regulation of acetylcholine receptor clustering by the tumor suppressor APC. *Nat Neurosci*, 6(10):1017–8, 2003.

[80] Bruneau, E. G. and M. Akaaboune. The dynamics of the rapsyn scaffolding protein at individual acetylcholine receptor clusters. *J Biol Chem*, 282(13):9932–40, 2007.

[81] Beeson, D., R. Webster, J. Cossins, D. Lashley, H. Spearman, S. Maxwell, C. R. Slater, J. Newsom-Davis, J. Palace, and A. Vincent. Congenital myasthenic syndromes and the formation of the neuromuscular junction. *Ann N Y Acad Sci*, 1132:99–103, 2008.

[82] Engel, A. G. and S. M. Sine. Current understanding of congenital myasthenic syndromes. *Current opinion in pharmacology*, 5(3):308–21, 2005.

[83] Cossins, J., G. Burke, S. Maxwell, H. Spearman, S. Man, J. Kuks, A. Vincent, J. Palace, C. Fuhrer, and D. Beeson. Diverse molecular mechanisms involved in AChR deficiency due to rapsyn mutations. *Brain*, 129(Pt 10):2773–83, 2006.

[84] Müller, J. S., S. K. Baumeister, U. Schara, J. Cossins, S. Krause, M. von der Hagen, A. Huebner, R. Webster, D. Beeson, H. Lochmüller, and A. Abicht. CHRND mutation causes a congenital myasthenic syndrome by impairing co-clustering of the acetylcholine receptor with rapsyn. *Brain*, 129(Pt 10):2784–93, 2006.

[85] Saffman, P. G. and M. Delbrück. Brownian motion in biological membranes. *Proc Natl Acad Sci USA*, 72(8):3111–3, 1975.

[86] Schütz, G. J., H. Schindler, and T. Schmidt. Single-molecule microscopy on model membranes reveals anomalous diffusion. *Biophys J*, 73(2):1073–80, 1997.

[87] Jacobson, K., A. Ishihara, and R. Inman. Lateral diffusion of proteins in membranes. *Annu Rev Physiol*, 49:163–75, 1987.

[88] Simson, R., B. Yang, S. E. Moore, P. Doherty, F. S. Walsh, and K. Jacobson. Structural mosaicism on the submicron scale in the plasma membrane. *Biophys J*, 74(1):297–308, 1998.

[89] Geerts, H., M. D. Brabander, R. Nuydens, S. Geuens, M. Moeremans, J. D. Mey, and P. Hollenbeck. Nanovid tracking: a new automatic method for the study of mobility in living cells based on colloidal gold and video microscopy. *Biophys J*, 52(5):775–82, 1987.

[90] Brabander, M. D., R. Nuydens, A. Ishihara, B. Holifield, K. Jacobson, and H. Geerts. Lateral diffusion and retrograde movements of individual cell surface components on single motile cells observed with Nanovid microscopy. *J Cell Biol*, 112(1):111–24, 1991.

[91] Kusumi, A., Y. Sako, and M. Yamamoto. Confined lateral diffusion of membrane receptors as studied by single particle tracking (nanovid microscopy). Effects of calcium-induced differentiation in cultured epithelial cells. *Biophys J*, 65(5):2021–40, 1993.

[92] Anderson, C. M., G. N. Georgiou, I. E. Morrison, G. V. Stevenson, and R. J. Cherry. Tracking of cell surface receptors by fluorescence digital imaging microscopy using a charge-coupled device camera. Low-density lipoprotein and influenza virus receptor mobility at 4 degrees C. *J Cell Sci*, 101 (Pt 2):415–25, 1992.

[93] Schmidt, T., G. J. Schütz, W. Baumgartner, H. J. Gruber, and H. Schindler. Characterization of Photophysics and Mobility of Single Molecules in a Fluid Lipid Membrane. *Journal of Physical Chemistry*, 99:17662–17668, 1995.

[94] Sako, Y. Imaging single molecules in living cells for systems biology. *Mol Syst Biol*, 2:56, 2006.

[95] Iino, R. and A. Kusumi. Single-Fluorophore Dynamic Imaging in Living Cells. *Journal of Fluorescence*, 11(3):187–195, 2001.

[96] Lord, S. J., H. lu D Lee, and W. E. Moerner. Single-molecule spectroscopy and imaging of biomolecules in living cells. *Anal Chem*, 82(6):2192–203, 2010.

[97] Alcor, D., G. Gouzer, and A. Triller. Single-particle tracking methods for the study of membrane receptors dynamics. *Eur J Neurosci*, 30(6):987–97, 2009.

[98] Guddat, L. W., J. A. Martin, L. Shan, A. B. Edmundson, and W. R. Gray. Three-dimensional structure of the alpha-conotoxin GI at 1.2 A resolution. *Biochemistry*, 35(35):11329–35, 1996.

[99] Zhang, J., R. E. Campbell, A. Y. Ting, and R. Y. Tsien. Creating new fluorescent probes for cell biology. *Nat Rev Mol Cell Biol*, 3(12):906–18, 2002.

[100] Lata, S., M. Gavutis, R. Tampé, and J. Piehler. Specific and stable fluorescence labeling of histidine-tagged proteins for dissecting multi-protein complex formation. *J Am Chem Soc*, 128(7):2365–72, 2006.

[101] Anderson, M. J. and M. W. Cohen. Fluorescent staining of acetylcholine receptors in vertebrate skeletal muscle. *The Journal of Physiology*, 237(2):385–400, 1974.

[102] Daly, J. W. Nicotinic agonists, antagonists, and modulators from natural sources. *Cell Mol Neurobiol*, 25(3-4):513–52, 2005.

[103] Janes, R. W. alpha-Conotoxins as selective probes for nicotinic acetylcholine receptor subclasses. *Current opinion in pharmacology*, 5(3):280–92, 2005.

[104] Schreiter, C. *Electrophysiology And Fluorescence Microscopy Of Ligand-Gated Ion Channels*. Ph.D. thesis, EPFL, 2006.

[105] Schreiter, C., M. Gjoni, R. Hovius, K. L. Martinez, J.-M. Segura, and H. Vogel. Reversible sequential-binding probe receptor-ligand interactions in single cells. *Chembiochem*, 6(12):2187–94, 2005.

[106] Grandl, J., E. Sakr, F. Kotzyba-Hibert, F. Krieger, S. Bertrand, D. Bertrand, H. Vogel, M. Goeldner, and R. Hovius. Fluorescent epibatidine agonists for neuronal and muscle-type nicotinic acetylcholine receptors. *Angew Chem Int Ed Engl*, 46(19):3505–8, 2007.

[107] Yano, Y. and K. Matsuzaki. Tag-probe labeling methods for live-cell imaging of membrane proteins. *Biochim Biophys Acta*, 1788(10):2124–31, 2009.

[108] Guignet, E. G., R. Hovius, and H. Vogel. Reversible site-selective labeling of membrane proteins in live cells. *Nat Biotechnol*, 22(4):440–4, 2004.

[109] Lata, S., A. Reichel, R. Brock, R. Tampé, and J. Piehler. High-affinity adaptors for switchable recognition of histidine-tagged proteins. *J Am Chem Soc*, 127(29):10205–15, 2005.

[110] Roy, R., S. Hohng, and T. Ha. A practical guide to single-molecule FRET. *Nat Methods*, 5(6):507–16, 2008.

[111] Vogelsang, J., R. Kasper, C. Steinhauer, B. Person, M. Heilemann, M. Sauer, and P. Tinnefeld. A reducing and oxidizing system minimizes photobleaching and blinking of fluorescent dyes. *Angew Chem Int Ed Engl*, 47(29):5465–9, 2008.

[112] Michalet, X., F. Pinaud, T. D. Lacoste, M. Dahan, M. P. Bruchez, A. P. Alivisatos, and S. Weiss. Properties of Fluorescent Semiconductor Nanocrystals and their Application to Biological Labeling. *Single Molecule*, 2(4):261–276, 2001.

[113] Chan, W. C. W., D. J. Maxwell, X. Gao, R. E. Bailey, M. Han, and S. Nie. Luminescent quantum dots for multiplexed biological detection and imaging. *Curr Opin Biotechnol*, 13(1):40–6, 2002.

[114] Geissbuehler, I., R. Hovius, K. L. Martinez, M. Adrian, K. R. Thampi, and H. Vogel. Lipid-coated nanocrystals as multifunctionalized luminescent scaffolds for supramolecular biological assemblies. *Angew Chem Int Ed Engl*, 44(9):1388–92, 2005.

[115] Roullier, V., S. Clarke, C. You, F. Pinaud, G. Gouzer, D. Schaible, V. Marchi-Artzner, J. Piehler, and M. Dahan. High-Affinity Labeling and Tracking of Individual Histidine-Tagged Proteins in Live Cells Using Ni^{2+} Tris-nitrilotriacetic Acid Quantum Dot Conjugates. *Nano Letters*, 2009.

[116] Bäumle, M., D. Stamou, J.-M. Segura, R. Hovius, and H. Vogel. Highly fluorescent streptavidin-coated CdSe nanoparticles: preparation in water, characterization, and micropatterning. *Langmuir*, 20(10):3828–31, 2004.

[117] Howarth, M., W. Liu, S. Puthenveetil, Y. Zheng, L. F. Marshall, M. M. Schmidt, K. D. Wittrup, M. G. Bawendi, and A. Y. Ting. Monovalent, reduced-size quantum dots for imaging receptors on living cells. *Nat Methods*, 5(5):397–9, 2008.

[118] Pinaud, F., X. Michalet, L. A. Bentolila, J. M. Tsay, S. Doose, J. J. Li, G. Iyer, and S. Weiss. Advances in fluorescence imaging with quantum dot bio-probes. *Biomaterials*, 27(9):1679–87, 2006.

[119] Pinaud, F., S. Clarke, A. Sittner, and M. Dahan. Probing cellular events, one quantum dot at a time. *Nat Methods*, 7(4):275–85, 2010.

[120] Osman, A. A., A. D. Schrader, A. J. Hawkes, O. Akil, A. Bergeron, L. R. Lustig, and D. D. Simmons. Muscle-like nicotinic receptor accessory molecules in sensory hair cells of the inner ear. *Mol Cell Neurosci*, 38(2):153–69, 2008.

[121] Webb, R. H. Theoretical basis of confocal microscopy. *Meth Enzymol*, 307:3–20, 1999.

[122] Joo, C., H. Balci, Y. Ishitsuka, C. Buranachai, and T. Ha. Advances in Single-Molecule Fluorescence Methods for Molecular Biology. *Annu Rev Biochem*, 2008.

[123] Groves, J. T., R. Parthasarathy, and M. B. Forstner. Fluorescence imaging of membrane dynamics. *Annu Rev Biomed Eng*, 10:311–38, 2008.

[124] Eggeling, C., C. Ringemann, R. Medda, G. Schwarzmann, K. Sandhoff, S. Polyakova, V. Belov, B. Hein, C. von Middendorff, A. Schönle, and S. Hell. Direct observation of the nanoscale dynamics of membrane lipids in a living cell. *Nature*, 2008.

[125] Hess, S. T., T. J. Gould, M. Gunewardene, J. Bewersdorf, and M. D. Mason. Ultrahigh resolution imaging of biomolecules by fluorescence photoactivation localization microscopy. *Methods Mol Biol*, 544:483–522, 2009.

[126] Cheezum, M. K., W. F. Walker, and W. H. Guilford. Quantitative comparison of algorithms for tracking single fluorescent particles. *Biophys J*, 81(4):2378–88, 2001.

[127] Hecht, E. *Optics* (Addison Wesley), fourth edition, 2002.

[128] Ober, R. J., S. Ram, and E. S. Ward. Localization accuracy in single-molecule microscopy. *Biophys J*, 86(2):1185–200, 2004.

[129] Saxton, M. J. and K. Jacobson. Single-particle tracking: applications to membrane dynamics. *Annual review of biophysics and biomolecular structure*, 26:373–99, 1997.

[130] Schwille, P., J. Korlach, and W. W. Webb. Fluorescence correlation spectroscopy with single-molecule sensitivity on cell and model membranes. *Cytometry*, 36(3):176–82, 1999.

[131] Ewers, H., A. E. Smith, I. F. Sbalzarini, H. Lilie, P. Koumoutsakos, and A. Helenius. Single-particle tracking of murine polyoma virus-like particles on live cells and artificial membranes. *Proc Natl Acad Sci USA*, 102(42):15110–5, 2005.

[132] Lommerse, P. H. M., G. A. Blab, L. Cognet, G. S. Harms, B. E. Snaar-Jagalska, H. P. Spaink, and T. Schmidt. Single-molecule imaging of the H-ras membrane-anchor reveals domains in the cytoplasmic leaflet of the cell membrane. *Biophys J*, 86(1 Pt 1):609–16, 2004.

[133] Banks, D. S. and C. Fradin. Anomalous diffusion of proteins due to molecular crowding. *Biophys J*, 89(5):2960–71, 2005.

[134] Ghosh, R. N. and W. W. Webb. Automated detection and tracking of individual and clustered cell surface low density lipoprotein receptor molecules. *Biophys J*, 66(5):1301–18, 1994.

[135] Saxton, M. J. Single-particle tracking: connecting the dots. *Nat Methods*, 5(8):671–2, 2008.

[136] Jaqaman, K., D. Loerke, M. Mettlen, H. Kuwata, S. Grinstein, S. L. Schmid, and G. Danuser. Robust single-particle tracking in live-cell time-lapse sequences. *Nat Methods*, 5(8):695–702, 2008.

[137] Sergé, A., N. Bertaux, H. Rigneault, and D. Marguet. Dynamic multiple-target tracing to probe spatiotemporal cartography of cell membranes. *Nat Methods*, 5(8):687–94, 2008.

[138] Harms, G. S., L. Cognet, P. H. M. Lommerse, G. A. Blab, H. Kahr, R. Gamsjäger, H. P. Spaink, N. M. Soldatov, C. Romanin, and T. Schmidt. Single-molecule imaging of l-type Ca^{2+} channels in live cells. *Biophys J*, 81(5):2639–46, 2001.

[139] Edidin, M. A., S. C. Kuo, and M. P. Sheetz. Lateral movements of membrane glycoproteins restricted by dynamic cytoplasmic barriers. *Science*, 254(5036):1379–82, 1991.

[140] Fujiwara, T. K., K. Ritchie, H. Murakoshi, K. Jacobson, and A. Kusumi. Phospholipids undergo hop diffusion in compartmentalized cell membrane. *J Cell Biol*, 157(6):1071–81, 2002.

[141] Lakowicz, J. R. *Principles of Fluorescence Spectroscopy* (Springer), 2006.

[142] Mielczarek, E. V., E. S. Greenbaum, R. S. Knox, and R. S. Knox. *Biological Physics.* Key Papers in Physics (American Institute of Physics), 1993.

[143] Meer, B. V. D., G. Coker, and S.-Y. S. Chen. *Resonance Energy Transfer Theory and Data* (VCH Publishers Inc), 1994.

[144] Meyer, B. H., J.-M. Segura, K. L. Martinez, R. Hovius, N. George, K. Johnsson, and H. Vogel. FRET imaging reveals that functional neurokinin-1 receptors are monomeric and reside in membrane microdomains of live cells. *Proc Natl Acad Sci USA*, 103(7):2138–43, 2006.

[145] Berney, C. and G. Danuser. FRET or no FRET: a quantitative comparison. *Biophys J*, 84(6):3992–4010, 2003.

[146] Abankwa, D. and H. Vogel. A FRET map of membrane anchors suggests distinct microdomains of heterotrimeric G proteins. *J Cell Sci*, 120(Pt 16):2953–62, 2007.

[147] Miyawaki, A., J. Llopis, R. Heim, J. M. McCaffery, J. A. Adams, M. Ikura, and R. Y. Tsien. Fluorescent indicators for Ca^{2+} based on green fluorescent proteins and calmodulin. *Nature*, 388(6645):882–7, 1997.

[148] Erickson, M. G., B. A. Alseikhan, B. Z. Peterson, and D. T. Yue. Preassociation of calmodulin with voltage-gated Ca(2+) channels revealed by FRET in single living cells. *Neuron*, 31(6):973–85, 2001.

[149] Ai, H.-W., K. L. Hazelwood, M. W. Davidson, and R. E. Campbell. Fluorescent protein FRET pairs for ratiometric imaging of dual biosensors. *Nat Methods*, 5(5):401–3, 2008.

[150] Feige, J. N., D. Sage, W. Wahli, B. Desvergne, and L. Gelman. PixFRET, an ImageJ plug-in for FRET calculation that can accommodate variations in spectral bleed-throughs. *Microsc Res Tech*, 68(1):51–8, 2005.

[151] Bromann, P. A., H. Zhou, and J. R. Sanes. Kinase- and rapsyn-independent activities of the muscle-specific kinase (MuSK). *Neuroscience*, 125(2):417–26, 2004.

[152] Frail, D. E., L. L. McLaughlin, J. Mudd, and J. P. Merlie. Identification of the mouse muscle 43,000-dalton acetylcholine receptor-associated protein (RAPsyn) by cDNA cloning. *J Biol Chem*, 263(30):15602–7, 1988.

[153] Sanes, J. R. and J. W. Lichtman. Induction, assembly, maturation and maintenance of a postsynaptic apparatus. *Nat Rev Neurosci*, 2(11):791–805, 2001.

[154] Burden, S. J. The subsynaptic 43-kDa protein is concentrated at developing nerve-muscle synapses in vitro. *Proc Natl Acad Sci USA*, 82(23):8270–3, 1985.

[155] Kummer, T. T., T. Misgeld, and J. R. Sanes. Assembly of the postsynaptic membrane at the neuromuscular junction: paradigm lost. *Curr Opin Neurobiol*, 16(1):74–82, 2006.

[156] Lee, Y., J. Rudell, S. Yechikhov, R. Taylor, S. L. Swope, and M. Ferns. Rapsyn carboxyl terminal domains mediate muscle specific kinase-induced phosphorylation of the muscle acetylcholine receptor. *Neuroscience*, 153(4):997–1007, 2008.

[157] Fuhrer, C., M. Gautam, J. E. Sugiyama, and Z. W. Hall. Roles of rapsyn and agrin in interaction of postsynaptic proteins with acetylcholine receptors. *J Neurosci*, 19(15):6405–16, 1999.

[158] Sobel, A., M. Weber, and J. P. Changeux. Large-scale purification of the acetylcholine-receptor protein in its membrane-bound and detergent-extracted forms from Torpedo marmorata electric organ. *Eur J Biochem*, 80(1):215–24, 1977.

[159] Phillips, W. D., e. a. Margaret M Maimone, M. M., and J. P. Merlie. Mutagenesis of the 43-kD postsynaptic protein defines domains involved in plasma membrane targeting and AChR clustering. *J Cell Biol*, 115(6):1713–23, 1991.

[160] Zhang, B., S.-W. Luo, X.-P. Dong, X. Zhang, C. Liu, Z. Luo, W.-C. Xiong, and L. Mei. Beta-catenin regulates acetylcholine receptor clustering in muscle cells through interaction with rapsyn. *J Neurosci*, 27(15):3968–73, 2007.

[161] Engel, A. G., K. Ohno, and S. M. Sine. Sleuthing molecular targets for neurological diseases at the neuromuscular junction. *Nat Rev Neurosci*, 4(5):339–52, 2003.

[162] Lommerse, P. H. M., B. E. Snaar-Jagalska, H. P. Spaink, and T. Schmidt. Single-molecule diffusion measurements of H-Ras at the plasma membrane of live cells reveal microdomain localization upon activation. *J Cell Sci*, 118(Pt 9):1799–809, 2005.

[163] Ferrari, R., A. Manfroi, and W. Young. Strongly and weakly self-similar diffusion. *Physica D*, 154(1-2):111–137, 2001.

[164] Gervásio, O. L., P. F. Armson, and W. D. Phillips. Developmental increase in the amount of rapsyn per acetylcholine receptor promotes postsynaptic receptor packing and stability. *Dev Biol*, 305(1):262–75, 2007.

[165] Gervásio, O. L. and W. D. Phillips. Increased ratio of rapsyn to ACh receptor stabilizes postsynaptic receptors at the mouse neuromuscular synapse. *J Physiol (Lond)*, 562(Pt 3):673–85, 2005.

[166] Kellner, R. R., C. J. Baier, K. I. Willig, S. W. Hell, and F. J. Barrantes. Nanoscale organization of nicotinic acetylcholine receptors revealed by stimulated emission depletion microscopy. *Neuroscience*, 144(1):135–43, 2007.

[167] Stetzkowski-Marden, F., K. Gaus, M. Recouvreur, A. Cartaud, and J. Cartaud. Agrin elicits membrane lipid condensation at sites of acetylcholine receptor clusters in C2C12 myotubes. *J Lipid Res*, 47(10):2121–33, 2006.

[168] Hezel, M., W. C. de Groat, and F. Galbiati. Caveolin-3 promotes nicotinic acetylcholine receptor clustering and regulates neuromuscular junction activity. *Mol Biol Cell*, 21(2):302–10, 2010.

[169] Suzuki, K. G. N., T. K. Fujiwara, F. Sanematsu, R. Iino, M. A. Edidin, and A. Kusumi. GPI-anchored receptor clusters transiently recruit Lyn and Galpha for temporary cluster immobilization and Lyn activation: single-molecule tracking study 1. *J Cell Biol*, 177(4):717–30, 2007.

[170] Suzuki, K. G. N., T. K. Fujiwara, M. A. Edidin, and A. Kusumi. Dynamic recruitment of phospholipase Cgamma at transiently immobilized GPI-anchored receptor clusters induces IP3-Ca2+ signaling: single-molecule tracking study 2. *J Cell Biol*, 177(4):731–42, 2007.

[171] Meier, J., C. Vannier, A. Sergé, A. Triller, and D. Choquet. Fast and reversible trapping of surface glycine receptors by gephyrin. *Nat Neurosci*, 4(3):253–60, 2001.

[172] Engelman, D. M. Membranes are more mosaic than fluid. *Nature*, 438(7068):578–80, 2005.

[173] Guignet, E. G., J.-M. Segura, R. Hovius, and H. Vogel. Repetitive reversible labeling of proteins at polyhistidine sequences for single-molecule imaging in live cells. *Chemphyschem : a European journal of chemical physics and physical chemistry*, 8(8):1221–7, 2007.

[174] Sine, S. M. and A. G. Engel. Recent advances in Cys-loop receptor structure and function. *Nature*, 440(7083):448–55, 2006.

[175] Peters, J. A., M. A. Cooper, J. E. Carland, M. R. Livesey, T. G. Hales, and J. J. Lambert. Novel structural determinants of single channel conductance and ion selectivity in 5-hydroxytryptamine type 3 and nicotinic acetylcholine receptors. *The Journal of Physiology*, 588(Pt 4):587–96, 2010.

[176] Niesler, B., J. Walstab, S. Combrink, D. Möller, J. Kapeller, J. Rietdorf, H. Bönisch, M. Göthert, G. Rappold, and M. Brüss. Characterization of the novel human serotonin receptor subunits 5-HT3C,5-HT3D, and 5-HT3E. *Mol Pharmacol*, 72(1):8–17, 2007.

[177] Morales, M. and S.-D. Wang. Differential composition of 5-hydroxytryptamine3 receptors synthesized in the rat CNS and peripheral nervous system. *J Neurosci*, 22(15):6732–41, 2002.

[178] Chameau, P. and J. A. van Hooft. Serotonin 5-HT(3) receptors in the central nervous system. *Cell Tissue Res*, 326(2):573–81, 2006.

[179] Färber, L., U. Haus, M. Späth, and S. Drechsler. Physiology and pathophysiology of the 5-HT3 receptor. *Scand J Rheumatol Suppl*, 119:2–8, 2004.

[180] Sun, H., X.-Q. Hu, M. B. Emerit, J. C. Schoenebeck, C. E. Kimmel, R. W. Peoples, A. Miko, and L. Zhang. Modulation of 5-HT3 receptor desensitization by the light chain of microtubule-associated protein 1B expressed in HEK 293 cells. *J Physiol (Lond)*, 586(3):751–62, 2008.

[181] Jansen, M., M. Bali, and M. H. Akabas. Modular design of Cys-loop ligand-gated ion channels: functional 5-HT3 and GABA rho1 receptors lacking the large cytoplasmic M3M4 loop. *The Journal of General Physiology*, 131(2):137–46, 2008.

[182] Cheng, A., K. A. Bollan, S. M. Greenwood, A. J. Irving, and C. N. Connolly. Differential subcellular localization of RIC-3 isoforms and their role in determining 5-HT3 receptor composition. *J Biol Chem*, 282(36):26158–66, 2007.

[183] Cheng, A., N. A. McDonald, and C. N. Connolly. Cell surface expression of 5-hydroxytryptamine type 3 receptors is promoted by RIC-3. *J Biol Chem*, 280(23):22502–7, 2005.

[184] Kim, J., H.-Y. Park, J. Kim, J. Ryu, D. Y. Kwon, R. Grailhe, and R. Song. Ni-nitrilotriacetic acid-modified quantum dots as a site-specific labeling agent of histidine-tagged proteins in live cells. *Chem Commun (Camb)*, 16:1910–2, 2008.

[185] Perez, J.-B., J.-M. Segura, D. Abankwa, J. Piguet, K. L. Martinez, and H. Vogel. Monitoring the diffusion of single heterotrimeric G proteins in supported cell-membrane sheets reveals their partitioning into microdomains. *J Mol Biol*, 363(5):918–30, 2006.

[186] Tairi, A. P., R. Hovius, H. Pick, H. Blasey, A. Bernard, A. Surprenant, K. Lundström, and H. Vogel. Ligand binding to the serotonin 5HT3 receptor studied with a novel fluorescent ligand. *Biochemistry*, 37(45):15850–64, 1998.

[187] Stora, T., R. Hovius, Z. Dienes, M. Pachoud, and H. Vogel. Metal ion trace detection by a chelator-modified gold electrode: A comparison of surface to bulk affinity. *Langmuir*, 13(20):5211–5214, 1997.

[188] Pick, H., A. K. Preuss, M. Mayer, T. Wohland, R. Hovius, and H. Vogel. Monitoring expression and clustering of the ionotropic 5HT3 receptor in plasma membranes of live biological cells. *Biochemistry*, 42(4):877–84, 2003.

[189] Rodova, M., K. F. Kelly, M. VanSaun, J. M. Daniel, and M. J. Werle. Regulation of the rapsyn promoter by kaiso and delta-catenin. *Mol Cell Biol*, 24(16):7188–96, 2004.

[190] Tsien, R. Y. The green fluorescent protein. *Annu Rev Biochem*, 67:509–44, 1998.

[191] Chalfie, M., Y. Tu, G. Euskirchen, W. Ward, and D. Prasher. Green Fluorescent Protein as a Marker for Gene Expression. *ScienceNew Series*, 263(5148):802–805, 1994.

[192] Zolotukhin, S., M. Potter, W. W. Hauswirth, J. Guy, and N. Muzyczka. A "humanized" green fluorescent protein cDNA adapted for high-level expression in mammalian cells. *J Virol*, 70(7):4646–54, 1996.

[193] Kredel, S., K. Nienhaus, F. Oswald, M. Wolff, S. Ivanchenko, F. Cymer, A. Jeromin, F. J. Michel, K.-D. Spindler, R. Heilker, G. U. Nienhaus, and J. Wiedenmann. Optimized and Far-Red-Emitting Variants of Fluorescent Protein eqFP611. *Chem Biol*, 15(3):224–33, 2008.

[194] Wiedenmann, J., B. Vallone, F. Renzi, K. Nienhaus, S. Ivanchenko, C. Röcker, and G. U. Nienhaus. Red fluorescent protein eqFP611 and its genetically engineered dimeric variants. *Journal of biomedical optics*, 10(1):14003, 2005.

[195] Shaner, N. C., R. E. Campbell, P. A. Steinbach, B. N. G. Giepmans, A. E. Palmer, and R. Y. Tsien. Improved monomeric red, orange and yellow fluorescent proteins derived from Discosoma sp. red fluorescent protein. *Nat Biotechnol*, 22(12):1567–1572, 2004.

[196] Campbell, R. E., O. Tour, A. E. Palmer, P. A. Steinbach, G. S. Baird, D. A. Zacharias, and R. Y. Tsien. A monomeric red fluorescent protein. *Proc Natl Acad Sci USA*, 99(12):7877–82, 2002.

[197] Nagai, T., K. Ibata, E. S. Park, M. Kubota, K. Mikoshiba, and A. Miyawaki. A variant of yellow fluorescent protein with fast and efficient maturation for cell-biological applications. *Nat Biotechnol*, 20(1):87–90, 2002.

[198] Day, R. N. and M. W. Davidson. The fluorescent protein palette: tools for cellular imaging. *Chem Soc Rev*, 38(10):2887–921, 2009.

[199] Miyawaki, A., O. Griesbeck, R. Heim, and R. Y. Tsien. Dynamic and quantitative Ca^{2+} measurements using improved cameleons. *Proc Natl Acad Sci USA*, 96(5):2135–40, 1999.

[200] Miyawaki, A., J. Llopis, R. Heim, J. M. McCaffery, J. A. Adams, M. Ikura, and R. Y. Tsien. Fluorescent indicators for Ca^{2+} based on green fluorescent proteins and calmodulin. *Nature*, 388(6645):882–7, 1997.

[201] Wallace, D. J., S. M. zum Alten Borgloh, S. Astori, Y. Yang, M. Bausen, S. Kügler, A. E. Palmer, R. Y. Tsien, R. Sprengel, J. N. D. Kerr, W. Denk, and M. T. Hasan. Single-spike detection in vitro and in vivo with a genetic Ca2+ sensor. *Nat Methods*, 5(9):797–804, 2008.

[202] Palmer, A. E., M. Giacomello, T. Kortemme, S. A. Hires, V. Lev-Ram, D. Baker, and R. Y. Tsien. Ca2+ indicators based on computationally redesigned calmodulin-peptide pairs. *Chem Biol*, 13(5):521–30, 2006.

[203] Dickson, R. M., A. B. Cubitt, R. Y. Tsien, and W. E. Moerner. On/off blinking and switching behaviour of single molecules of green fluorescent protein. *Nature*, 388(6640):355–8, 1997.

[204] Patterson, G. H. and J. Lippincott-Schwartz. A photoactivatable GFP for selective photolabeling of proteins and cells. *Science*, 297(5588):1873–7, 2002.

[205] Lippincott-Schwartz, J. and G. H. Patterson. Development and use of fluorescent protein markers in living cells. *Science*, 300(5616):87–91, 2003.

[206] Betzig, E., G. H. Patterson, R. Sougrat, O. W. Lindwasser, S. Olenych, J. S. Bonifacino, M. W. Davidson, J. Lippincott-Schwartz, and H. F. Hess. Imaging intracellular fluorescent proteins at nanometer resolution. *Science*, 313(5793):1642–5, 2006.

[207] Mckinney, S. A., C. S. Murphy, K. L. Hazelwood, M. W. Davidson, and L. L. Looger. A bright and photostable photoconvertible fluorescent protein. *Nat Methods*, 6(2):131–3, 2009.

[208] Subach, F. V., G. H. Patterson, S. Manley, J. M. Gillette, J. Lippincott-Schwartz, and V. V. Verkhusha. Photoactivatable mCherry for high-resolution two-color fluorescence microscopy. *Nat Methods*, 6(2):153–9, 2009.

[209] Müller, J. S., G. Mildner, W. Müller-Felber, U. Schara, K. Krampfl, B. Petersen, S. Petrova, R. Stucka, W. Mortier, J. Bufler, G. Kurlemann, A. Huebner, L. Merlini, H. Lochmüller, and A. Abicht. Rapsyn N88K is a frequent cause of congenital myasthenic syndromes in European patients. *Neurology*, 60(11):1805–10, 2003.

[210] McLaughlin, S. and A. Aderem. The myristoyl-electrostatic switch: a modulator of reversible protein-membrane interactions. *Trends Biochem Sci*, 20(7):272–6, 1995.

[211] Nirenberg, M., S. Wilson, H. Higashida, A. Rotter, K. Krueger, N. Busis, R. Ray, J. G. Kenimer, and M. Adler. Modulation of synapse formation by cyclic adenosine monophosphate. *Science*, 222(4625):794–9, 1983.

Acknowledgments

It would not have been possible to achieve this work without the help and support of many persons. I would like to thank some of them.

I would like to thank the professor Horst Vogel for giving me the opportunity to join his research group, especially for the freedom of research and the great work conditions provided.

I also would like to thank the doctor MER Ruud Hovius for the incredible amount of time spent in direction and discussions on all the aspect of the work presented here. I also want to emphasize his humanity and tolerance with young scientists and their ideas.

Special thank to Verena Tabet for her kindness and, among other human qualities, her ability to make administrative things easier and to Cédric Deluz, because this laboratory would not be the same without him.

I also would like to thank the persons who have taught me the different techniques used during this work, Emmanuel Guignet, who showed me the basics of molecular biology and lab practice, Jean-Manuel Segura and Christoph Schreiter, who explained me almost everything about single-molecule microscopy and data analysis.

It would be very difficult to work in a lab alone. Therefore, I would like to thank all the member of the LCPPM for their daily support, help and friendship, more particularly Olivia Baud, Sophie Roizard, Thamani Dahoun, Veronica Ponce de Leon, Christophe Danelon, Davor Kosanic, Enrico Condemi, Ghérici Hassaïne, Luigino Grasso, Menno Tol, Michael Werner, Pedro Pascoal, Romain Wyss, Sylvain Etter, Ralf Schmauder, Samuel Terrettaz and all the others.

Some part of this thesis would not have been performed without the help of my students. I would like to thank Linda Wicht, Nathalie Preiswerk, Cyril Moccand, Erol Basic, and Yvan Bouza.

I would like to thank all my friends for their support during all my studies and this thesis.

Finally the most important thanks go to my parents, my brother and my sister who have always believed in me and supported me during all these years.

Curriculum vitae

Joachim Piguet

Born on August 30, 1979 in Pompaples, Switzerland

2005-2010	PhD thesis under supervision of Prof. Horst Vogel and Ruud Hovius at the Institute of Chemistry and Chemical Engineering of EPFL, Lausanne, Switzerland.
1999-2005	Studies in chemical and biological engineering. École Polytechnique Fédérale de Lausanne, Switzerland, Master in chemical and biological engineering.
1995-1999	Gymnase cantonal du Bugnon, Lausanne, Switzerland, maturité fédérale de type C.